UNIVERSITY OF CALIFORNIA

Los Angeles

Optical Probing of CO_2 Laser-Plasma Interactions at Near Critical Density

A dissertation submitted in partial satisfaction

of the requirements for the degree

Doctor of Philosophy in Electrical Engineering

by

Chao Gong

2015

ABSTRACT OF THE DISSERTATION

Optical Probing of CO_2 Laser-Plasma Interactions at Near Critical Density

by

Chao Gong

Doctor of Philosophy in Electrical Engineering

University of California, Los Angeles, 2015

Professor Chandra Joshi, Co-Chair

Professor Warren Mori, Co-Chair

The interaction of a high-power laser beam with plasma has been explored extensively in the context of laser-driven fusion, plasma-based acceleration of ions and electrons and high energy-density physics. One of the fundamental processes common to all these studies is the penetration of intense light into a dense matter through the hole boring effect and self-induced transparency. Light with a given wavelength λ will be reflected once the electron density equals the critical electron plasma density $n_c = 1.1\times10^{21} cm^{-3} / [\lambda(\mu \text{m})]^2$. The radiation pressure exerted on the critical density layer is characterized by the ponderomotive force of a focused laser pulse which scales with a laser intensity, I as $I\lambda^2$ Wμm^2/cm^2. At $I\lambda^2$ ~10^{17} Wμm^2/cm^2 and above, it becomes possible for the laser pulse not only to steepen the plasma profile but to push the overcritical plasma with $n_e > n_c$ creating a cavity or a hole in the target. The phenomenon of hole boring, whereby a laser pulse propagates through a reduced density cavity to reach and push the critical density layer, is of importance in fast-ignition fusion because it may allow the laser pulse

to deliver its energy closer to the compressed fuel where it can be converted into fast electrons that are needed to ignite a small portion of the fuel. The layer of plasma pushed by the radiation pressure can reflect and accelerate ions via the so called Hole Boring Radiation Pressure Acceleration mechanism. Also the density pile- up in combination with the strong electron heating at the critical density layer can facilitate the formation of a collisionless shock. This shock wave acceleration can produce high energy ion beams with a narrow energy spread.

Numerous experiments have been carried out to study dynamics of laser plasma interaction indirectly using solid state targets that are opaque for 1µm laser. However, by using a longer wavelength CO_2 laser, λ = 10.6µm, the critical plasma density is decreased by a factor of 100 ($n_c \approx 1\times10^{19} cm^{-3}$). Therefore overdense CO_2 laser plasma is transparent for a fast optical probe which opens a unique opportunity to study the physics of laser hole boring in the temporal and spatial domain simultaneously. This thesis reports the first direct measurements of the laser hole boring velocity in an overdense plasma using a four-frame picosecond green pulse interferometry.

The plasma was created by tunnel ionization of a plume of He gas from a gas jet using a train of 3ps long CO_2 laser pulses. For probing the plasma, a ~2ps frequency-doubled (532nm) Nd:Glass laser pulse is used in a four-frame interferometry scheme. Spatio-temporal dynamics of hole boring in CO_2 laser-plasma interaction at $I\lambda^2 \leq 2\times10^{18}$ Wµm^2/cm^2 are studied with a ~15µm spatial and better than 2ps time resolutions. Experimental measurements indicate the hole boring process is determined by a balance between the radiation pressure P_L and thermal pressure P_{th}. As a result of this competition, v_{hb} increases during the risetime of the laser pulse where $P_L > P_{th}$ but decreases with a larger slope rate on the falling edge. This is because the plasma electrons once heated cool slowly and P_{th} diminishes the efficacy of P_L even faster.

The dissertation of Chao Gong is approved.

Pietro Musumeci

Chandra Joshi, Committee Co-Chair

Warren Mori, Committee Co-Chair

University of California, Los Angeles

2015

Dedication

To my parents, without whose enduring love, support and sacrifice, this wouldn’t be possible.

TABLE OF CONTENTS

LIST OF FIGURES

LIST OF TABLES

ACKNOWLEDGEMENTS

I would like to acknowledge the great help from Dr. Sergei Tochitsky who guided me through each step of this work. On daily basis, he worked with me through my entire Ph.D. project and helped me develop the experimental skills which I possess now. Without his expertise and optimistic approach, this experiment would never come to any fruition. I would also like to thank Jeremy Pigeon for spending countless hours in running the data acquisition systems during the experiment. Many thanks to Ken Marsh's research group for a consistent interest and support to this project. Thanks to Frederico Fiuza for his 2D simulational support and the contribution to the theoretical part of this dissertation. Thanks a lot to Maria Guerrero who spent a great deal of time helping me to resolve the student related issues. Last, but certainly not the least, I would like to thank my supervisor, Professor Chan Joshi, for all of his support, guidance and for allowing me to pursue a research area that interests me.

VITA

2004 B.S. in Material Science Engineering, Zhejiang University, Zhejiang, Hangzhou, China

2006 M.S. in Optical Engineering, Zhejiang University, Zhejiang, Hangzhou, China

2008 M.S. in Electrical Engineering, Lehigh University, Bethlehem, PA

2008-2015 Graduate Student Researcher at UCLA, Department of Electrical Engineering.

PUBLICATIONS

Direct observation of spatio-temporal dynamics of laser-hole boring in a near critical plasma

Chao Gong, Sergei Tochitsky, Frederico Fiuza, Jeremy J. Pigeon, and Chan Joshi. *Submitted to* ***Phys. Rev. Lett.*** **(2015)**

Collisionless shocks in laser-produced plasma generate monoenergetic high-energy proton beams

Dan Haberberger, Sergei Tochitsky, Frederico Fiuza, Chao Gong, Ricardo A. Fonseca, Luis O. Silva, Warren B. Mori and Chan Joshi. ***Nature Physics 8, 95-99 (2012)***

Laser-Driven Shock Acceleration of Monoenergetic Ion Beams

F. Fiuza, A. Stockem, E. Boella, R.A. Fonseca, L.O. Silva, D. Haberberger, S. Tochitsky, C. Gong, Warren B. Mori and Chan Joshi. ***Phys. Rev. Lett. 109, 215001 (2012)***

CHAPTER 1

1. Introduction

The field of laser plasma interaction has seen resurgence during the past two decades because of the availability of lasers that generated intense enough pulses to make plasma electrons oscillate with relativistic velocities. One reason for this is the steady progress during these two decades of the chirped pulse amplification (CPA) technology that allowed for the first time to compress the laser pulse in the temporal dimension [1]. This technology led to great advances in the achievable laser powers and focused intensities and opened the opportunity for studying the interaction process between the relativistic laser pulse ($a_o \geq 1$, a_o is the normalized potential vector of the laser) and plasmas in different density regimes. A wide range of basic plasma physics and practical applications have been explored including generation and saturation of plasma instabilities [2], transport of intense heat flux, compact laser-driven particle accelerators [3], and fast ignition of laser fusion [4]. While the CPA scheme was mostly adopted to produce femtosecond-class pulses using near-infrared lasers (Ti-sapphire and Nd:Glass for instance), a different technique (described later in this thesis) was developed for amplification of picosecond mid-IR (the 10μm CO_2 laser) laser pulses to relativistic intensities. This opened a new opportunity for studying near-critical density intense-laser-plasma interactions because the critical plasma density for 10μm pulses (density at which the electron plasma frequency equals the laser frequency) is 10^{19} cm^{-3} – i.e. sufficiently small for probing the interaction physics using optical frequency (0.53μm) laser pulses. This is the main goal of this thesis. We have developed a picosecond multi-frame interferometry technique and used it to directly visualize and characterize an important but previously indirectly inferred phenomenon known as “hole-boring” of intense laser pulses into the above critical density plasma.

When considering the interaction between an electromagnetic wave and a fully ionized plasma, the density regimes of the plasma can be categorized by the local plasma density with respect to the critical density of the incident laser pulse $n_c = \frac{m_e \varepsilon_o \omega^2}{e^2}$, where n_c is the critical density, m_e is the electron mass and ω is the angular frequency of laser radiation. When plasma density $n_e < 0.5\, n_c$, it is typically regarded as an underdense plasma which can be nearly transparent for the laser pulse propagating through it. For densities larger than n_c, the plasma is opaque for the laser pulse and it is called overdense. In the range of plasma densities from $0.5n_c$ to n_c, laser-plasma interaction occurs at near critical density and both the underdense and overdense portions of the plasma influence the interaction.

To date, it is the underdense laser-plasma interactions that are studied the most both experimentally and numerically [5]. This is so because laser-plasma parametric instabilities such as Stimulated Raman (SRS) and Brillouin (SBS) scattering, two-plasmon decay, self-focusing and filamentation all occur in the underdense region. These nonlinear optical effects were detrimental to the coupling efficiency of laser light in both direct and indirect fusion and therefore were studied in great details in plasmas with flows and density gradients. In addition all these effects have additional characteristic signatures at relativistic intensities. For instance, one of the observed phenomena is channel formation and self-focusing due to either the thermal or the ponderomotive force causing charge displacement of the plasma electrons. At high laser intensities, relativistic change in the electron mass becomes important and leads to the lowering of the plasma frequency [6]. It is found that a relativistic filament with finite electron density is unstable to transverse modulations, which leads to break up of the laser pulses into independent filaments. The surface wave formed on the walls of the plasma channels also has the capability to accelerate electrons [7]. The SRS, the two-plasmon decay instabilities produce plasma waves that can trap and accelerate plasma electrons whereas the SBS instability produces an ion wave that can trap and heat ions. Of particular interest has been the Stimulated Raman forward Scattering instability that produces relativistic plasma waves that in turn can accelerate electrons to relativistic energies. The observation of such relativistic electrons gave an impetus to the field of laser-plasma electron accelerators. All the laser-plasma acceleration schemes including the self-modulated laser wakefield accelerator [8], the plasma beat wave accelerator [9] and the laser wakefield accelerator [10] are fundamentally Raman accelerators in a sense that in all cases a plasmon induced in an underdense plasma by a laser pulse traps and accelerates electrons to high energies. A comprehensive study of laser-plasma accelerators has been reported in a Reviews of Modern Physics article by E. Esaray et al [11]. In addition to electron acceleration, relativistic self-focusing effect in the underdense plasma can also lead to a few times laser intensity enhancement compared to the focused intensity in vacuum. This leads to the acceleration of ions in the transverse direction. Krushelnick et al. [12] have observed helium ions with peak energy of 3.6MeV, which is inferred as a result of this effect.

Studies of the interaction between high intensity laser pulses and near critical density and overdense plasmas frequently produced using a solid target have mainly focused on understanding different plasma heating mechanisms such as collisional absorption (also known as inverse Bremstrahlung), resonance absorption, vacuum heating, and the so-called J×B heating [13]. Based on accumulated experimental as well as simulations knowledge, the heated electrons near the critical density surface are known to exhibit a two-temperature distribution. The fraction of energy absorbed by the plasma and the resulting so-called hot-electron temperature strongly depend on the density scale-length at the critical surface, the angle of incidence of the laser light, the cold-electron temperature and the laser intensity.

An important phenomenon during the overdense laser-plasma interaction is the high order harmonics generation (HHG) of laser radiation. It should be mentioned that HHG is seen in underdense plasmas as well and is well explained by the so-called recollision model [14]. The mechanism that produces high order harmonics at critical density is however different than recollision of a nearly ionized electron with the atomic nucleus. When the laser pulse is focused on to the critical surface of a solid target, a significant fraction of the electromagnetic radiation scattered is composed of harmonics of the laser frequency, which can even extend into the soft x-ray region of the spectrum. Indeed the production of harmonics up to the 75^{th} order (of 1.053 μm radiation) has been observed by focused laser intensities up to 10^{19} Wcm^{-2} with a conversion efficiency of 10^{-6} [15]. This can be understood as resulting from an oscillating current of electrons dragged across the vacuum-solid surface by the intense electric field of the laser pulse. The efficient generation of such harmonics has a potential to be used as a bright source of XUV radiation [16].

A near critical density plasma with a peak density between 0.5 and a few times n_c is an interesting object of study. Typically, such plasmas can be generated by using foam targets in the case of a near infrared/visible lasers or a gas jet target using a CO_2 laser. The latter represents a unique opportunity for studying near critical density laser-plasma interaction phenomena because the plasma density can be easily changed from 0.1-5n_c ($n_c = 1\times 10^{19} cm^{-3}$) by changing the backing pressure of the gas while the composition of the plasma can be changed by using different molecular and noble gases (H_2, He, N_2, Ar etc.).

There is a considerable interest in understanding how an intense laser pulse penetrates and heats a near critical density plasma. The radiation pressure of an intense laser pulse can steepen the density profile of such a plasma and pile up and even push the plasma electrons and ions that are in the vicinity of the critical density layer. In 3D, this process can bore a density cavity or a hole that is continuously pushed further into the higher density plasma by the increasing intensity of the laser pulse. The electric field associated with this moving layer of piled up plasma can reflect and accelerate plasma ions- a process known as hole boring Radiation Pressure Acceleration (HB-RPA) mechanism [17]. Also this hole boring process creates a density discontinuity which along with strong electron heating at the n_c layer may result in launching a collisionless laminar electrostatic shock in plasma [18] that as shown recently can accelerate ions to high kinetic energy.

In this thesis, an experimental study of laser hole boring is carried out using a CO_2 laser pulse train with peak intensities between 1×10^{15} W/cm^2 to 2×10^{16} W/cm^2. While a limited number of 2D particle-in-cell code simulations were carried out to compare the experimental measurements with a computer experiment, these simulations are very expensive to carry out. Therefore, to study the basic physics of this process- how does the radiation pressure of the laser pulse push a thermal plasma-, a 1-D plasma simulation code is used to simulate laser pulse steepening and pushing a plasma with an initial linear density ramp for different laser-plasma parameters. There 1D simulations are described in Chapter2.

Since Wilks et al. [19] first proposed that the laser hole boring process may be a way to deposit the laser pulse energy closer to the compressed laser fusion target to generate fast electrons which will ignite a portion of the fuel (in a scheme known as fast-ignition), there has been a tremendous interest in studying this process. Previous studies have indirectly inferred the motion of the plasma layer that is being pushed by the intense laser pulse by either measuring the Doppler shift of the laser pulse reflected from the critical density layer or of high order harmonics self-generated as described above [20, 21].

Any observed frequency shift in the fundamental wavelength or its harmonics (second/fourth) is assumed to be caused by the reflection from a moving critical density layer pushed by the pump laser. The main problem of Doppler technique is the lack of spatial resolution. Also the time integrated or time resolved backscattered light spectra can be affected by other nonlinear effects such as self-phase modulation—particularly important in an ionizing plasma.

Another technique dedicated to study the laser hole boring process is a short pulse X-ray laser interferometry allowing one to look inside the overdense plasma. This has produced convincing interferograms of the laser-produced cavity. However, no systematic measurements of the temporal evolution or the dependence of the hole boring velocity on the intensity of the laser were carried out in this study.

To our knowledge, there have been no direct measurements of the continuously moving density cavity produced close to the critical density layer reported to date since it is extremely challenging to develop an ultra-fast probe for the solid-density plasma due to its opacity for light.

In contrast to the solid targets, using a CO_2 laser and gas plasma interaction to study hole boring gives an opportunity to directly visualize both the laser cavity and its motion in the direction of the laser pulse using visible-probe interferometry. In the following chapters, we will discuss the picosecond multi-frame interferometry technique for laser hole boring velocity measurements and the physics that has been unravelled.

So far, we have reviewed previous studies of intense laser plasma interactions at different density regimes, such as SRS and SBS scattering, two-plasmon decay, self-focusing and filamentation effects in underdense case as well as plasma heating mechanisms, HHG process in overdense case. In the following chapters we focus on studying the laser hole boring process. Chapter 2 describes some key physics concepts that affect the hole-boring process under different laser and plasma parameters. Chapter 3 describes the Neptune CO_2 laser system that generates a train of picosecond pulses with intensities necessary to push the critical density surface of a plasma. Chapter 4 discusses the experimental set-up and in particular the four--frame interferometry method developed here to visualize the cavity formation in the plasma density by the radiation pressure of the laser pulses and the dynamics of the pushing of this cavity forward in the direction of the laser (hole boring). Chapter 5 shows the raw experimental data and its analysis that clearly shows evidence for hole-boring and its dependence on the laser intensity near critical density He plasmas. Chapter 6 presents the details of ion acceleration results by hole boring effect. This is followed by the conclusions chapter.

CHAPTER 2

2. Hole Boring and Laser Plasma Heating

2.1 Simple Model for Laser Hole Boring due to Wilks

An intense laser pulse incident on a critical density plasma will push the plasma forming a cavity or a hole in a process known as laser hole boring [19, 22].

To describe this process, we can start from an ideal scenario assuming that a laser pulse is normally incident upon the critical density plasma layer and that all the laser energy is reflected by the plasma. Laser radiation pressure can be defined as $P_L = 2I/\mathrm{c}$, where I is the laser intensity and c is the speed of light. Based on the conservation of momentum, the change in momentum of the laser photon is mostly imparted to the plasma ions pushing them forward at the hole boring speed v_{hb}. In the laboratory frame the ions are reflected off the moving plasma thus accelerated to twice velocity of v_{hb}. Therefore, balancing momentum flux gives:

$$(2v_{hb}n_i M)v_{hb} = \frac{2I}{c} \tag{1}$$

where n_i is the ion density, v_{hb} is the hole boring velocity and M is the ion mass. The critical plasma density is defined for condition $\omega_p = \omega_L$ as $n_c = \frac{\omega_L^2 \varepsilon_o m}{e^2}$ (ω_L is the angular frequency of the laser pulse, m is the electron mass), laser intensity can be written as $I = \frac{c\varepsilon_o}{2} E_L^2$ (E_L is electrical field of the laser pulse) and the ion density $n_i = \frac{n_{pe}}{Z}$ (Z is the ionized charge state). Replace I and n_i in Eq. (1) and we obtain:

$$\frac{v_{hb}}{c} = \left(\frac{n_c}{2n_{pe}}\frac{Zm}{M}\right)^{1/2}\frac{eE_L}{mc^2 k_L} \tag{2}$$

Where k_L is the wavenumber of the incident laser pulse. Now if we introduce the normalized amplitude of the laser vector potential $a_o = \frac{eE_L}{mc^2 k_L}$ and its handy engineering formula

$a_o \approx 8.5\times10^{-10} I^{0.5}[\mathrm{W/cm^2}]\lambda[\mu\mathrm{m}]$, where I is the intensity and λ is the wavelength, Eq. (2) will become:

$$\frac{v_{hb}}{c} = [\frac{n_{cr}}{2n_{pe}} \frac{Zm}{M} \frac{I\lambda^2}{1.37\times10^{18}}]^{1/2} \tag{3}$$

The above expression of laser hole boring velocity was first introduced in the paper of S.C. Wilks et.al in 1992 based on an earlier paper by Kruer et.al in 1975 [22]. In the 1992 paper, the possibility of coupling laser light to an overcritical plasma by pushing the plasma in the vicinity of the critical density layer forward was investigated. It assumes that all the laser energy is reflected and there is a balance of momentum flux between the momentum imparted by the reflected laser and the moving plasma.

2.2 Laser-Plasma Coupling Mechanisms and their Effect on v_h

This proposed simple model for v_h agrees with the 1D simulation results very well for the case when ponderomotive heating dominates (at laser intensity greater than 10^{18} W/cm^2) and for a normal incidence angle upon the plasma [19]. However, for an intensity less than 10^{18} W/cm^2, a variety of laser absorption models and plasma heating mechanisms need to be considered and Eq.(3) is only used as an upper boundary for v_{hb} estimation. It should be noted that Wilk's model does not take into account the thermal pressure of the plasma which counterbalances the radiation pressure.

The heating mechanisms in the interaction of a laser pulse ($0.1 \le a_o \le 1$) and plasma include collisional absorption, resonant absorption, vacuum heating, ponderomotive heating (all these occur near the critical density) and stimulated Raman scattering and two-plasmon decay heating (these occur in the underdense region of the plasma) [23]. These mechanisms contribute to the laser energy absorption differently as a function of laser intensity and experimental geometry. Generally speaking, the absorption rate depends on the plasma density scale length L, the laser incident angle θ, the laser intensity times the wavelength squared- $I\lambda^2$ and the plasma collision frequency. When $I\lambda^2 \leq 10^{15}$ $Wcm^{-2}\mu m^2$, the collisional effects between the electrons and ions are typically significant and collisional absorption or so called "inverse bremsstrahlung" contributes to the total plasma heating significantly. However, when the laser intensity increases, the effective temperature of plasma also increases. Since the electron collisional frequency is inversely proportional to the effective plasma temperature $1/T_{eff}^{2/3}$, the collisional absorption will decrease. As expected, the collisional absorption increases with the plasma density scale length and decreases relative to resonance absorption with the increase of the laser incident angle [13]. As $I\lambda^2$ approaches 10^{17} $Wcm^{-2}\mu m^2$, collisional absorption effect becomes relatively unimportant because of the effect of the large oscillating velocity of the electron on reducing the collision frequency.

Resonant absorption can be significant either at low or high laser intensities. When the laser is p-polarized and incident upon the target obliquely, an important parameter $v_{osc} / \omega_L L$ helps to determine if the resonant absorption effect would occur. Here L is the plasma density scale length, ω_L denotes the laser frequency, and $v_{osc} = eE/m_e\omega$ is the quiver velocity of the electrons, in which, E and ω represent the laser electric field and the laser frequency, m_e is the electron mass. When L is large, a fraction of the evanescent laser electric field that points in the direction of the density gradient will result in oscillation of electrons along this direction causing the excitation of an electron electrostatic wave (ESW). As this wave grows it narrows and eventually breaks, transferring its oscillatory energy into the kinetic energy of the fast electrons that are directed down the density gradient. This plasma heating mechanism is called resonant absorption which can be very efficient when the laser incident angle matches with the plasma density gradient. The optimal laser incident angle for resonant absorption happens at $\theta_m = \arcsin(0.68(\omega_L \mathrm{L}/\mathrm{c})^{-1/3})$ [24].

Vacuum heating absorption can happen at the laser irradiance $I\lambda^2 \geq 10^{17}$ $\mathrm{Wcm^{-2}\mu m^2}$ when the laser is incident obliquely upon sharply bounded overdense plasma. The plasma density profile needs to be very steep ($L \ll \lambda$). At this condition, strong laser energy absorption can be accounted by the electrons that are pulled into vacuum and sent back to the plasma in the laser electric field with a quiver velocity v_{osc} ~c. This plasma heating mechanism is more efficient than the usual resonant absorption for $v_{osc}/\omega > L$.

When the laser intensity keeps increasing ($a_o \geq 1$), the ponderomotive force is strong enough to push electrons forward in the incident direction, this process can significantly transfer the laser energy into the electrons, which is also called j×B heating or ponderomotive force heating [25].

Lastly, Raman Back (RBS), Side (RSS) and Forward Scattering (RFS) instabilities can also cause significant plasma heating. These involve the scattering of the incident EM wave into an either back, side or forward scattered EM waves and a plasma wave. Basically the incident EM wave collectively Thomson scatters from plasma thermal fluctuations at the plasma frequency. The scattered light is frequency downshifted by ω_p. Now the beating of the incident and the scattered light reinforces the plasma density fluctuation via the ponderomotive force which then scatters even more photons and thus leads to the Raman instability. The plasma waves associated with backscatter and sidescatter have non-relativistic phase velocities whereas that associated with forward scattering is typically relativistic. The trapping of electrons or breaking of these waves can strongly heat the plasma. The RFS instability in particular can generate relativistic electron temperatures because the phase velocity of the plasmons is close to c. The RFS instability has a higher threshold than RBS and is strongly susceptible to the plasma density gradients compared to RBS. However laser self-focusing due to thermal or ponderomotive effects can increase the peak laser intensity and lead to the onset of RFS. In additional, when the laser pulse with power $P \geq P_{cr}$ is interacting with the underdense plasma at $n_e \leq 0.25 n_c$ [26], it will be focused due to relativistic effects and the resultant plasma dynamics can be strongly nonlinear. Here $P_{cr} \cong 17(\omega_o/\omega_p)^2$ [GW] is the critical power for the relativistic self-focusing, where ω_o is the laser angular frequency and ω_p is the plasma frequency. During this process, the peak laser field can be significantly enhanced due to the radially dependent relativistic mass increase of the electrons that produces a convex refractive index gradient in the plasma that causes the laser wavefront to converge. In addition to self-focusing in this relativistic intensity regime a two dimensional modulational instability can occur that is similar to RFS in that the plasma wave involves has the same phase velocity as that in RFS and can therefore accelerate electrons to high energies. This instability leads to the self-modulated laser wakefield acceleration.

2.3 1-D OSIRIS SIMULATION RESULTS

2.3.1 Hole Boring Velocity Measurement in Function of a_o

To accurately account for the plasma heating and self-focusing/filamentation of the laser pulse one needs to do multi-dimensional numerical modeling, which can be extremely time consuming and expensive. Indeed this is what was done to model the experimental data that is described later on in the thesis (in collaboration with Dr. Frederico Fiuza of Lawrence Livermore Laboratory). However much of the salient features of a heated plasma being pushed forward by the radiation pressure of the laser pulse can be qualitatively studied in 1D geometry.

In particular to demonstrate how the heated plasma temperature affects the hole boring velocity, we carried out simulations with the one dimensional version of OSIRIS PIC code [27] to measure the scaling of the hole boring velocity in terms of the laser normalized vector potential a_o ($\propto I\lambda^2$) and then further analyzed the results to see how the hole boring velocity varied with the plasma temperature.

As shown schematically in Figure 1, these simulations involve a single 70ps CO_2 laser pulse with a various values of a_o = 0.5, 1.0, 1.5 (which for a CO_2 laser corresponds to intensities of 8×10^{15}, 1×10^{16} and 3×10^{16} W/cm^2 respectively). The pulse is incident on a preformed, cold and collisionless 1.5n_c flat top density plasma. The semi-infinite plasma profile has a sharp rising front starting at 17.64mm and a flat top with a constant density at 1.5n_c.

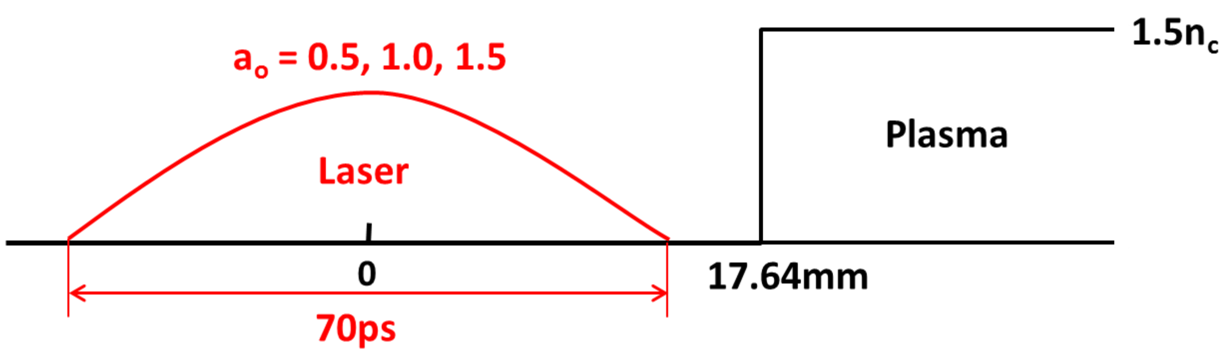

Figure 1: Schematic of the laser and plasma initial conditions used in 1-D OSIRIS PIC code simulations of hole boring velocity measurement.

The table below summarizes the parameters used in the simulations. Note that, since the plasma is above the critical density, the laser frequency ω_o is equal to the plasma frequency ω_p.

Parameter	**Value**
Longitudinal Box Size	$16{,}000\,\frac{c}{\omega_o} = 27.2\text{mm}$
Spatial Resolution	$0.2\,\frac{c}{\omega_o} = 3.4\times10^{-4}$ mm
Time Resolution	$0.2\,\frac{1}{\omega_o} = 1.1\times10^{-3}$ ps
Time Duration	$30{,}000\frac{1}{\omega_o} = 167.1$ ps
Charge to mass ratio	7344 (He^{1+})
Laser pulse duration	$12568\,\frac{1}{\omega_o} = 70\text{ps}$
a_o	0.5, 1.0 and 1.5

Table 1: Parameter setup in hole boring velocity measurement as a function of a_o using 1-D OSIRIS PIC code simulation for He^{1+}.

The method we use to measure the hole boring velocity is based on the Doppler effect in which the CO_2 laser light reflected from the moving critical density plasma layer will experience a red-shift. The redshifted frequency (Doppler frequency) can be calculated as in Eq. (4) below:

$$\nu_D = (1 - \frac{v_{hb}}{c})\nu_o \tag{4}$$

Where ν_D is the redshifted frequency, v_{hb} is the hole boring velocity and ν_o is the incident laser frequency.

The reflected redshifted pulse will then beat with the incident pulse and the hole boring velocity can be extracted from the beat frequency. The relationship between the hole boring velocity and the beat frequency, ν_b, is shown in Eq.(5):

$$\frac{\nu_b}{\nu_o} = \frac{\text{v}_{hb}}{c} \tag{5}$$

Figure 2 below depicts the simulation results that demonstrate an example of how the beating can be used in the hole boring velocity measurement.

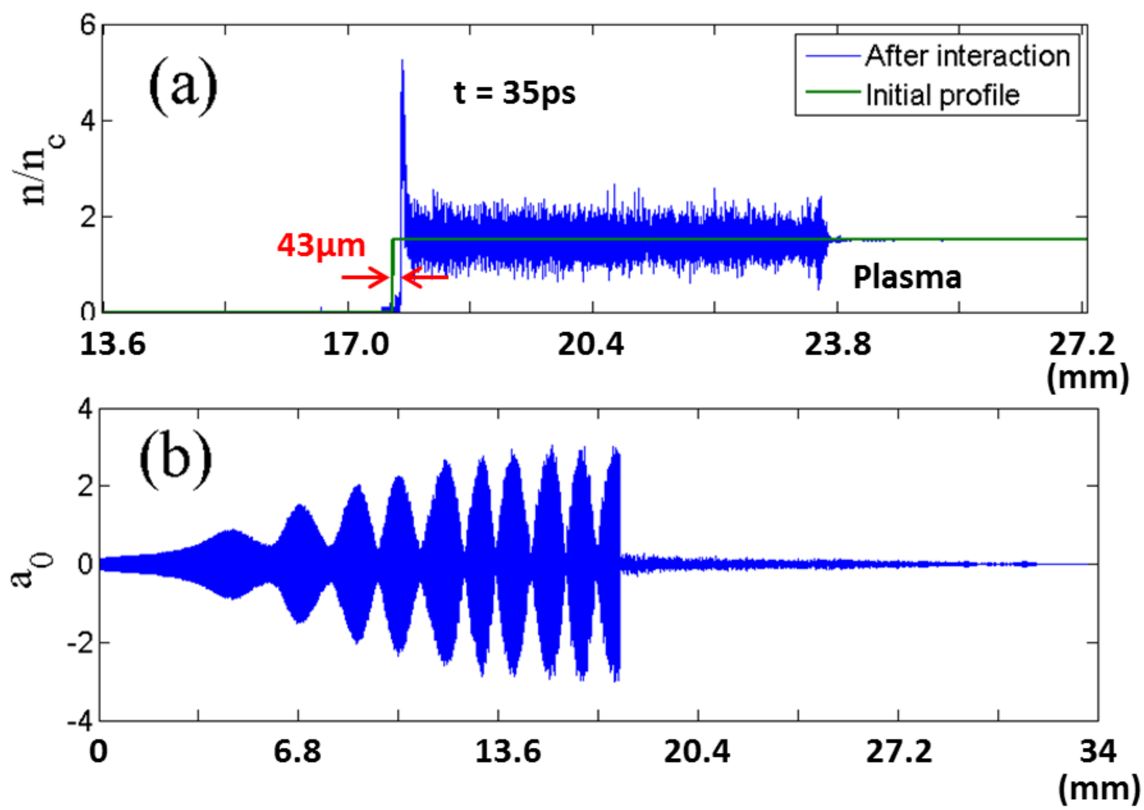

Figure 2: (a) The plasma density profile at time t = 35ps when the peak laser intensity is incident upon the plasma. Solid green line depicts the initial plasma density profile. Solid blue line is the plasma density profile after the laser pulse has been reflected. (b) The CO_2 laser beat pattern as a function of space. Here, the initial a_o of the incident laser pulse is 1.5.

The case shown in Figure 2 is performed at laser $a_o = 1.5$. As can be seen in Figure 2(a), the plasma density profile is clearly steepened by the CO_2 laser pulse at t = 35ps. Also the peak density increases from $1.5n_c$ up to $5n_c$ due to the plasma pile up caused by the ponderomotive force exerted by the laser pulse. Here we will use the term ponderomotive force (proportional to the gradient of the laser intensity when talking about 1D simulations and radiation pressure when discussing the 2D simulations later in the thesis). This steepened density profile is pushed forward by a measurable amount (43μm) at this time. In Figure 2(b), we observe that the laser profile has a characteristic beat pattern with a beat frequency that increases as a function of time. This shows the point from which the laser light is being reflected is accelerated from rest to some asymptotic velocity as the plasma critical density layer is pushed by the laser radiation.

In Figure 3(a), we indicate the typical snapshot of the distance between the adjacent peaks of the beat pattern taken at the peak of the laser pulse. Here the beat frequency can be measured and by using Eq. (5) we can therefore derive the hole boring velocity. Figure 3(b) is a plot of the extracted hole boring velocity for different measurement points, as depicted in Figure 3(a). Here the theoretical value of the hole boring velocity is calculated from on Eq. (3) and shown by a black dashed line.

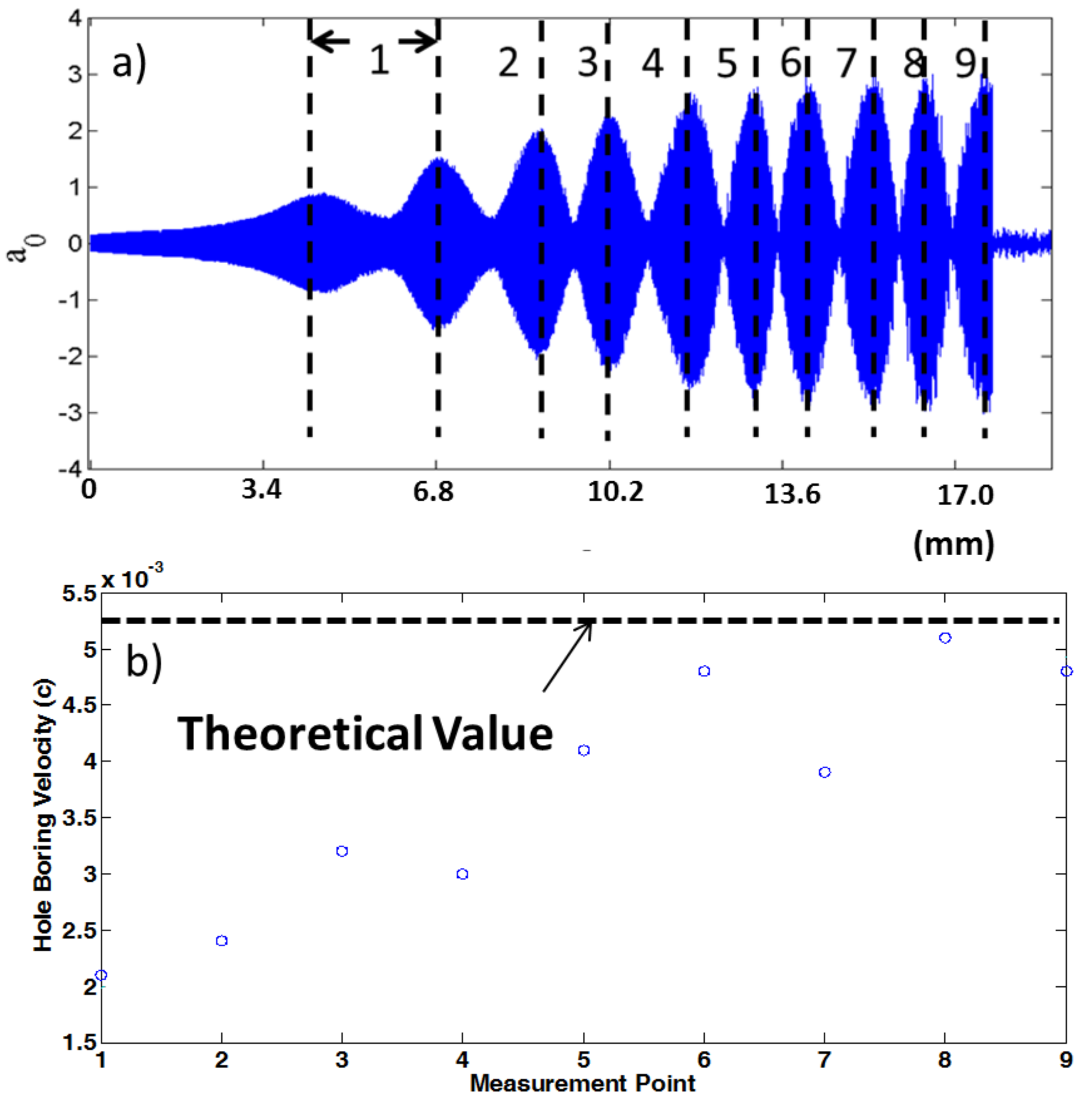

Figure 3: (a) The beat between the incident and reflected portion of the laser pulse as a function of space. Dashed lines indicate where measurements of the beat wavelength are taken. (b) The hole boring velocities for different measurement points. The dashed line shows the maximum theoretical hole boring velocity calculated using Eq. (3) in this simulation condition.

Using the same method, we have calculated the hole boring velocities for other laser pulses all 70ps (base-to-base) long but peak a_o values of 0.5, 1.0. The results of measurements are shown in Figure 4. As can be seen from this plot, the hole boring velocity of He^{1+} ions is approximately linearly proportional to laser a_o.

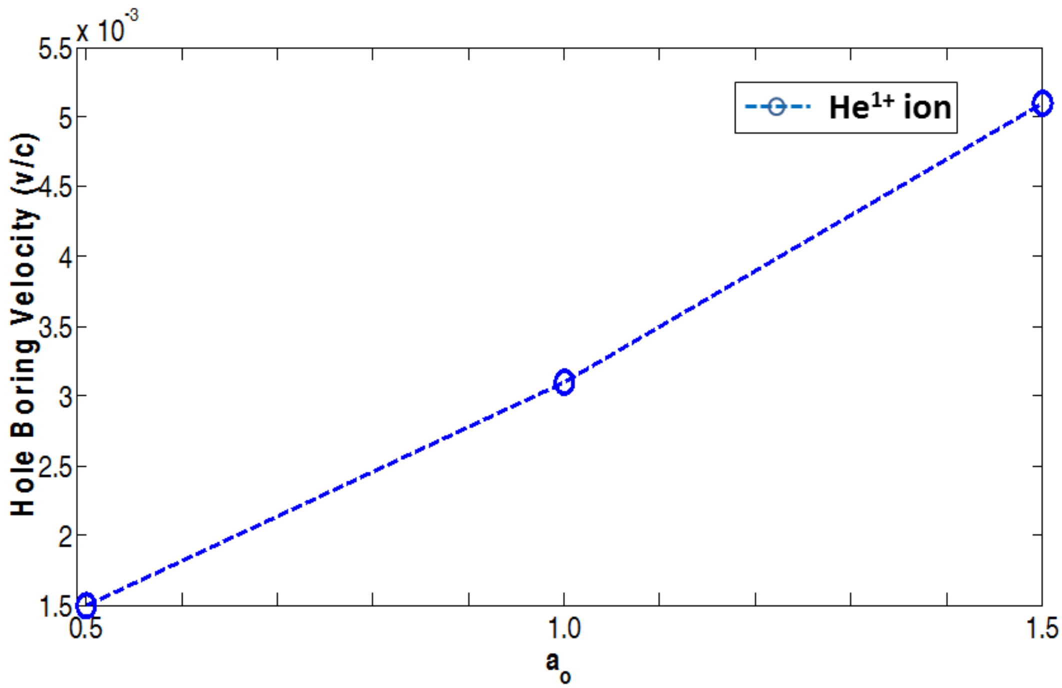

Figure 4: Hole boring velocity as a function of the laser a_o for He^{1+} ions.

Aside from using the Doppler shift method to measure the hole boring velocity. We have also calculated an average hole boring velocity. It was accomplished by directly measuring the distance that the critical density layer is traveling during the interaction e.g. at t = 35ps (see Figure 2a). The hole boring velocity from such measurement is in average 20% lower than one measured from the Doppler method.

2.3.2 Hole Boring Velocity Measurement in a Triangular Plasma Density Profile

Typically, the gas jet plasma doesn't have a constant flat-top density profile but one that can be approximately described by a symmetric triangular shape with a variable density up-ramp length L_r. During the interaction process between the high power CO_2 laser and the plasma, the peak density may reach several n_c due to the density profile steepening pushed by radiation pressure. Therefore, measuring the hole boring velocity in plasma with a triangular plasma density profile is more relevant to the experimental condition.

The parameter setup in 1-D OSIRIS simulation of a triangular plasma density profile with different initial L_r is shown in Figure 5. Simulations involve a single 70ps long CO_2 laser pulse with a_o = 0.5, 1.0, 1.5.

In order to measure the hole boring velocity more accurately by using the Doppler effect, we additionally send an orthogonally polarized 100ps long probe pulse with a very low a_o = 0.01. Because of its very low intensity the probe pulse does not cause any additional perturbation to the plasma, on the other hand because it has an orthogonal polarization w.r.t. the main laser pulse it can be uniquely analyzed upon reflection from the plasma. As shown in Figure 5, a 70ps CO_2 laser pump pulse is incident upon the plasma from left to right. Normalized vector potential (a_o) of the CO_2 laser pulse is chosen as 0.5, 1.0 and 1.5 for three simulation runs for each density profile. The initial triangular plasma density profiles of the three simulation cases have a peak plasma density of 3.0n_c and a 500μm falling edge (FWHM). For the rising fronts, we have simulated cases when L_r are at 500μm, 100μm and 20μm (FWHM).

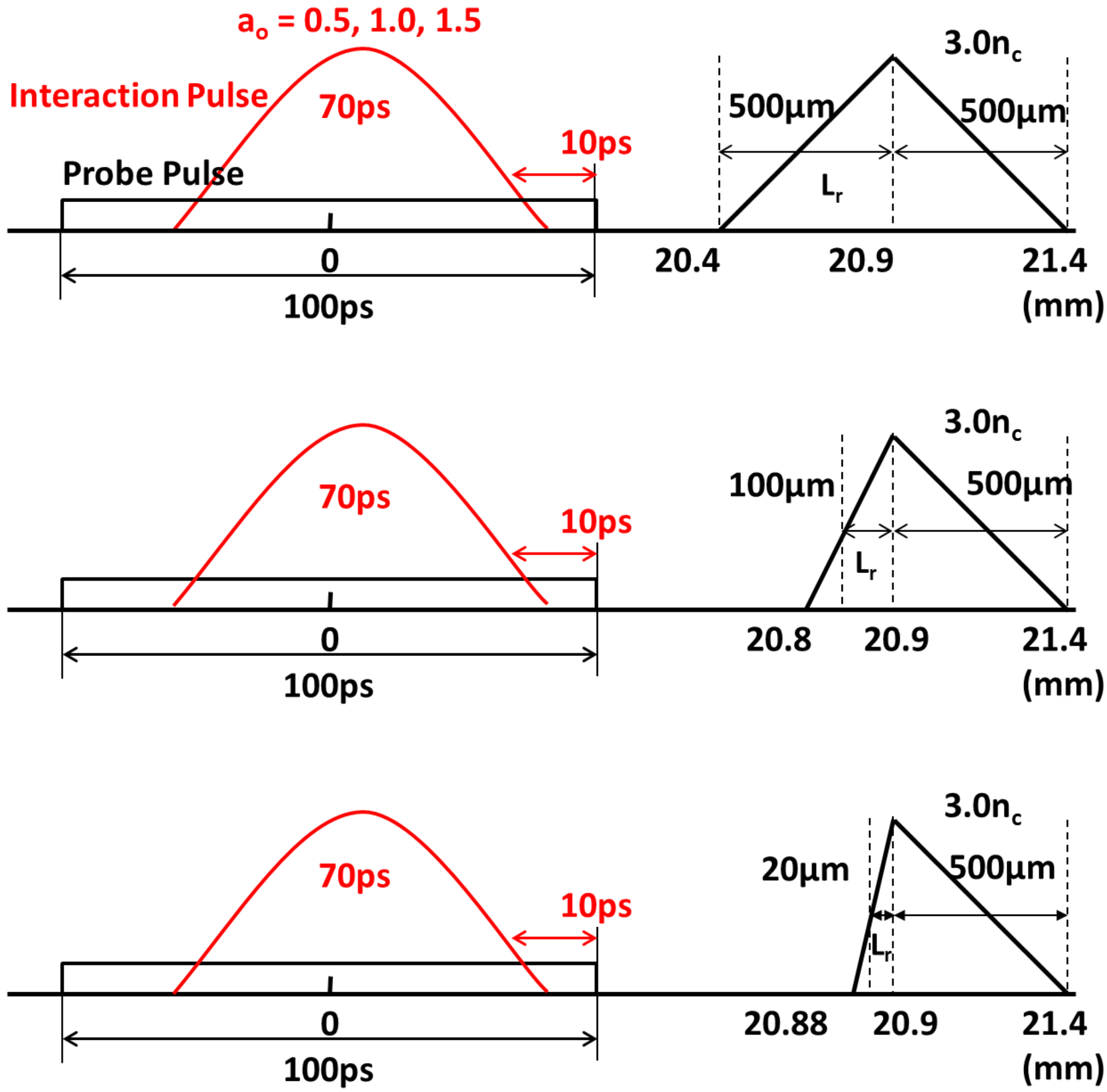

Figure 5: Parameter setup in 1-D OSIRIS PIC code simulations of the hole boring velocity measurement in a triangular plasma density profile.

Table 2 summarizes the parameters used in the simulations.

Parameter	**Value**

Longitudinal Box Size	$12{,}588 \frac{c}{\omega_o}$ = 21.4 mm
Spatial Resolution	$0.2 \frac{c}{\omega_o}$ = 3.4×10^{-4} mm
Time Resolution	$0.2 \frac{1}{\omega_o}$ = 1.1×10^{-3} ps
Time Duration	$30{,}000\frac{1}{\omega_o}$ = 167.1 ps
Charge to mass ratio	7344 (He^{1+})
Pump pulse	$12568 \frac{1}{\omega_o}$ = 70ps, a_o = 0.5, 1.0, 1.5
Probe pulse	$17954 \frac{1}{\omega_o}$ = 100ps, a_o = 0.01

Table 2: Parameter setup in hole boring velocity measurement as a function of a_o with a triangular plasma density profile in He^{1+}.

Figure 6 depicts a snapshot of plasma density profile for a_o = 1.5, τ_l = 70ps (laser pulse length) at the time frame t = 35ps. At this time frame the peak of the laser pulse is incident upon the plasma. The initial plasma density profile has a 20μm rising front and a 500μm falling edge with the peak density at $3.0n_c$.

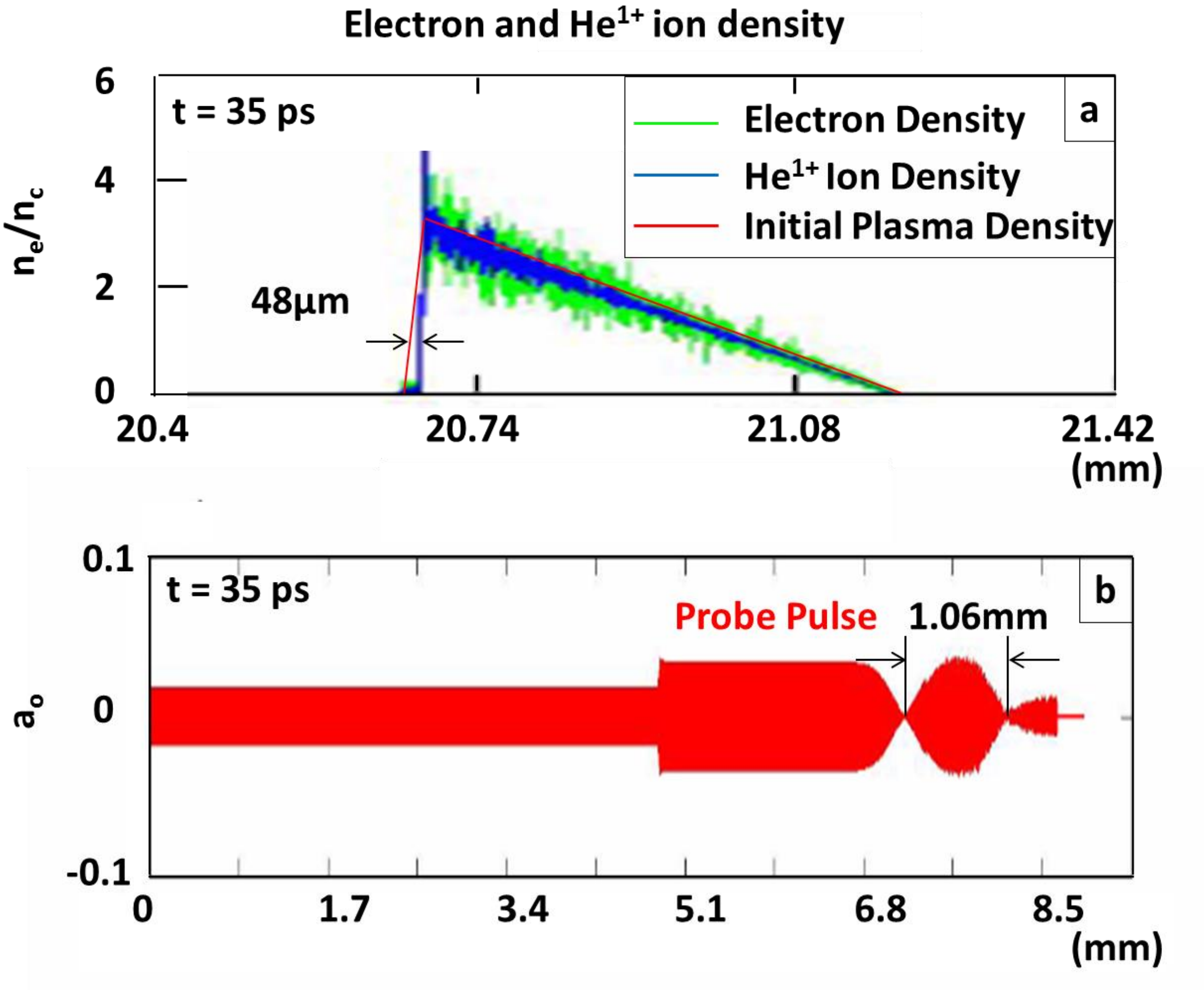

Figure 6: a) A snapshot at t = 35ps of plasma density interacting with the peak of the CO_2 laser pulse. The laser pulse has a peak $a_o = 1.5$. The green line shows the electron density. The blue line shows the He^{1+} ion density. And the red line shows the initial triangular plasma density profile. b) The beat pattern of the probe pulse at the peak of the laser pulse.

In Figure 6 a), we can clearly observe steepening of the plasma density profile driven by the laser pulse. A spatial shift of $n_e = n_c$ layer in the laser propagating direction over the time of t

= 35ps is measured to be 48µm. Based on this direct measurement, we can calculate that the average hole boring velocity over this time period is $v_{hb\_avg} = 4.5\times10^{-3}c$.

The beat pattern of the probe pulse observed in Figure 6 (b) can be used to extract the hole boring velocity using Doppler shift analysis. The node length (L_n) is measured to be 1.06mm and the beating frequency is $v_b = \dfrac{c}{2L_n}$, then following Eq. (5), we calculate the instantaneous hole boring velocity $v_{hb\_int} = 5.02\times10^{-3}c$. Note that two values are in a good agreement but Doppler shift based technique allows for measuring an instantaneous value of v_{hb_int}.

Based on the above methods, we summarize the average and instantaneous hole boring velocities for various density profiles at different a_o in Figure 7.

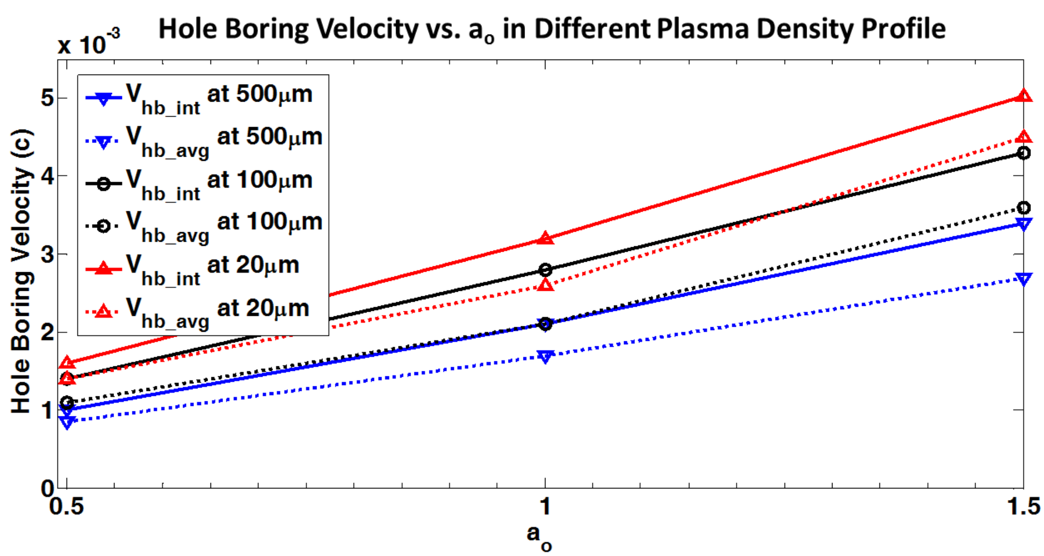

Figure 7: Hole boring velocity measurement as a function of laser a_o for different triangular plasma density profiles. The solid and dashed lines in red, black and blue show the instantaneous

and average hole boring velocities with a 20μm, 100μm and 500μm rising front density profile respectively.

As seen in Figure 7, both v_{hb_int} and v_{hb_avg} increase with an increase in a_o. The measured v_{hb_int} at the laser peak is larger than v_{hb_avg}. These simulations also show that the front ramp length L_r of the plasma density profile has a significant effect on the hole boring velocity. For example at $a_o = 1.5$, when L_r increases from 20 to 500μm, v_{hb_int} drops from 5.02×10^{-3}c to 3.4×10^{-3}c. Such a behavior may be attributed to increase of an underdense part of the plasma for longer ramps. Here, excitation of an electron plasma wave via stimulated Raman scattering at $n_e \leq 0.25 n_c$ can effectively heat up electrons and increase the plasma temperature [28].

For the 20μm rising front simulation case in Figure 5 we also measure the v_{hb_int} at discrete time frames separated with a time interval of 10ps to understand the dynamics of the hole boring velocity within a single 70ps long CO_2 laser pulse. The result of the measurement is plotted in Figure 8.

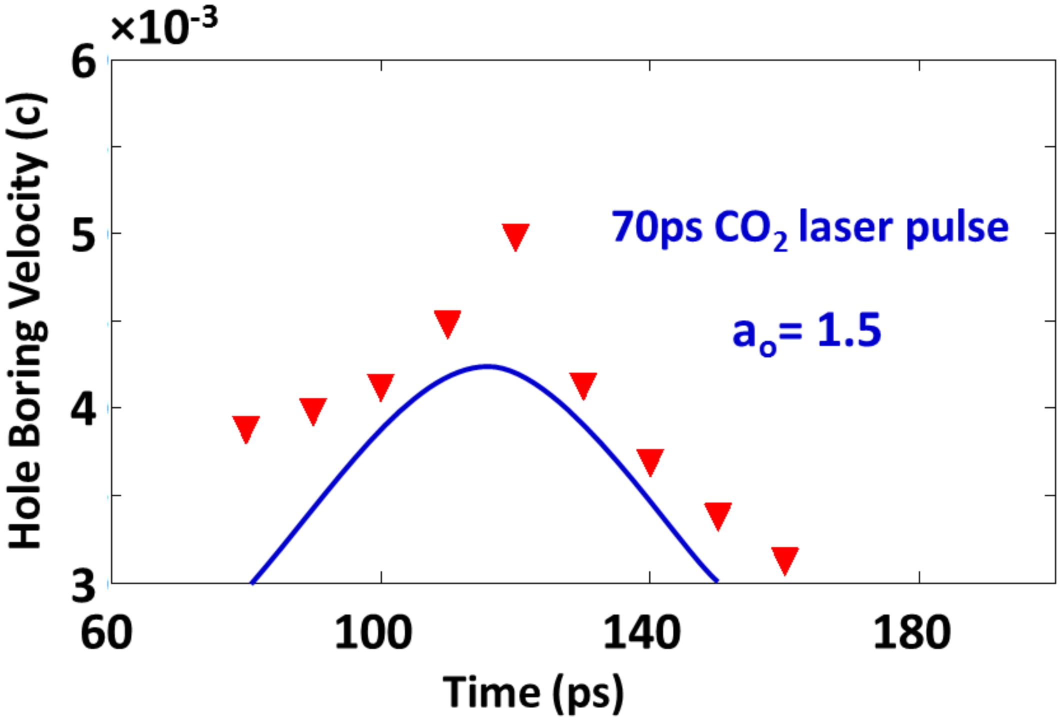

Figure 8: Instantaneous hole boring velocity (v_{hb_int}) as a function of time. Red triangles are the measured data points. Blue line shows the temporal profile of the 70ps long CO_2 laser pulse with a peak a_o = 1.5.

From Figure 8, we can see that the measured hole boring velocities follow the pulse envelope of the incident laser. On the rising edge, when the laser intensity increases, the hole boring speed also increases. The peak hole boring velocity in such case is 5 $\times 10^{-3}$c. It is important to note that on the falling edge, the hole boring velocity slows down faster in comparison with the rising edge. It eventually decreases to $v_{hb_int} = 3.14\times 10^{-3}$c at the laser tail. An interesting fact that we observe is even though the single laser pulse sent into the plasma has a completely symmetric pulse envelope, the measured hole boring velocities have an asymmetry and do not follow the laser profile. The observed behavior indicates the possibility that the thermal pressure may be diminishing the efficacy of the laser radiation pressure. Thus, studying the dynamics of the plasma temperature during this interaction is important.

To understand this plasma heating process better, we extract the plasma temperature dynamics during the laser pulse. But before proceeding further, let us review the definition of the physical notion of 'plasma temperature'. A gas in thermal equilibrium has particles of all velocities, and the most probable distribution of these velocities is known to be the Maxwellian distribution. The one-dimensional Maxwellian distribution is given by

$$f(\mathrm{u}) = A\exp(-\frac{1}{2}\mathrm{mu}^2/\mathrm{kT}_e) \qquad (6)$$

Where $f(\mathrm{u})$ is the number of particles per m^3 with velocity between u and $u+du$, $\frac{1}{2}mu^2$ is the kinetic energy, and k is Boltzmann's constant.

In 1-D OSIRIS simulation, plasma temperature can be measured in the electron phase space as shown in Figure 9 by measuring the plasma density distribution function and extracting plasma temperature T_e based on Eq. (6).

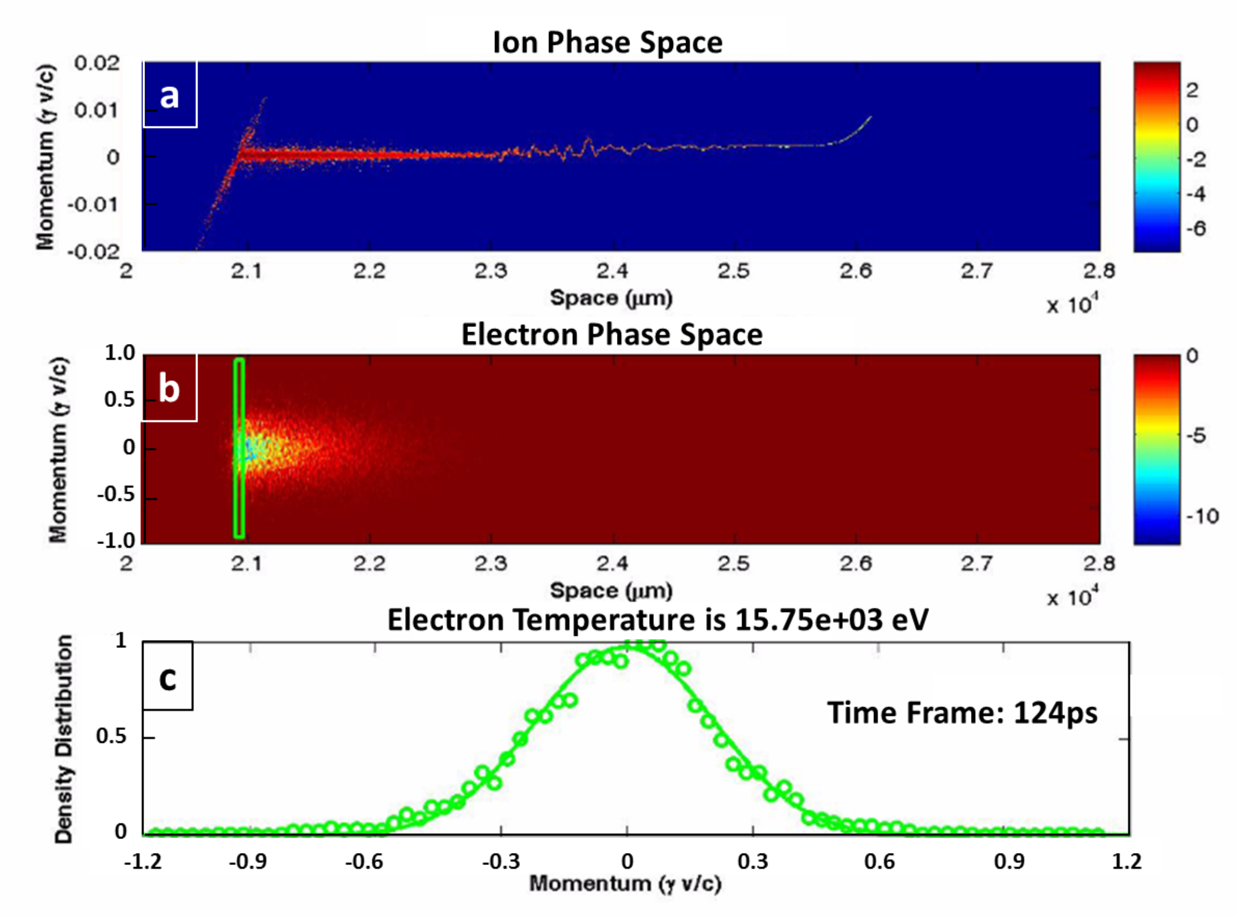

Figure 9: Plasma temperature measurement in electron and ion phase space using 1-D OSIRIS PIC code simulation. The incident CO_2 laser pulse has a Gaussian profile with a 70ps pulse duration and $a_o = 1.5$. Time frame of the selected snapshot is 124ps. Initial plasma has a triangular density profile with a 20μm (FWHM) rising edge and a 500μm falling edge. The peak plasma density is $3.0n_c$. a) shows the ion phase space. b) shows the electron phase space and c) shows the extracted plasma temperature.

Figure 9 shows the ion phase space and the electron phase space at one of the later frames t = 124ps. Plasma is already hot and the width of the plasma density distribution in the momentum axis represents its T_e. We are interested in changes of the plasma temperature where the CO_2 laser pulse is stopped (t = 124ps). Thus a very thin box (shown in solid green line) is drawn to cover the plasma density distribution around the critical dense layer. Within the green box the density is integrated and normalized along the spatial direction and plotted in Figure 9 c). A Gaussian function is used to fit all the data points (shown by green circles) and the plasma temperature from the fitting curve (shown by solid green line) is extracted using Eq. (6). Temperature measured at this time frame is ~16keV.

Based on the above method, the plasma temperature versus time is plotted in Figure 10 as below.

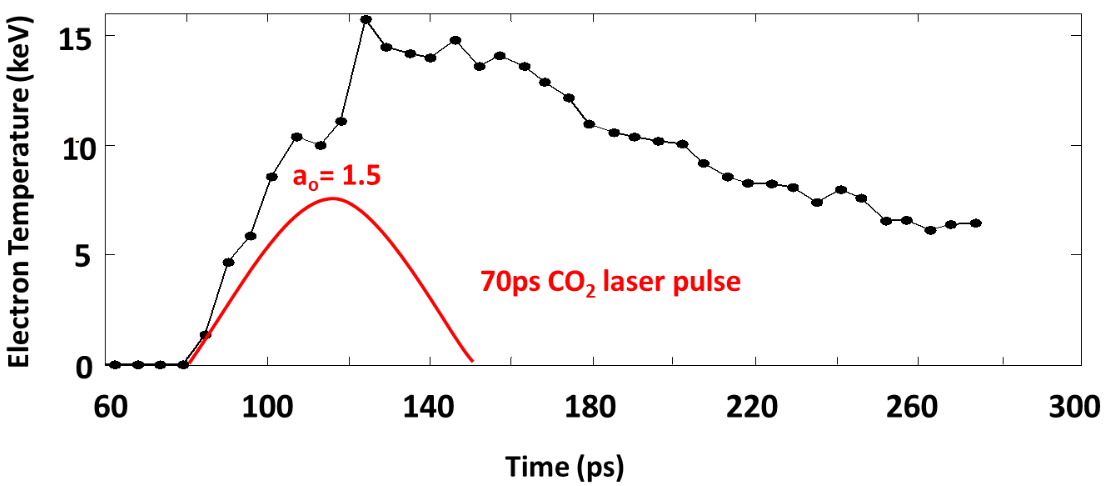

Figure 10: Plot of plasma temperature T_e versus time. Measured data points are shown in black dots. Red line indicates the temporal profile of a 70ps CO_2 laser pulse.

From the plasma temperature measurement we can draw several conclusions: First, the peak plasma temperature of ~16keV occurs at 124ps which is 9 ps after the laser peak (t = 115ps).

In other words, up to this point the plasma heating rate exceeds the plasma cooling rate. This might be expected during the time the laser intensity is increasing. The most energetic of the heated electrons will leave the plasma creating a target potential that confines the bulk of the heated electrons. These electrons will reflux through the plasma virtually decoupled from the ions and the cold electrons and cool very slowly as the plasma expands. From its peak value, the plasma temperature drops to half of its value in 80ps. In fact at the end of the laser pulse at 150ps, the plasma temperature is still ~14keV. It is thus not surprising that once heated, the plasma will continue to exert a significant thermal pressure thereby causing the hole boring velocity to rapidly decrease as the laser intensity begins to drop on the falling edge of the laser pulse as shown in Figure 8.

2.3.3 Hole Boring Velocity and Plasma Temperature Measurement in Laser Pulse Train

Finally, we study the interaction between the helium gas plasma and a series of CO_2 laser pulses to understand the time evolution of hole boring close to our experimental condition. Note that in the next chapter we will explain the origin of temporally structured CO_2 laser pulses. Plasma temperature is monitored in sequential time frames to study the competition between the thermal pressure $P_{th} = n_e k_B T_e$ and laser radiation pressure $P_L = (1+\mathrm{R})\,\mathrm{I}/\mathrm{c}$, where R is the plasma reflectivity. The threshold of the observation of laser hole boring is related to a certain $I\lambda^2$ value when P_L exceeds P_{th}.

The simulations involve a CO_2 laser macropulse which consists of five micropulses. Each micropulse has a 3ps pulse width and is separated from the adjacent one by 18ps. Normalized vectors potentials of the 5 micropulses are set as 0.5, 1.0, 1.5, 1.0, 0.5 in symmetry. A 200ps long probe pulse with a_o = 0.01 is sent simultaneously into the plasma as the diagnostic for hole boring effect based on Doppler shift. The plasma has a triangular density profile with a 20µm rising front and 500µm falling edge (FWHM). The simulation setup is shown in Figure 11 as below.

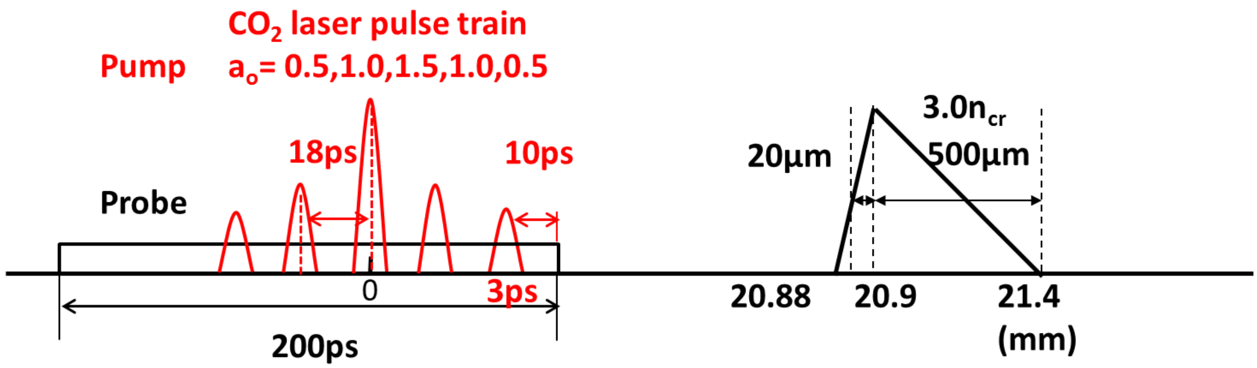

Figure 11: Parameter setup in 1-D OSIRIS PIC code simulations of hole boring velocity and plasma temperature measurements with a CO_2 laser pulse train interacting with a triangular helium gas plasma. Five 3ps CO_2 laser micropulses with 18ps separation from each other are incident upon the plasma from left to right. A 200ps long probe pulse with $a_o = 0.01$ is sent simultaneously into the plasma for hole boring velocity measurement by Doppler shift. The initial triangular plasma density profile has a peak plasma density at $3.0n_c$ and a 20µm rising front and 500µm falling edge (FWHM).

Table below summarizes all the parameters used in the simulations.

Parameter	**Value**
Longitudinal Box Size	$12{,}588 \frac{c}{\omega_o} = 21.4$ mm
Spatial Resolution	$0.2 \frac{c}{\omega_o} = 3.4\times10^{-4}$ mm

Time Resolution	$0.2 \frac{1}{\omega_o} = 1.1\times10^{-3}$ ps
Time Duration	$60{,}000\frac{1}{\omega_o}$ = 334.2 ps
Charge to mass ratio	7344 (He^{1+})
Pump pulse	5 micropulses with individual pulse length of $538.6 \frac{1}{\omega_o}$ = 3ps and 18ps pulse separation, a_o = 0.5, 1.0, 1.5, 1.0, 0.5
Probe pulse	$35906 \frac{1}{\omega_o}$ = 200ps, a_o = 0.01

Table 3: Parameter setup in hole boring velocity and plasma temperature measurement with a CO_2 laser pulse train interacting with a triangular helium gas plasma.

For hole boring velocity, we use the Doppler effect procedure presented earlier to measure v_{hb_int} for time frames separated by an interval of 10ps. This allows for taking into account the interaction between each individual laser micropulse and the plasma. The measurement result is shown in Figure 12.

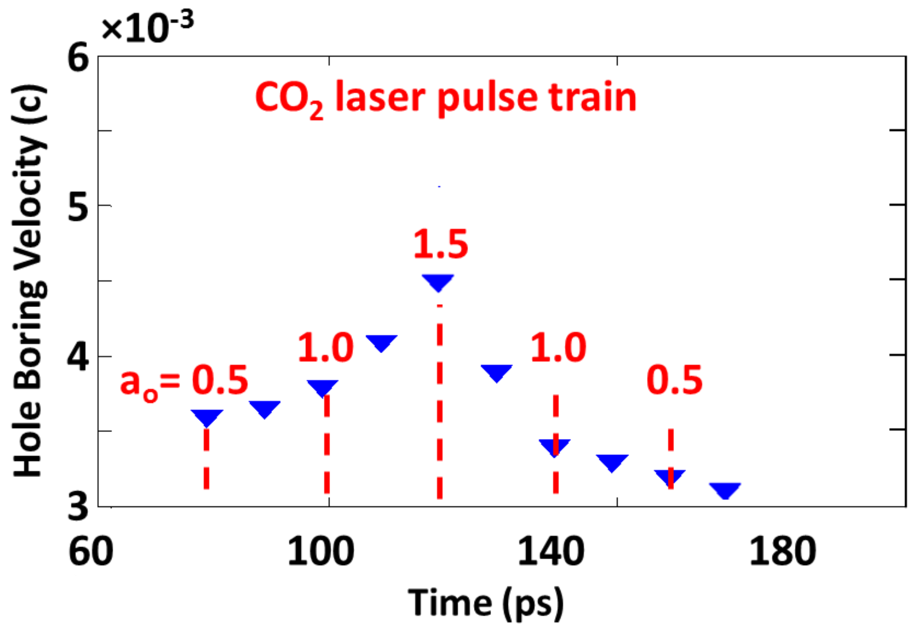

Figure 12: Instantaneous hole boring velocity (v_{hb_int}) as a function time during the interaction with the CO_2 laser pulse train. Blue triangles are the measured data points. Red dashed lines indicate the temporal structure of the incident laser pulse.

As seen in Figure 12, the peak hole boring velocity measured as the most intense laser micropulse ($a_o = 1.5$) strikes the plasma is 4.5×10^{-3}c. Note that for a 70ps pulse, peak hole boring velocity is 5×10^{-3}c. This indicates a more effective push of the critical density layer due to the continuous radiation pressure exerted by the single pulse at similar peak power. Of course the single 70ps pulse contains roughly 8 times more energy than the sum of the energy contained in the individual micropulses within the macropulse of the same peak intensity. On the falling edge of the pulse train, the hole boring velocity is still measurable as $v_{hb_int} = 3.2\times10^{-3}$c when the last laser micropulse has passed. And a similar asymmetric hole boring velocity profile is observed.

The plasma temperature is measured in the electron phase space using the similar procedure applied in the single smooth pulse case.

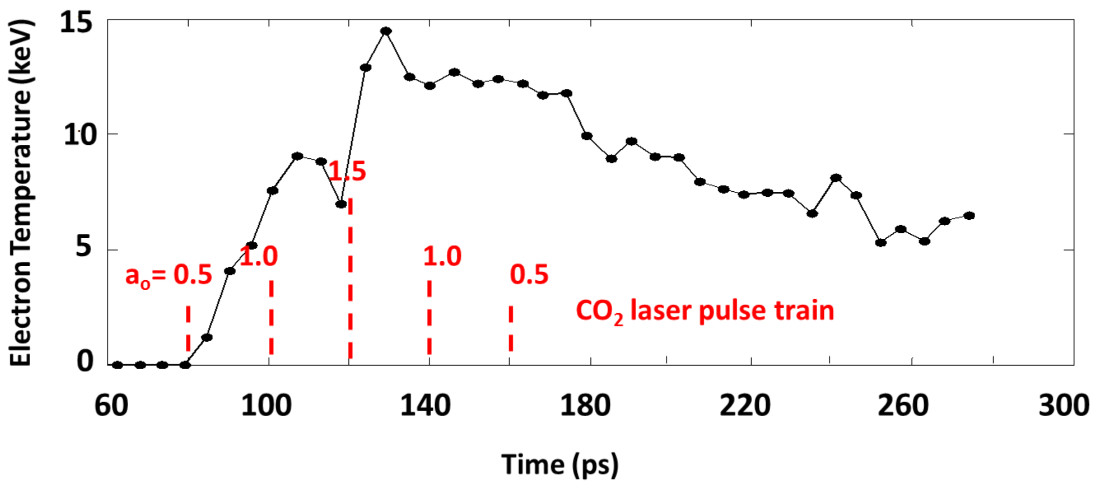

Figure 13: Plot of plasma temperature T_e versus time. Measured data points are shown in black dots. Red dashed lines show the temporal structure of the incident CO_2 laser pulse train.

The overall plasma temperature evolution in the two cases (Figure 10 v.s. Figure 13) is very similar as expected. In both cases the plasma reaches its peak temperature after the peak intensity and thereafter cools more slowly as the laser intensity drops compared to the temperature increase during the rise of the laser intensity. In the case of the train of micropulses, the plasma can show some "cooling" in between the 2nd and 3rd and 3rd and the 4th micropulses as well. In 1D simulations that do not model self-focusing and filamentation or for the matter resonance absorption, one does not expect to see a great deal of difference in the mechanisms that cause the plasma electron heating ($j \times B$ and Raman scattering) between these two cases.

2.4 Summary

In this chapter, we have used the 1-D OSIRIS PIC code to study the laser hole boring phenomenon for different laser and plasma conditions. The interaction of a single 70ps CO_2 laser pulse is compared with a train of 3ps pulses separated by 18ps, both pulses having the same peak intensity. The average hole boring velocity deduced directly by measuring the displacement of the critical density point v_{hb_avg} is compared with the instantaneous hole boring speed v_{hb_int} measured using the Doppler shift of a probe pulse. The v_{hb_int} measured at the laser peak is seen to be higher by approximately 20% than v_{hb_avg}. The density scale length of the rising density edge of the plasma affects the hole boring velocity. When the rising front of the density profile increases from 20μm to 500μm, for the same laser intensity and pulse duration, v_{hb_int} drops from 5.02×10^{-3}c to 3.4×10^{-3}c. The maximum hole boring velocity for a smooth laser pulse that has the same peak intensity as a time structured pulse containing several individual micropulses is greater due to the continuous push on the plasma provided by the single pulse as expected.

The most important physics conclusion is that regardless of CO_2 laser pulse profile the hole boring process is determined by a balance between the radiation pressure P_L and thermal pressure P_{th}. As a result of this competition, v_{hb} first increases during the risetime of the laser pulse where $P_L > P_{th}$ but the hole boring efficacy is reduced during the falling edge because the plasma electrons once heated cool slowly causing more rapid fall of v_{hb}.

CHAPTER 3

3. The Neptune CO_2 Laser System

3.1 CO_2 Laser and Amplification of Short Pulses

For the work described in this dissertation, high-power 10μm pulses for laser-plasma studies in near critical density regime were generated by a CO_2 Master-Oscillator-Power-Amplifier (MOPA) system at the UCLA Neptune laboratory. We describe how this was done and the resultant train of short pulses that this method of generating short pulses necessarily produces. This train of pulses together with the four frame interferometry technique for probing the plasma was critical to measuring the intensity dependence of the hole boring velocity in a plasma that was first being heated (during the intensity increase of the envelope of the CO_2 pulse train) and subsequently was slowly cooling down (during the intensity decrease of the envelope of the laser pulse train).

The upper lasing levels in the rotational-vibrational states of the CO_2 molecules provide metastable levels for the CO_2 laser gain medium. These states can generally be excited by an electrical discharge through inelastic collisions between the energetic electrons and the gas molecules. The CO_2 gas is usually mixed with N_2 and He to produce a strong population inversion in the CO_2 molecules. For N_2 molecules, their first excited vibrational level is metastable and coincides with the upper lasing level of the CO_2 molecules (00^o1). Thus, the stored energy of N_2 molecules can be efficiently transferred to the CO_2 molecules through collisions. Helium is also added into the gas mixture due to its high thermal conductivity, which can efficiently cool down the CO_2 gas and also depopulate lower CO_2 lasing levels via collisions.

Therefore, a combination of these three gases under the electrical discharge condition can effectively excite the CO_2 molecules into the population inversion states, which are suitable for the amplification of the seed pulse.

Conventionally, CO_2 laser operating on a single rotational-vibrational transition under the atmospheric pressure lacks the necessary bandwidth to support the amplification of a picosecond long laser pulse. For instance, at 1 atmosphere (henceforth atm), the gain spectrum of the 10P rotational-vibrational manifold centering at 10.6μm consists of a series of rotational transitions separated by 55GHz and each transition has a bandwidth of ~3.5 GHz (gas mix of 1:1:14 CO_2: N_2: He). Therefore, the maximum pulse length that can be amplified is ~1ns due to this bandwidth limitation. In order to amplify sub-ns pulses, the bandwidth must be broadened. One way to achieve this goal is to rely on collisional broadening to enlarge the bandwidth. And this can be done through increasing the pressure of the CO_2 gain medium. The following equation shows the collisional bandwidth of the rotational line in a relation to the pressure of the gas mixture:

$$\Delta v_{pressure} = P \bullet (5.79\psi_{CO_2} + 4.25\psi_{N_2} + 3.55\psi_{He}) \tag{7}$$

Here $\Delta \nu_{\text{pressure}}$ is the bandwidth of the pressure-broadened rotational line in GHz, P is the pressure of the gas mixture in atm, and ψ is the fraction of a particular gas in the mixture. The calculated gain spectrum for the 10P branch of the 00^o1-10^o0 vibrational band of the CO_2 molecule is shown in Figure 14 at three pressures (1, 10, and 25 atm). A 37 GHz bandwidth is achievable through the pressure broadening at 10 atm. The neighboring rotational lines are observed to merge together under this high pressure. The ideal scenario for picosecond pulse amplification would be production of a continuous spectrum across the entire vibrational branch, which covers a 1.2 THz bandwidth. This case happens at ~25 atm pressure in the simulation. Although, with such bandwidth, a ~3ps pulse can be amplified directly, this pressure is too high for a stable discharge in gas that has a few centimeter spacing between the electrodes.

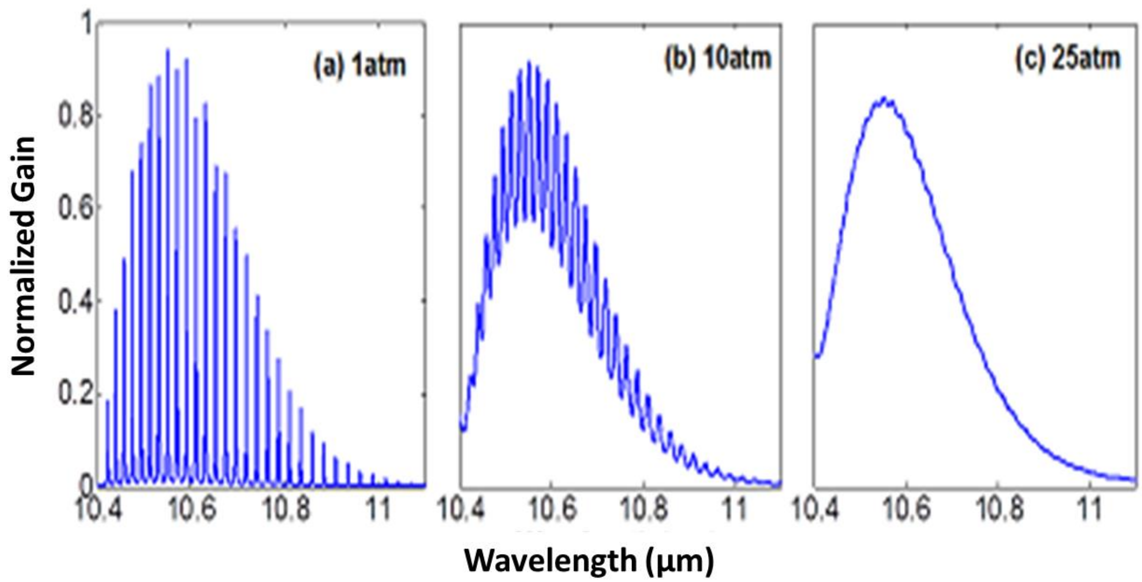

Figure 14: CO_2 gain spectrum vs. wavelength with a gas mixture of 1:1:14 (CO_2: N_2: He) at pressure of 1 atm (a), 10 atm (b), and 25 atm (c). x-axis shows the wavelength and y-axis shows the normalized gain.

For a pressure less than 10 atm, a picosecond CO_2 laser pulse can still be amplified, however, its spectrum covers multiple rotational lines in the gain medium. Under this condition, the spectrum of the seed pulse will be filtered by the CO_2 gain spectrum after amplification and results in 55 GHz modulation (Shown in Figure 15(a)). Applying the Fourier transform to the modulated spectrum, the resultant temporal structure of the laser pulse becomes a train of 3ps long micropulses with a 1/55 GHz = 18ps separation. The entire pulse train is referred to as the 'macropulse' and each individual pulse inside the pulse train is referred to as the 'micropulse'.

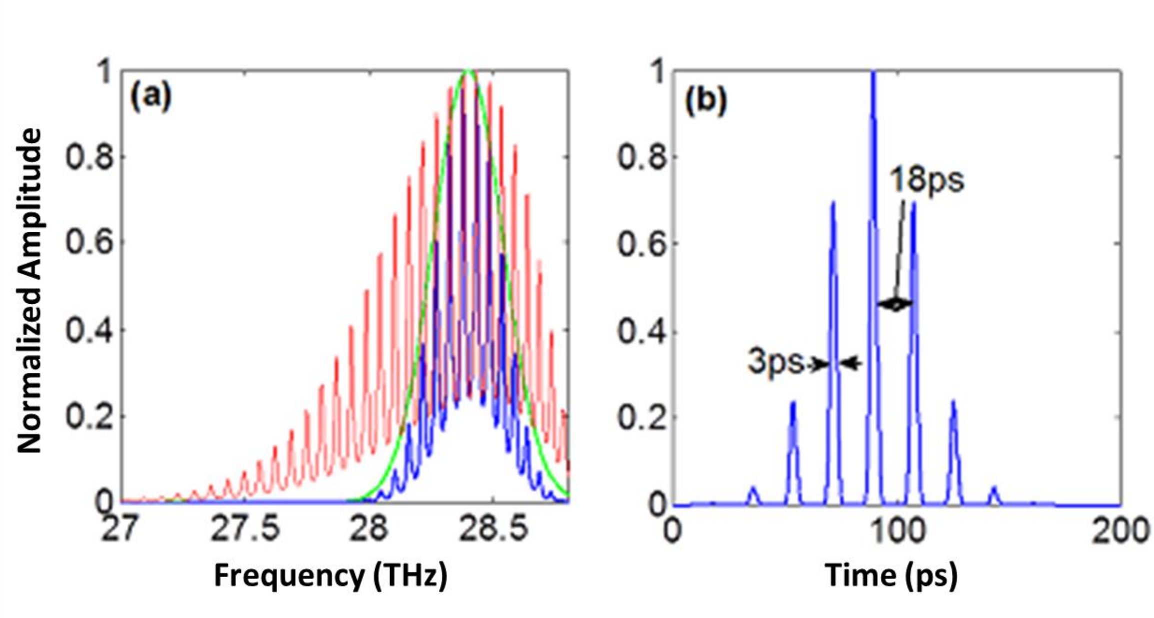

Figure 15: (a) CO_2 gain spectrum at 5 atm (red), 3ps input seed pulse spectrum (green), and the pulse spectrum filtered by the CO_2 gain spectrum obtained via multiplication of the red and green traces (blue). (b) Fourier transform of the pulse spectrum filtered by the CO_2 gain medium shows a train (the macropulse) of individual 3ps long micropulses.

Figure 15(a) shows the spectra of a 3ps input pulse before and after interacting with a 5 atm CO_2 laser gain medium with a gas mix of 1:1:14 (CO_2:N_2:He). The CO_2 gain spectrum (red), the 3ps input pulse spectrum (green), and the pulse spectrum filtered by the CO_2 gain spectrum via multiplication of the red and green traces (blue) are plotted. Figure 15(b) shows the temporal structure of the resultant macropulse from this interaction through the Fourier Transform. An expected pulse train structure is achieved.

Through analyzing the results simulated by the codes written by V. Platonenko [29], we can draw two conclusions. First, through the interaction, a CO_2 laser macropulse consisting of a series of 3ps micropulses with an 18ps separation is produced. Second, each micropulse still preserves a 3ps time duration due to the much broader bandwidth ~1.2THz of the entire 10P vibrational branch.

3.2 Neptune CO_2 Laser MOPA Systems

Now we describe how a high power train of picosecond pulses were produced in our laboratory.

Figure 16 shows schematically the CO_2 master oscillator - power amplifier (MOPA) system [30] which consists of three major stages:

1. First stage is a Hybrid Transversely-Excited Atmospheric-pressure (TEA) master oscillator which produces a 2ps, ~nJ level seed pulse.

2. Second stage relies on a regenerative amplifier module working at 8atm pressure to boost the energy of the produced seed pulse up to mJ level.

3. Third stage involves a large-aperture (20 x 35 cm^2) 2.5 atm CO_2 module which further amplifies the laser pulse to ~60J.

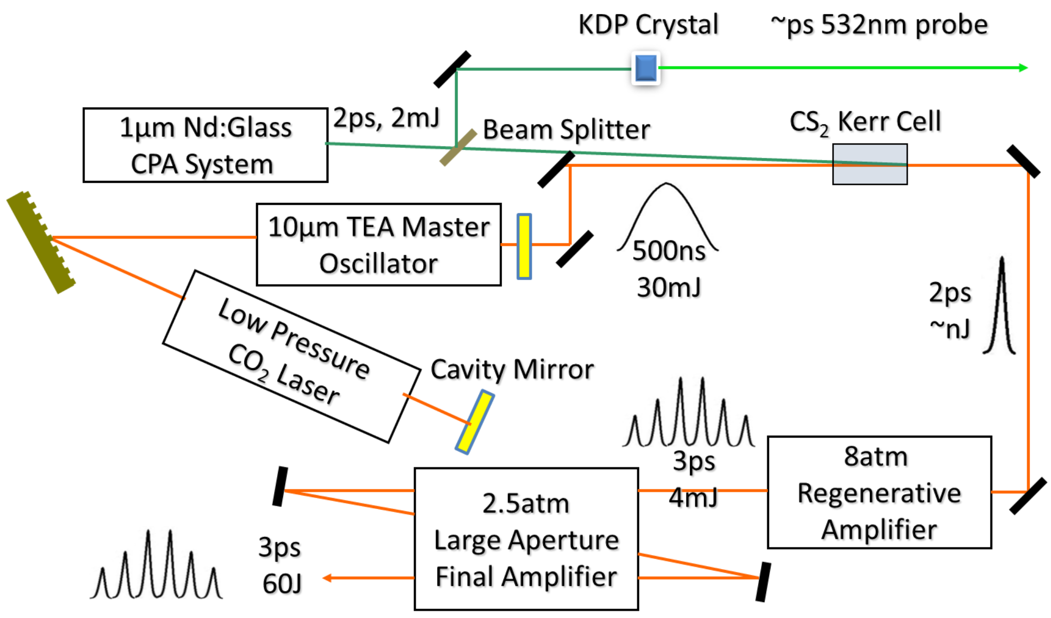

Figure 16: The Neptune CO_2 Master-Oscillator Power-Amplifier (MOPA) laser system. Three amplification stages include a 10µm TEA Master Oscillator, an 8atm Regenerative Amplifier and a 2.5atm Large Aperture Final Amplifier. Part of 1µm beam is redirected to the KDP crystal to produce a second harmonic generation (532nm) for plasma probing.

3.3 Picosecond 10µm Seed Pulse Production

As previously mentioned the CO_2 molecule does not have enough bandwidth to amplify picosecond long pulses, therefore, the commonly used mode-locking technique is not applicable for production of a picosecond CO_2 laser seed pulse. In order to compensate for this bandwidth limitation, a short 2ps 1µm laser pulse produced by the solid state laser is used as an optical gate to switch a ~3ps portion from a 200ns long CO_2 laser pulse.

For this purpose, Nd: Glass CPA system as shown in Figure 16 is used to generate the 2ps long 1μm laser pulse. Part of the 1μm beam (~40%) with energy of ~1mJ is directed into a KDP crystal to generate a second harmonic ≤ 2ps, 532nm pulse for plasma probing. The rest of 1μm energy is used to gate the 10μm pulse. There are two ways to produce a picosecond long 10μm seed pulse by using a short 1μm pulse. They are semiconductor switching technique and ultrafast Kerr modulator [31]. The advantage of Kerr effect is that it's proportional to the intensity instead of fluence of the gate pulse and therefore requires less energy for switching [32]. We have adopted a two stage switching where a ~3ps long 10μm pulse is first produced via a Kerr modulator placed between two crossed polarizers and then a Ge reflective switch is used to increase the contrast of the seed 10μm pulse.

The optical Kerr Effect in a nonlinear medium relies on dependence of the refractive index of the material (through which the CO_2 laser propagates) on the intensity of the pump pulse (1μm):

$$n(\mathrm{I}) = n_o + n_2 I^2 \tag{8}$$

Where, n_o is the linear index of refraction, n_2 represents the nonlinear refractive index in the medium, and I is the intensity of the 1μm pump pulse in units of W/cm^2. Due to the high intensity of the 1μm pulse, a birefringence effect is induced in the nonlinear (Kerr) medium along its polarization direction. The refractive index along the polarization direction of the 1μm will change for a weaker 10μm pulse and the nonlinear medium will behave like a transient phase retarder. An ideal scenario for such polarization-based switch is the polarization direction of the 10μm is rotated by 90° after the laser pulse propagates through the entire nonlinear medium. And this requires the following condition being satisfied:

$$| n(\mathrm{I}) - n_o | = \frac{\lambda}{2d} \tag{9}$$

Where $n(I)$ is the refractive index, λ = 10μm, and d is the total length of the Kerr medium.

Carbon disulfide (CS_2) is chosen as the Kerr medium for the reasons that it is transparent for both 1μm and 10μm radiation and also has a large nonlinear refractive index of n_2= 2×10^{-14} cm^2/W [33]. Besides, for the pump pulse (1μm) and probe pulse (10μm), the group velocity dispersion in the nonlinear medium CS_2 is measured as ~1ps/cm, thus the length of the Kerr cell is confined below 2.5cm to avoid the significant stretching of the 10μm seed pulse. Based on the above equations(8), (9) and parameters, a 90° rotation requires a 1μm laser pulse of 10 GW/cm^2, which is achievable for a picosecond long pulse.

A TEA CO_2 oscillator is used to produce the 10μm pulse in the MOPA laser system. A low pressure (~30Torr) CO_2 amplifier is introduced into the laser cavity along with the TEA module and this so-called hybrid system can provide a single longitudinal mode output with an energy of ~30mJ in a 200ns long CO_2 laser pulse. The laser pulse then co-propagates with the 1μm into the Kerr cell with a ~2° crossing angle. A ~3ps portion of a long nanosecond pulse is switched out due to the polarization control. Then a 6-plate Ge analyzer (II-VI Inc., model: PAG-15-AC-6) with a measured contrast of 1×10^5 is used to filter out the pulse. After the analyzer, the 10μm pulse is delivered to a 1μm controlled Ge semiconductor switch to boost the contrast further. For this system, the 1μm pulse is incident on the Brewster angled Ge plate by a few picoseconds earlier than the 10μm and produces a layer of electron-hole surface plasma, which induces a reflection of the 10μm beam. Eventually, a 3ps, nJ level, 10μm seed pulse that has a Gaussian profile is produced. This level of energy is sufficient for injection mode-locking of the high-pressure CO_2 regenerative amplifier.

3.4 CO_2 Regenerative Amplifier

The generated 3ps 10μm seed pulse is then sent into an 8 atm TE CO_2 module for further amplification. The laser has a gain volume of $1\times1\times60$ cm^3 and is filled with a mixture of gas of CO_2, N_2 and He. The ratio of each gas in the mixture is 1:1:14 (CO_2:N_2:He). Through a 50% ZnSe input coupler, the regenerative amplifier is injection mode-locked by the 3ps seed pulse. As a result, a train of 10μm pulses separated by an ~12ns cavity roundtrip time is produced. The total energy is boosted from nJ to ~80mJ with a cavity gain of ~10^7.

The injection mode-locked pulse train essentially follows the same beam path of the input seed pulse but is decoupled due to the transmission through the Ge reflective switch, since surface plasma produced earlier has already decayed. Then, a single pulse from this "mode-locked train of pulses" with a maximum energy ~10mJ is selected by a CdTe Pockels cell located between a set of crossed polarizers. For this single pulse selector, the throughput is ~40%, leaving a ~4mJ seed pulse for a further amplification in the final amplifier.

3.5 Final Amplification

A large-aperture (20×35 cm^2) amplifier pumped by the electron-beam controlled discharge is employed for the final amplification. A total gain of G_o~15,000 is provided through 3 passes in the gain medium with a total length of 7.5m. This increases the seed pulse energy from ~4mJ up to ~60J.

The input beam sent through the final amplifier for the first pass is quasi-collimated with a beam radius of w_o = 4 mm. This provides an input intensity ~200MW/cm^2. A total measured gain after the first pass is G_o ~100 which brings the laser intensity up to 20GW/cm^2.

For the second and third passes in the final amplifier, the beam radius is designed to increase from w_o =1cm to 6.25cm for two purposes. The first one is to extract a large amount of energy through the interaction with the gain medium. And the second is to prevent the laser damage on the NaCl window located on the output side of the amplifier. The total measured gain of these two passes is G_o~150 and the CO_2 laser energy can eventually be boosted up to ~60J.

An interesting phenomenon worth mentioning is the significant broadening of the rotational line bandwidth of CO_2 molecules due to the ac Stark Effect [34] is observed during the amplification due to the sufficiently high intensity of the CO_2 laser pulse in the final amplifier. This process is commonly known as 'field broadening', which can compensate for the lack of bandwidth in low-pressure amplifiers. Based on our study, when laser intensity $I < 4$GW/cm^2, pressure broadening dominates. When $I > 4$GW/cm^2, field broadening can also make a significant contribution for producing a short macropulse envelope.

3.6 Summary

In this chapter, we have described the CO_2 Master Oscillator-Power Amplifier (MOPA) laser system used in the experiment. This three-stage laser amplification system has the capability of boosting a 3ps, 10μm seed pulse from nJ up to 10s of Joules level. The peak power of the produced laser pulse can reach ~TW level. Simulations show the amplification of a 3ps CO_2 seed pulse in a gain medium at pressure of 8atm will result in a pulse train consisting of a series of 3ps long pulses separated by 18ps defined by separation of rotational lines of CO_2 molecules. The entire laser pulse train is referred as a 'macropulse' and each individual pulse inside it is referred as a 'micropulse'. A focused CO_2 laser beam can reach intensity of $\leq 10^{16}$ W/cm^2 and ionize He, H_2 gas. Temporal structure of the CO_2 laser pulse favors laser hole boring study, because it allows the measurement of the motion of the laser produced cavity during and between the laser micropulses.

CHAPTER 4

4. Experimental Setup

4.1 Target Chamber

In the past experiments [35], the target chamber window size limited the maximum CO_2 laser beam diameter to 4". For the LPI study, a new larger target chamber, which can accommodate a beam with a maximum 7" diameter, was installed. The experimental arrangement in the target chamber is shown in Figure 17.

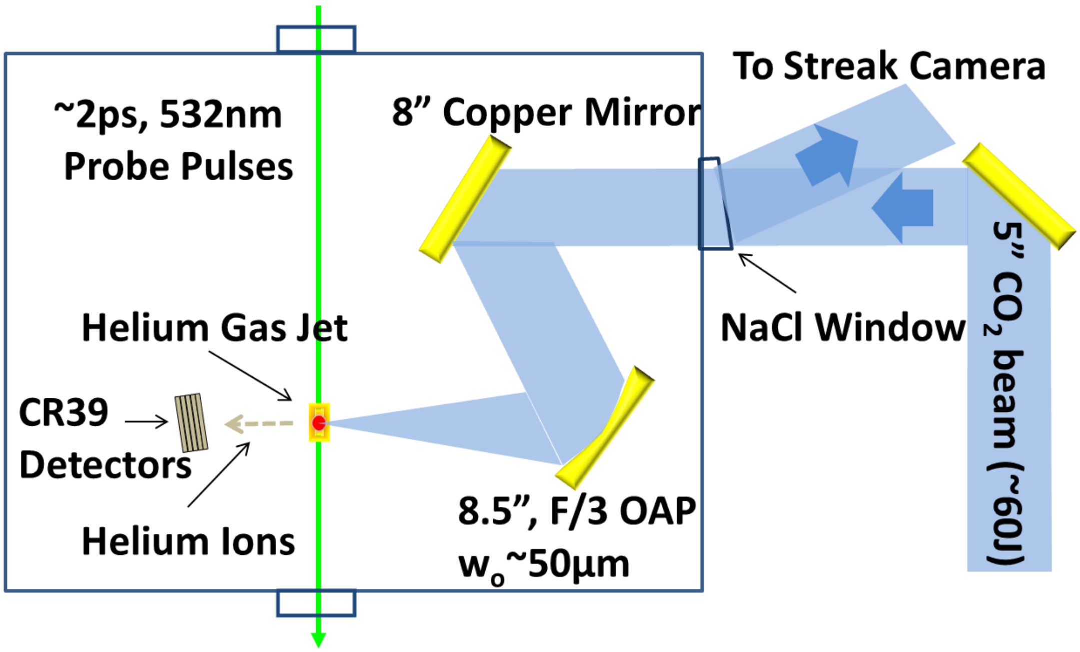

Figure 17: Schematic of LPI experimental setup in the target chamber. CR39 is a stack of plastic nuclear detectors used to detect forward emitted He ions from the plasma. See section 5.5 for results obtained with this diagnostic.

After three stages of amplification, a 5” diameter CO_2 laser beam with energy of ~60J is sent into the target chamber through an 8” diameter salt (NaCl) window. The salt window is mounted on the top of a 4^o wedge. A 4% reflection of the laser beam is directed to a streak camera diagnostic for synchronization of the CO_2 train of pulses and the four green laser pulses used for interferometry. The CO_2 laser pulse inside the target chamber is reflected first by an 8” diameter copper mirror and then focused onto a 1.4mm diameter helium gas jet by an 8.5” F/3 off-axis parabolic mirror (OAP). Behind the gas jet, ~15cm away, a stack of 10cm × 10cm CR-39 detectors is mounted on the same height along the laser axis to monitor the forward propagating stream of helium ions. A ~2ps, 532nm probe pulse is incident from the side port of the target chamber to probe the plasma. Outside the target chamber, two CCD cameras are installed on the side and top to facilitate the process of positioning the gas jet in the focus of CO_2 laser beam with a precision better than 20μm. For this purpose, a tunnel-ionized plasma by a high-power CO_2 laser pulse in ~200 mTorr of Ar was utilized.

4.2 2ps, 532nm Probe Pulse Generation and Transport

To study the complex dynamics of interaction between the temporally modulated high power CO_2 laser macropulse and near critical density plasma, a diagnostic system based on Mach-Zehnder laser interferometer is set up around the target chamber.

For this diagnostic, it is critically important to choose an appropriate probe pulse. This requires considering the probe wavelength, the necessary temporal resolution and the alignment and transportation of the probe pulse to the plasma. Furthermore, possible refraction of the probe beam by plasma also needs to be taken into account. Density gradient of the plasma in the transverse direction from the probe can be translated into a refractive index gradient based on Eq. (10).

$$n_p = \sqrt{1 - \frac{\boldsymbol{n_p}}{\boldsymbol{n_c}}} \tag{10}$$

Where n_p is the refractive index of plasma, $\boldsymbol{n_p}$ is the plasma density, and $\boldsymbol{n_c} = (4\pi^2 \, \mathrm{m}_{\boldsymbol{e}} \, \varepsilon_{\boldsymbol{o}} \, \mathrm{c}^2)/(\mathrm{e}^2 \, \lambda^2)$ is now the critical density of the plasma for the probe light.

It is the refractive index gradient that will affect the propagation of the probe in the plasma. Even though, this refraction will not change the first order phase information, it can cause signal losses and therefore distort/blurr the generated interferograms. By using a simple geometric analysis, the refraction angle θ of the probe light propagating through an inhomogeneous medium can be expressed as $\theta = \frac{L}{n_o}(\frac{dn}{dx})$ [36], where L is the length of the medium, n_o is the average index of refraction, and $\frac{dn}{dx}$ is the refractive index gradient along the probing direction. For the LPI experiment, the refraction angle θ can be estimated by assuming we are probing ~1mm long plasma at near critical density for 10μm radiation ($10^{19}cm^{-3}$). If the 532nm green laser pulse is used as the probe, $\boldsymbol{n_c}$ in Eq. (10) is equal to $4\times10^{21}cm^{-3}$. We assume the plasma density gradient is on the order of 10^{19} cm^{-4}, then based on the refraction angle equation, 2θ is calculated as 0.5° indicating it won't affect light collection significantly. Besides, as $\frac{\boldsymbol{n_p}}{\boldsymbol{n_c}}$ decreases, θ becomes even smaller which can further diminish the refraction. Thus, 532nm laser pulse is adequate for probing plasmas around $10^{19}cm^{-3}$. Obviously, using a visible beam makes alignment and transportation process rather straightforward.

In our MOPA laser system as shown in Figure 16, a fraction of the 1μm radiation, used for slicing of a short 10μm seed, can be directed into a KDP crystal to produce the second harmonic radiation (532nm) using a type I phase matching KDP crystal. This 532nm light is used to build the multiple-frame laser interferometry for LPI study. Energy conversion efficiency of the second harmonic generation (SHG) process is ~30%. Typically, a ~300μJ, 532nm pulse is produced from a fundamental 1μm light with a pulse duration ≤ 2ps as measured by a multi-shot auto correlator.

On the other hand, the 532nm probe and the 10μm seed pulse both originate from the same 1μm radiation. So, they are deterministically synchronized with each other. However, due to the sequential delays introduced by many round trips inside the CO_2 regenerative amplifier and three passes in the final amplifier (7.5m), it arrives at the interaction point (IP) of the LPI experiment approximately 592ns (178m) later than the 532nm probe. In order to resynchronize the pump and probe on the IP in picosecond accuracy, the probe needs to be delayed by ~592ns. For this purpose, an optical delay line was designed and built [35]. We use two optical tables, which are separated by 10m to mount the optical components. The probe pulse is reflected between the two tables 13 times and then guided to the IP. The total delay of the probe before reaching the IP is roughly ~592ns. Thus, the pump and probe can be resynchronized on the IP within 1ns using fast detectors and an oscilloscope. The throughput of this transport system is measured to be ~60% and as a result an 180μJ probe pulse synchronized to the CO_2 laser pulse within ± 1ns can be delivered to the target chamber.

In order to temporally resolve the laser-plasma interaction dynamics, the pulse length of the probe is required to be as short as the time scale of plasma evolution which is expected to be on the order of the ion sound velocity, $C_s = \sqrt{kT_e/M_i}$, where k is the Boltzmann constant, T_e is the electron temperature, and M_i is the ion mass. For an electron temperature of kT_e = 1MeV (estimated by ponderomotive heating scaling), C_s = 12.6 μm/ps. For the probe pulse with temporal duration of 1ps, the plasma density layer can move by ~12.6μm which can be clearly resolved by the multi-frame interferometry diagnostic system present later with spatial resolution ≤ 5μm .

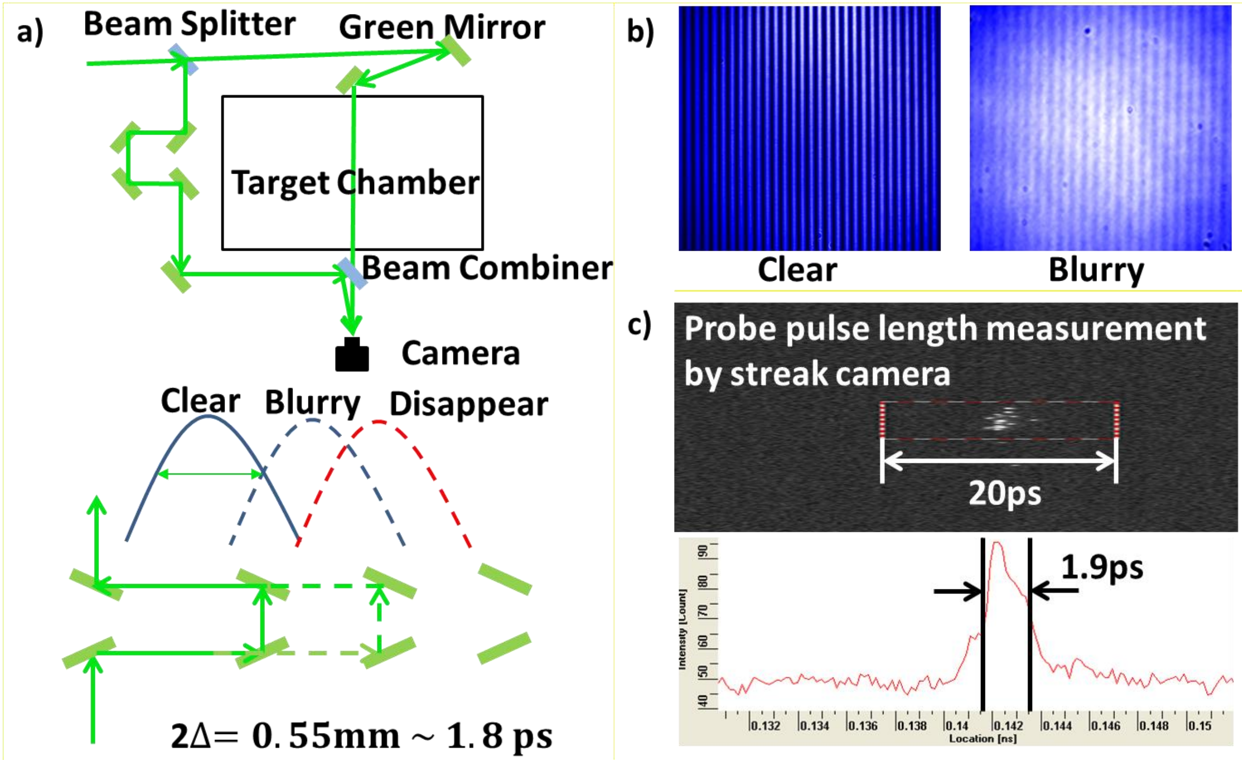

Figure 18: 532nm probe pulse length measurement (a) Schematic of the Mach Zehnder interferometer. The visibility of the interferometric fringes at different locations where the delay line parks is marked. (b) Comparison between the produced fringes with high and low visibility. (c) Probe pulse length measured directly by a streak camera with a ~1.5ps resolution.

A precise measurement of the probe pulse duration at the IP was accomplished by two methods, using interferometry or by sending the pulse directly to a streak camera. As shown in Figure 18 (a), the 532nm probe pulse enters into a classic Mach Zehnder (MZ) interferometer and produces the interference pattern on a CCD camera. The quality of the fringes produced can be described quantitatively using the visibility V , which, as first formulated by Michelson, is given by :

$$V = \frac{I_{max} - I_{min}}{I_{max} + I_{min}} \tag{11}$$

Where, $I_{max} = I_1 + I_2 + 2\sqrt{I_1 I_2}$ and $I_{min} = I_1 + I_2 - 2\sqrt{I_1 I_2}$. I_1 and I_2 are the intensity of the two interfered laser pulses. As we can see, when $I_1 = I_2$, the visibility V = 1, reaching the maximum and we can get the interference pattern with the highest contrast on the CCD camera. This fact points to a need to vary the green pulse energy smoothly in order to achieve visibility close to 1.

To measure the coherence length of the pulse, as shown in Figure 18(a), we can adjust the delay line to gradually increase the length of the reference arm to the point where the fringes disappear. Figure 18(b) shows the change of the fringe visibility corresponding to different positions where the delay stage parks. Here the fringe pattern first has high contrast but gradually becomes blurry when the length of the reference arm increases. The reason of degradation of the fringe visibility is due to a mismatch between the peaks of the pulse in a main arm and a reference arm which results in $I_1 \neq I_2$ and drop of V . A total of 4Δ = 1.1mm increment will make the fringe pattern fully disappear, in which case pulses of the main and reference arms are not overlapped at all. Based on this measurement, the FWHM of the probe pulse can be easily deduced as ~1.8ps. We also propagate the probe pulse into a streak camera where its pulse duration can measured directly. Figure 18(c) shows the result of streaking which confirms that our 532nm probe has the pulse duration close to ≤ 2ps.

4.3 Synchronization and Characterization of LPI Process

4.3.1 Cross-correlation Measurement

As mentioned earlier, the 10μm seed pulse for amplification in the CO_2 laser chain and the 2ps 532nm probe both originate from the same 1μm pulse of Nd: Glass CPA system, so they are deterministically synchronized with each other. However, due to a different propagation length, ~600ns relative delay is introduced by the time when the two pulses arrive at the IP. In order to diagnose the laser plasma interaction process using the probe pulse, a necessary step is to resynchronize the pump and the probe over the IP with picosecond time accuracy. To achieve this goal, a semiconductor switching technique is used for a cross-correlation measurement [31]. As shown in Figure 19, a piece of 800μm thick Si is mounted right above the gas jet at a 45° angle to both 10μm and 532nm beams. The CO_2 laser pulse is incident from the left to right and is focused by an 8.5" F/3 OAP down to a 60μm diameter spot on the Si plate. The 2ps, 532nm probe pulse is delivered into the target chamber and focused by an F=15cm lens down to an ~120μm diameter spot. The focal spot size of the probe is two times larger than the pump and through careful alignment, it can spatially cover the entire CO_2 laser beam. Behind the Si semiconductor, a mercury cadmium telluride (HCT) detector is installed to measure the energy of the transmitted CO_2 laser pulse.

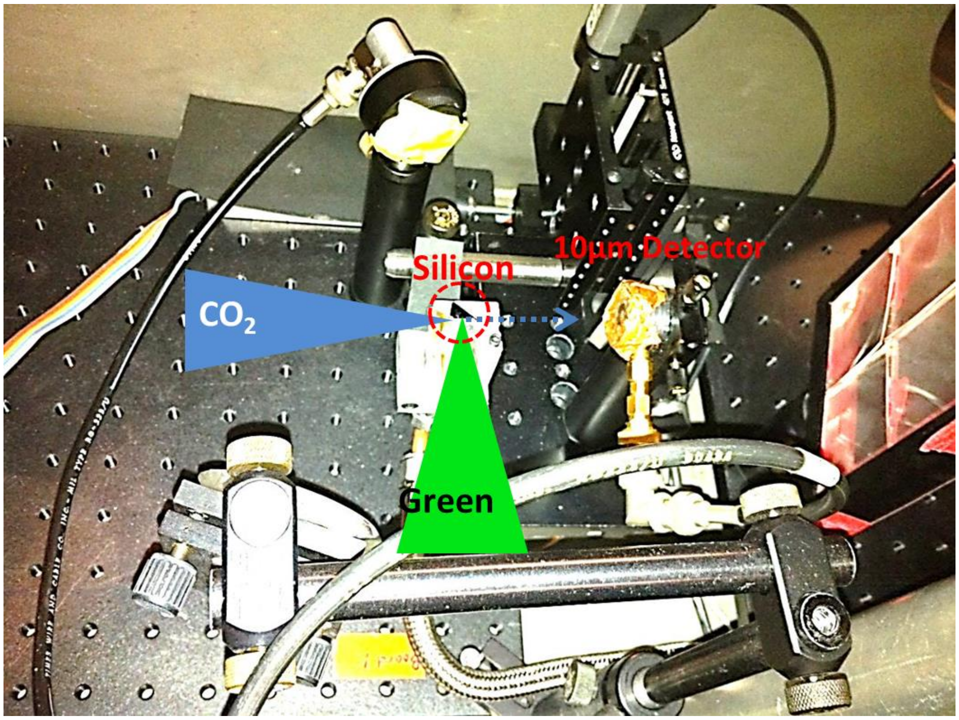

Figure 19: Picture of the experimental setup of the cross-correlation measurement.

The Si plate (~500μm thickness) will normally transmit a large fraction of the 10μm light but absorbs the 532nm light due to its bandgap being smaller than the photon energy. An electron-hole plasma layer can be formed on the surface of the Si plate after it absorbs the 532nm photons. When the surface plasma density increases to ~n_{cr} for the 10 μm radiation, the Si plate will act like a plasma mirror, being able to modulate the transmission/reflection of the 10μm light [31].

A typical scanning result of our cross-correlation measurement is shown below in Figure 20. The blue diamond data points show the normalized transmission signal of the 10μm light through the silicon plate as a function of the time delay of the probe. When the probe pulse arrives at the silicon plate later than the CO_2, the surface plasma produced on the semiconductor is too late and the 10µm light can propagate through unaffected. Otherwise, the 10µm light is screened by the near critical dense surface plasma created by the earlier probe. When the 532nm probe and the CO_2 pulse are crossing each other, we observe a transition of the high to low transmitted signal shown in the red fitting curve. The derivative of this fitting curve indicates an entire ~120ps long CO_2 macropulse envelope.

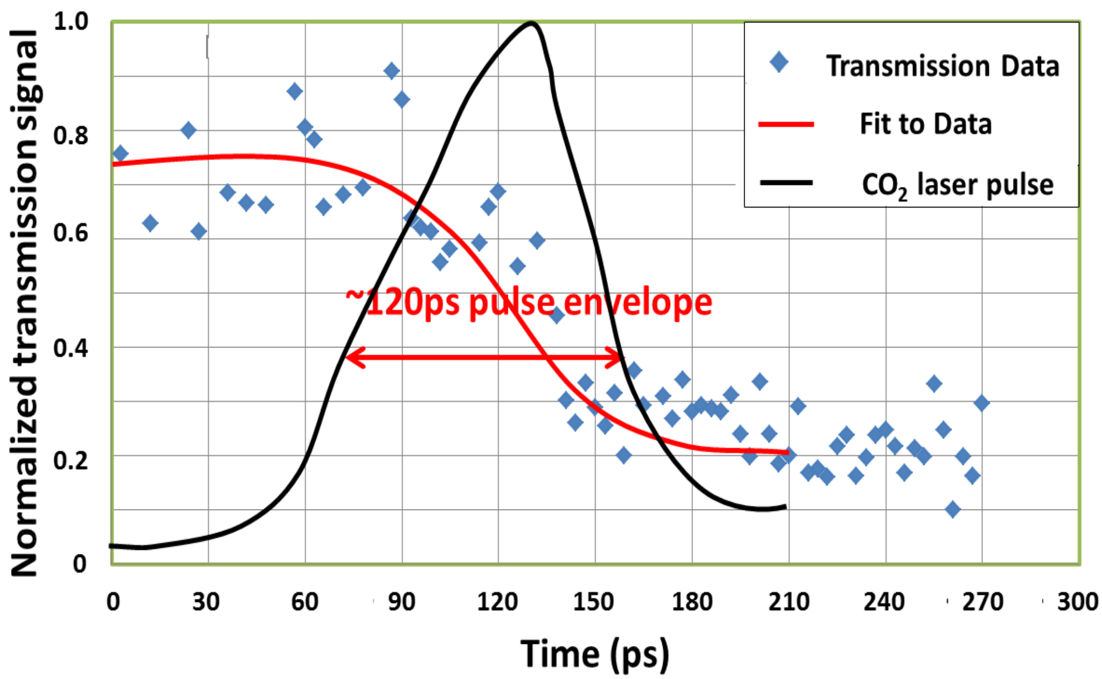

Figure 20: Cross-correlation measurement of the 2ps 532nm probe pulse with the 10µm pulse train. The blue diamond shows the normalized transmitted CO_2 signal in a function of time. Red solid line is a fitting curve to the blue diamonds. The black curve is the derivative of the fitting curve corresponding to the envelope of the CO_2 laser macropulse.

After mapping the entire CO_2 laser pulse envelope through the cross-correlation measurement, we adjust the position of the delay line such that the probe pulse coincides with the very peak of the scanned CO_2 laser macropulse envelope and is defined as time '0' for plasma probing. However, the entire cross-correlation measurement is completed with an unamplified CO_2 pulse. During the LPI experiment, when the final amplifier is on, an additional ~400ps delay is observed. This delays the entire CO_2 pulse train as shown in Figure 21. Contributions to this extra delay could come from various factors. For example, it is known that the resonant behavior of the refractive index results in increase of n in the inverted medium [37]. Also streaking of the unamplified pulse was realized with the use of an auxiliary mirror in front of the 8" salt window, which introduced another discrepancy in a time-of-flight for the 10μm pulse. Besides, during the run, a shot to shot variation of this extra delay is also observed which adds even more complexity for controlling the probe timing.

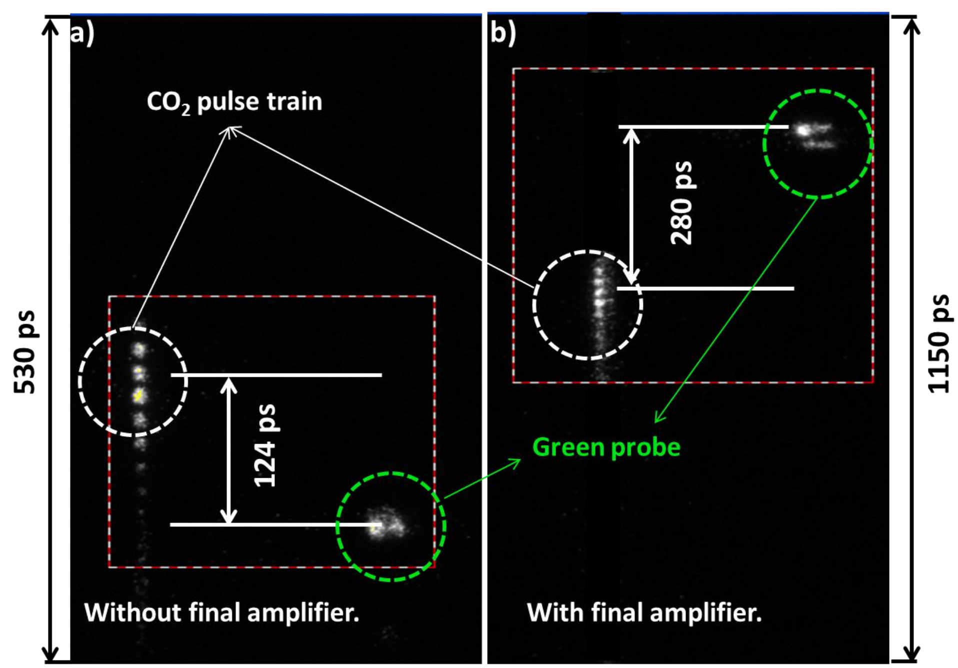

Figure 21: Streaking measurement of the CO_2 laser pulse train and the green probe pulse. Figure a) shows a 530ps streaking window. Without running the final amplifier, a relative delay of 124ps is observed between the CO_2 laser pulse train and the green probe. CO_2 laser pulse train

comes earlier than the green probe. Figure b) shows an 1150ps long streaking window. With the final amplifier on, the relative delay between the green probe and the CO_2 laser pulse train changes to 280ps with the green probe comes earlier. The entire CO_2 laser pulse train is pulled back by 404ps during the laser shot.

4.3.2 Laser Temporal Structure Measurement

To take into account this systematic time uncertainty and to control the probe timing properly during the experiment, the pump pulse and probe pulse are simultaneously sent into the streaking diagnostic system for a temporal structure measurement. Then the relative time delay change between them is: i) observed for each shot and ii) can be compensated by adjusting the delay line for the probe green pulse. The experimental setup of the streaking diagnostic is shown in Figure 22 below.

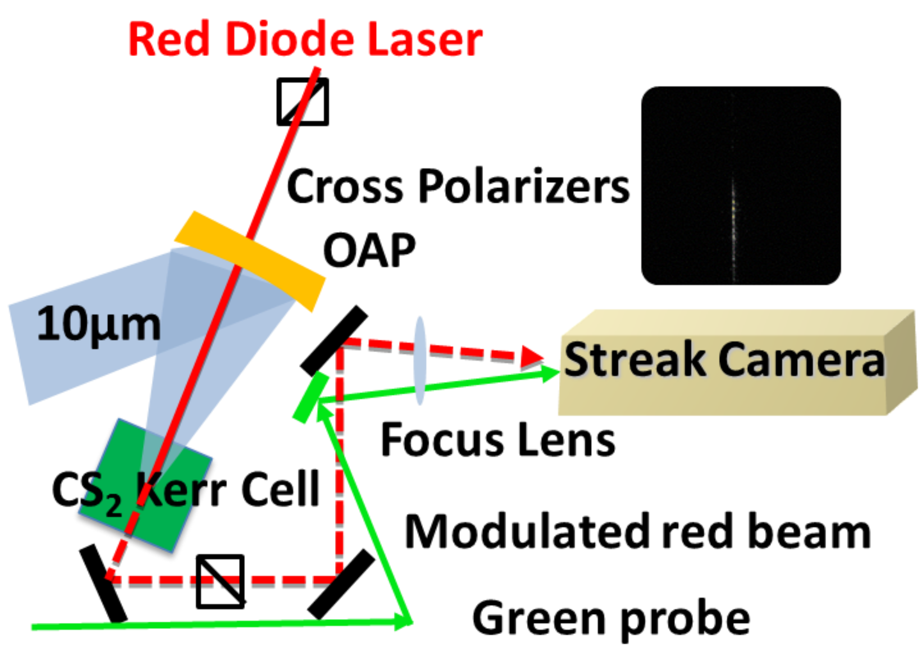

Figure 22: Schematic of the streaking diagnostics for the temporal delay measurement between the CO_2 laser macropulse and the 2ps, 532nm probe pulse.

A 4% back reflection of the incident CO_2 laser pulse from the salt window of the target chamber is directed and focused by a 5" OAP into a CS_2 cell. This intense 10μm pulse is used as a pump to produce a temporal birefringence in the CS_2 liquid through changing the nonlinear refractive index along its polarization direction (see Section 2.1 for more details). On the other side, a red diode laser pulse (658nm) is used as the probe for visualization. After passing through a polarizer, the red diode is focused through a hole at the center of the OAP and overlaps and propagates collinearly with the p-polarized high-power 10μm pump pulse through the CS_2 cell. Due to the nonlinear Kerr effect, the CS_2 medium acts like a transient phase retarder for the red diode controlled by a CO_2 laser pulse train. An analyzer is set up afterwards to transmit a portion of the diode with a rotated polarization, thus the filtered pulse signal will copy the entire temporal structure feature of the 10μm pulse. Then this frequency-up-converted pulse is sent into a streak camera with ~1.5 ps time resolution. The small insert of the streaking image in Figure 22 shows the typical modulated temporal structure of the CO_2 macropulse recorded in the experiment.

On the other side, a less than 2% leakage of the green probe from a 45^{o} reflection mirror is sent through a delay line and then directed to the streak camera. The amount of delay is carefully adjusted to put the probe pulse and the CO_2 laser macropulse on the same time window. It should be noted that the probe is still located in the middle of the CO_2 laser macropulse and this observed delay on the screen is artificial. Based on the streaking measurement, we know the probing timing within the CO_2 laser pulse train with an accuracy of 20ps.

The temporal structure of the amplified CO_2 laser pulse is an important parameter used to estimate the laser peak intensity. Figure 23 below shows a typical example of the temporal structure measurement of the amplified CO_2 laser pulse with the 532nm probe pulse on top.

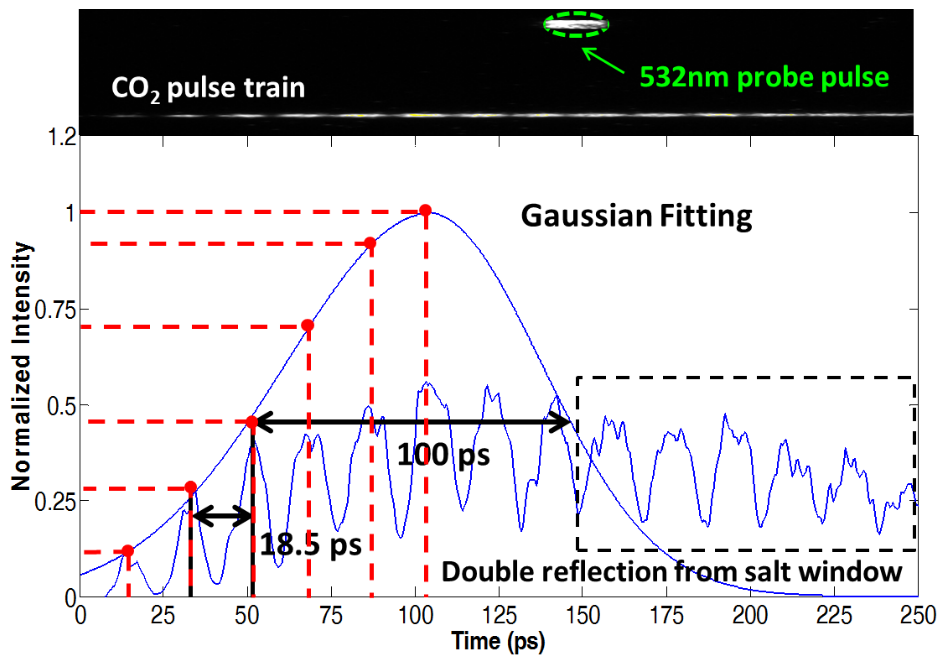

Figure 23: The top part of the figure shows the raw streaking data of 532nm probe and CO_2 laser pulse train in the same time window. The bottom part of the figure shows the lineout of temporal structure of the CO_2 laser pulse train and a Gaussian fitting curve in solid blue lines. The Gaussian fitting ignores the double reflection effect of the CO_2 laser from the salt window as well as the over rotational effect of the gated diode pulse. The measured FWHM of the CO_2 laser macropulse is ~100ps and the separation between micropulses is 18.5ps.

The top part of the figure shows a raw streaking image of the CO_2 laser pulse train. A simple sum column of the pixel counts reveals the temporal structure of the CO_2 laser macropulse consisting of a series of micropulses (see the blue lineout). The 3ps pulsewidth of each micropulse isn't resolved in this measurement due to the slow speed of the streak camera used for synchronization. Also small dynamic range of Kerr cell is responsible for low saturation limit of the signal as confirmed by nonphysical flattening of the signal and splitting of replicas of individual pulses discussed below.

For the streaking diagnostic, there are two limiting factors preventing us from attaining a direct, precise temporal structure measurement. The first is a 'double reflection effect', which is produced due to the reflection of the CO_2 laser pulse from the front and back surfaces of the NaCl window. Due to this effect, the temporal structure of the CO_2 laser macropulse is observed as having a double hump feature due to the overlapping of the two reflected laser pulses. The second issue is the 'over rotation effect' of the polarization of the red diode laser induced by the more intense CO_2 laser pulse. Due to this effect, a modulated pulse structure is resolved on the streak camera in vicinity of the most intense CO_2 laser micropulses. This is because the much more intense CO_2 laser pulse over-rotates the polarization of the red diode through the Kerr effect and more red photons are screened out by the analyzer before reaching the CCD camera thus lowers the count number eventually produced. Therefore a small dip is observed at the central peak area of the intense micropulse and produces the 'fork' structure. This effect induces an uncertainty for precisely resolving each individual micropulse--a key factor for the energy partition process.

To solve these problems and be able to assign energy to each individual micropulse, we use a Gaussian curve to fit the first CO_2 laser macropulse and neglect the second one induced by the double reflection effect. It is reasonable to assume the CO_2 laser macropulse has a Gaussian envelope and by fitting this Gaussian curve to the non-saturated micropulses as much as possible, we can use the modeled Gaussian function to mimic the CO_2 laser macropulse. As shown in the figure, the fitting Gaussian curve is superimposed on top of the streaking lineout using a solid blue line. For each individual micropulse with the over-rotation problem, its amplitude is replaced by the data point locating right above it on the Gaussian curve. Based on these assumptions, we can simplify our streaking data into Figure 24 shown below. The energy partition for each micropulse can be achieved based on their normalized amplitude shown along the y axis, which is used later for the laser intensity estimation. Note that careful measurements of temporal CO_2 laser pulse profile at the maximum of time resolution of the streak camera (not possible during the experimental runs due to the time jitter of SC) confirmed the above assumptions.

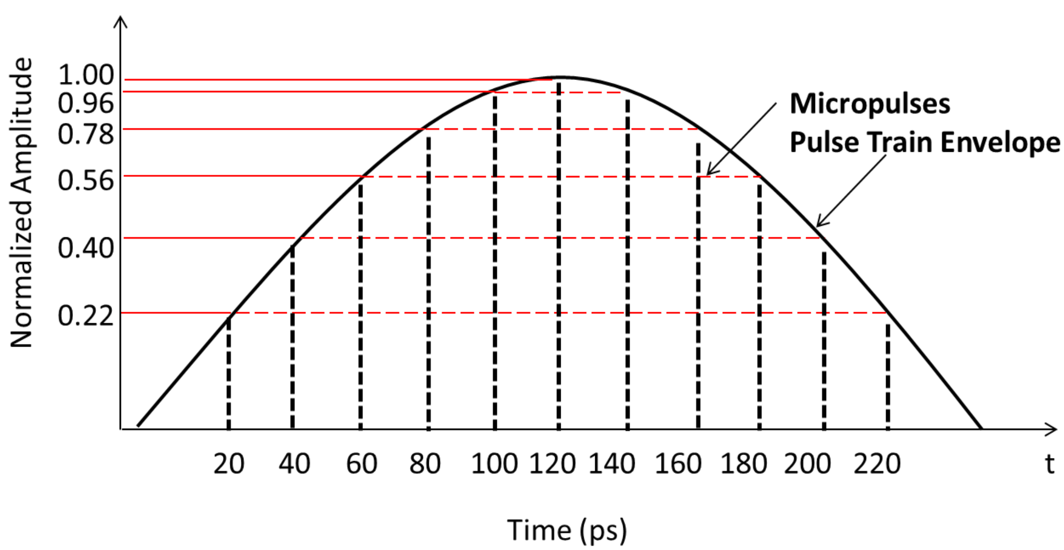

Figure 24: CO_2 laser pulse train distribution with normalized amplitude.

4.3.3 <u>10μm Laser Focal Spot Measurement</u>

To determine the laser pulse intensity the CO_2 laser focal spot size must be measured. To attain this parameter, an IR camera with a 5× magnification imaging system is set up to measure the spatial profile of the unamplified laser beam as a function of distance (Denoted as $\hat{z}$).

As shown in Figure 25, we measure the focal spot sizes of the CO_2 laser in two different focusing geometries F/3 and F/7.62 used in the LPI experiment. Due to the residual astigmatism of the beam, the observed spatial profile of the CO_2 laser beam is elliptical, thus both a horizontal (w_h) and vertical (w_v) radii are extracted for each $\hat{z}$ position and plotted as seen in the red and green traces, respectively. We observe that due to the stronger astigmatism effect of the laser beam for F/3 configuration, there is a much more significant difference between horizontal and vertical spot sizes than that for the F/7.62 focusing. For the z-scanning spot size measurement, there are also many other factors resulting in the non-diffraction limited focus of the laser beam. One of the most important effects is the small angle reflection from the mirrors and telescopes in a multi-pass final amplifier, which induces a divergence difference in different planes of the laser beam.

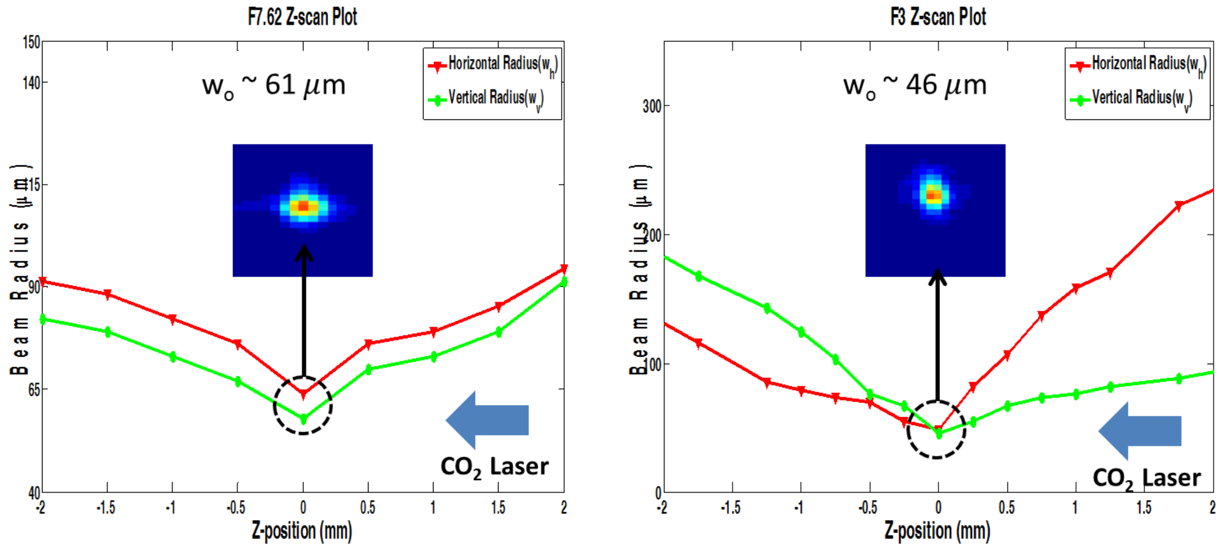

Figure 25: (a) 10μm laser beam radius along the laser axis ($\hat{z}$) for F/7.62 focusing geometry. (b) 10μm laser beam radius along the laser axis ($\hat{z}$) for F/3 focusing geometry.

Combining the measurement results of the CO_2 laser focal spot size and temporal structure with laser energy partition, we can estimate for a 45J laser shot (Typical laser shot energy delivered in the experiment to the gas jet) the laser peak intensity can reach $I = 5.0\times10^{15}$ W/cm^2 for F/7.62 scheme and $I = 2.87\times10^{16}$ W/cm^2 for F/3 scheme.

4.4 Four-Frame Mach-Zehnder Interferometry Diagnostic

4.4.1 <u>Generation of Four-Frame Interferograms Based on Laser Polarization</u>

Having a train of CO_2 laser pulses gives us a unique opportunity to observe the plasma density response to each individual micropulse by employing a multi-frame interferometry technique. In the past, we have employed a single frame interferometry to obtain the plasma density profile and also recorded some information about the plasma evolution by adjusting the probe time from one shot to the next. However, this is limited in its usefulness due to the fact that there is a shot-to-shot laser energy fluctuation. Ideally, only a single-shot diagnostic is capable to generate a clean set of data for plasmas pumped by a temporally modulated laser pulse. Therefore, we use the ~2ps, frequency-doubled (532nm) Nd: Glass laser pulse (Section 2.1) to build a four-frame Mach-Zehnder interferometer. As was discussed above, for the 532nm radiation, the 10^{19} cm^{-3} plasmas are underdense and transparent and can be analyzed by a regular CCD camera.

The total propagation length of the probe starting from the first reflective mirror of the transport system to the final IP is ~200 meters. Numerous mirrors, lenses and one additional quarter wave plate will depolarize the probe pulse and change it from linear to elliptical. As shown in Figure 26, this elliptical polarized probe pulse first enters into a Michelson Interferometer where a narrowband polarization cube (Glan-Thomson) splits the probe into P (60% energy) and S (40% energy) components. An arbitrary delay can be introduced for the S polarized component with respect to the P by using an optical delay line. A 20ps delay is set up between P and S with P arriving at the IP earlier. Then, both components follow the same beam path and propagate into a classical Mach-Zehnder (MZ) interferometer. In the MZ interferometer, the probe beam is additionally split into two channels with a fixed delay of 60ps by a beam splitter. An additional optical delay is introduced in channel1 to adjust the delay between the two channels. Channel2 (indicated by a dashed line) probes the plasma at a 2^o angle from a normal direction to the CO_2 laser axis. Each channel contains both P and S components separated by 20ps. Thus the entire comb of probe pulses covers an 80ps time window which is sufficient for probing the ~120ps long, 10μm laser macropulse. This comb of 2ps, 532nm probe pulses P1, S1, P2, S2 with the delays between them of 20ps, 40ps and 20ps respectively is then sent to the plasma for probing. A large 3” diameter field lens is mounted outside the target chamber, after the beam combiners to collect the probe light through the plasma. Also, the field lens is used to image the gas jet onto the cameras. Two Glan-Thompson polarization cubes are placed after the lens to separate and redirect the P and S components of the two channels into four independent CCD cameras to produce the four-frame interferograms at different probe times. The insert in Figure 26 at the left down corner shows a sketch of the CO_2 laser pulse train and a comb of 532nm probe pulses. For the CO_2 pulse train, each individual micropulse has pulse duration of 3ps and separates from each other by 18ps. Besides interferometry, a Schlieren diagnostic is also built up using the P2 component reflected off the beam combiner. A detail discussion about this diagnostic will be presented later.

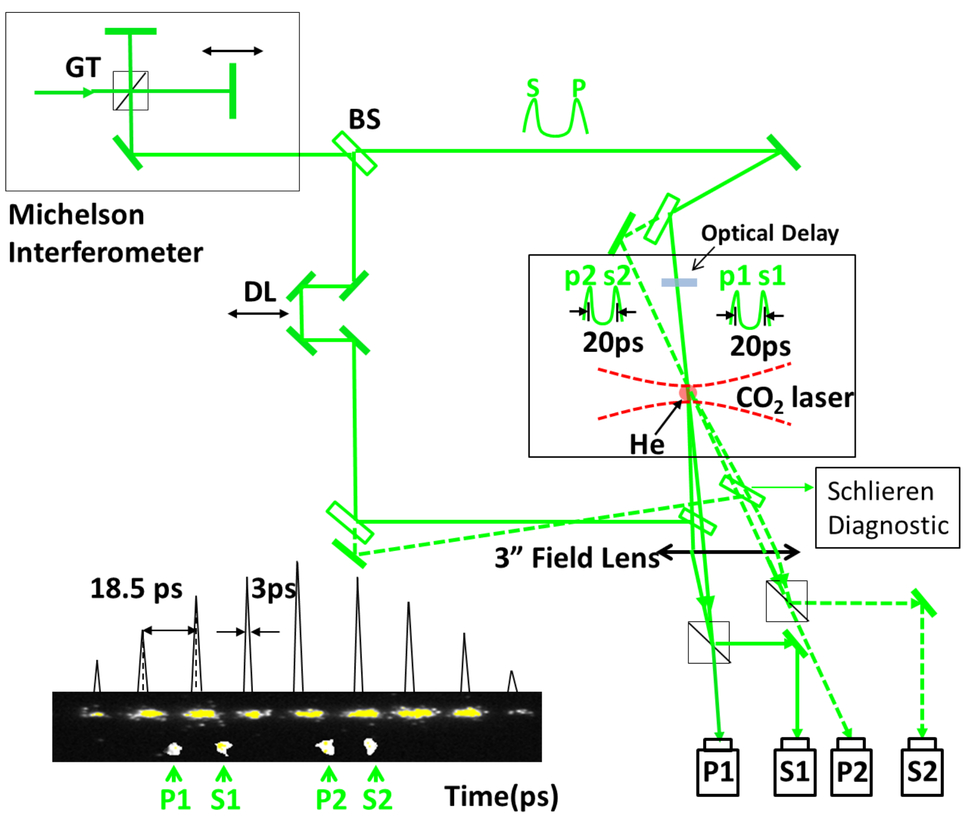

Figure 26: Schematic experimental set-up for four-frame picosecond interferometry. A streak of CO_2 laser pulse train (with a sketch of the intensity profiles of the micropulses is drawn on the top) and the four green-laser probe pulses used in experiments are shown below the schematic. GT is Glan-Thomson polarization cube. DL is an optical delay line. BS is a beam splitter.

4.4.2 Time Delay Setup of Each Probe Frame

As discussed, due to the modulated gain spectrum, the micropulses in the CO_2 laser pulse train are separated from each another by ~18ps. In order to study the dynamic evolution during the interaction between the near critical dense plasma and each individual micropulse, a precise delay control between each probe pulse is required in order to match with the unique temporal structure of the CO_2 laser pulse train. Figure 27 shows the experimental setup of how the time delay between the probe pulses was measured.

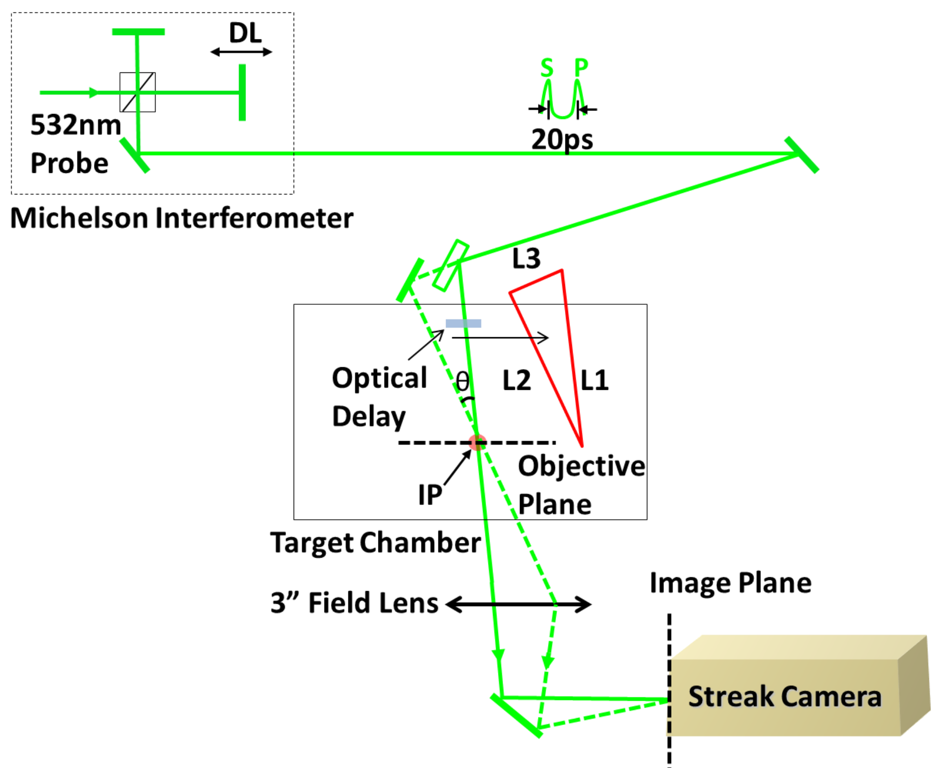

Figure 27: Schematic of the experimental set-up for temporal delay measurement of the probe pulses. DL is an optical delay line. IP is the interaction point where the CO_2 laser pulse is focused in the gas jet.

The purpose of this measurement is to adjust and setup the temporal delay between the probe pulses P1, S1, P2, S2 (the reference arm of the MZ interferometer is not shown). As the first step, let us ignore channel 2 (shown in the dashed green line) and adjust the delay between P1 and S1. As shown in the figure, a translation stage is used for one of the Michelson system mirrors. It was set such to provide a 20ps delay between p- and s- components of the beam. Outside the chamber, an F=35cm, 3” field lens is installed in the beam path to collect the P1 and S1 probes and image the gas jet onto the streaking camera. For this single lens system, the temporal delay between P1 and S1 measured by the streak camera is equal to the time delay between them when they arrive at the IP. After setting up the delay between P1 and S1 in channel, the second step is to adjust the delay between channel 1 and channel 2. For this purpose, we use a beam splitter and a mirror behind to produce channel 2, as shown in a dashed line. Since channel 2 is a replica of channel 1, the delay between P2 and S2 is the same as P1 and S1. As for the delay between the two channels, due to the spatial limitation between the beam splitter and the mirror, the time delay couldn’t be smaller than 60ps. As shown in the figure, this delay is introduced based on a length difference of the sides of a triangle (L3+L2)-L1, marked in the solid red line. Therefore, the delay between P1, S1, P2 and S2 are eventually set up as 20, 40, and 20ps. A temporal structure of four probes measured by the streak camera is shown in Figure 28. It confirms the separation between P1, S1, P2, and S2 as 20ps, 40ps, and 20ps. The slight curvature of the streaking line is resulted from the time of flight difference of the electron beam produced by the central and peripheral part of the laser in the varying high voltage tube of the streak camera.

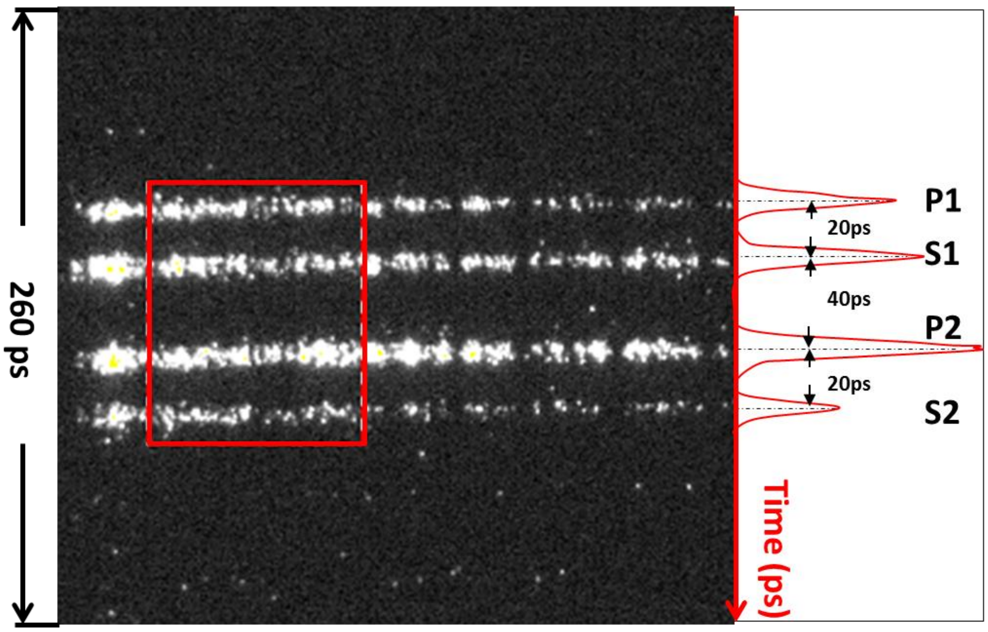

Figure 28: Temporal delay between P1, S1, P2, S2 measured by the streak camera with a resolution limit of ~1.5ps. The entire time window is 260ps. P1 is the leading probe pulse shown on the top of the frame.

To measure the plasma dynamic on a faster scale, the probe pulses of channel1 are delayed using a 10mm thick coated glass window, that is transparent for the 532nm radiation (as shown in Figure 26). This extra delay introduced to the system is 33ps. And by further adjusting the delay stage controlling the S component, we could eventually produce a comb of probe pulses separated with respect to each other by 7ps and covering ~20ps time window. This time delay is confirmed by the streak camera using the similar measuring method discussed above.

The goal of squeezing the four probes into a ~20ps time window is to study the dynamics of the plasmas during the interaction with each single CO_2 laser micropulse.

4.5 Dark Field Schlieren Diagnostic

Besides the four-frame Mach-Zehnder interferometry, a Schlieren diagnostic is also built into the experimental setup as shown in Figure 29. It uses an F/40 field lens to image the gas jet in a larger field of view than interferometer. Such zoom out imaging can give us better information about the whole plasma during the interaction as compared with the interferometric image. Additionally, during the interaction process, Schlieren image can help us observe whether the laser beam is strongly filamented or not in the underdense part of the gas jet target. Besides, the relative position of the laser pulse to the center of the gas jet is easily measured due to the large field of view. All the latter can be seen in Figure 30.

The Schlieren diagnostic works by imaging the refracted rays of the probe light when it propagates through the plasma. This is achieved by generating an intensity pattern on a CCD camera which images at the target by partially or entirely blocking the unperturbed light (dark-field) or the refracted light (light-field). The produced intensity pattern contains information of the plasma's refractive index gradients, which in turn are indicative of the density gradients in the plasma. (Eq.(10)).

In our LPI experiment, a comb of probe pulses P1, S1, P2, S2 are used to diagnose the plasmas. Since the main arm of the MZ interferometers propagates through the plasma, we can pick up any probe pulse from the main arm to produce a Schlieren image. During the experiment, we chose to use P2 because the probe time of P2 was typically close to the peak of the CO_2 laser pulse.

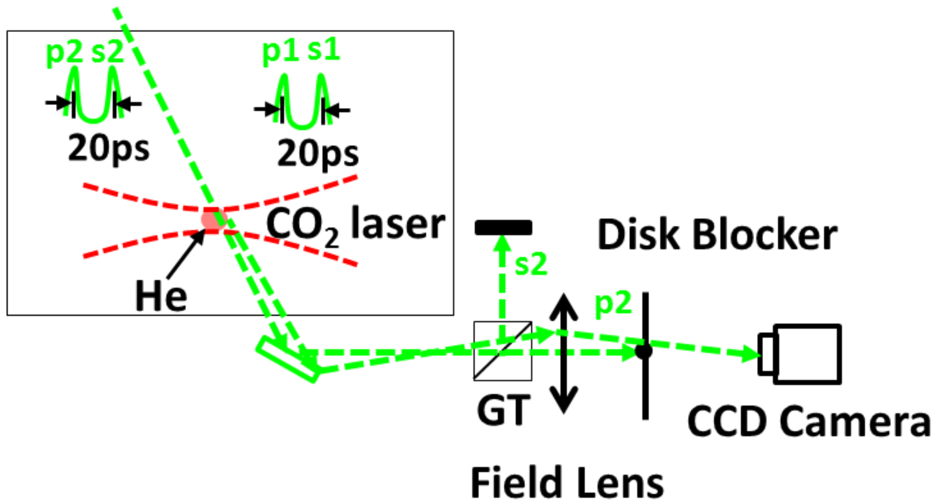

Figure 29: Schematic of the Schlieren diagnostic setup. The reflected rays off the beam combiner in channel 1 are completely blocked. A GT polarization cube is installed to filter out S2 component in channel 2. P2 component in channel 2 is used to generate the dark-field Schlieren image

As shown in Figure 29, P2 probe reflects off the back surface of the beam combiner after probing the plasma and then is focused down to a ~100µm diameter spot by an f= 20cm field lens. To generate the dark field Schlieren image, a 2" diameter glass disk with a 150µm diameter deposited Cr dot is installed in the focal plane of the field lens. With a careful alignment, the 150µm diameter Cr dot can completely block the P2 probe on the focal plane. If there is plasma in the beam path, which causes the probe beam to refract, the perturbed probe will follow a different trajectory, bypassing the 150µm diameter chrome blocker and arrive at the CCD camera.

The Schlieren image produced by these refracted rays in this way is indicative of the position of the strong density gradients in the plasma.

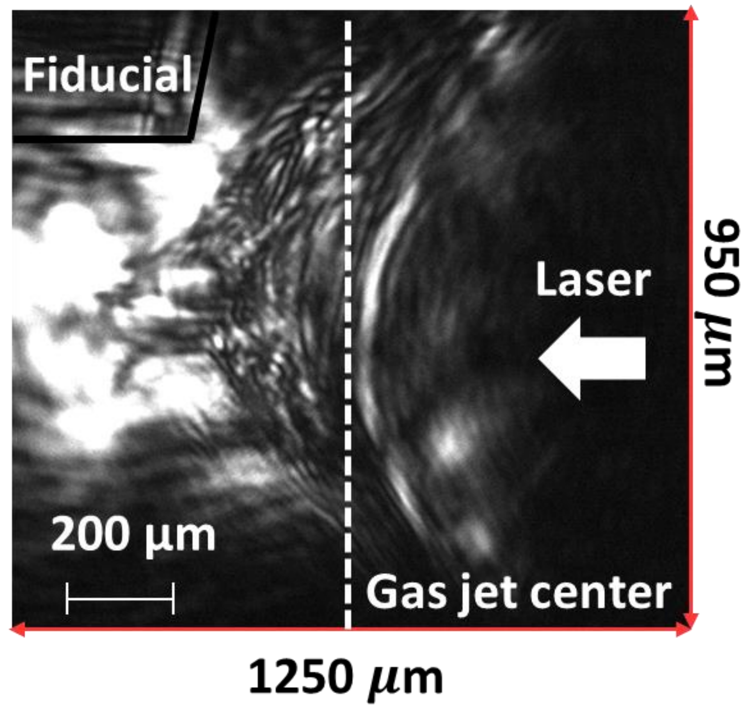

Figure 30: Schlieren image at a 45J laser shot in Helium gas plasma. The back pressure of the helium gas jet is 200psi. White dashed line indicates the center of the gas jet.

Another example of Schlieren image along with the interferogram is shown in Figure 31 (a) and (b) at a 60J laser shot. The back pressure of the helium gas jet is ~950psi. Plasma density inside the ion channel peaks at $1.1\times10^{18}cm^{-3}$, which is below the critical density of the 10μm laser. Plasma density measured on the wall is $\sim1.72\times10^{19}cm^{-3}$, slightly above the critical density.

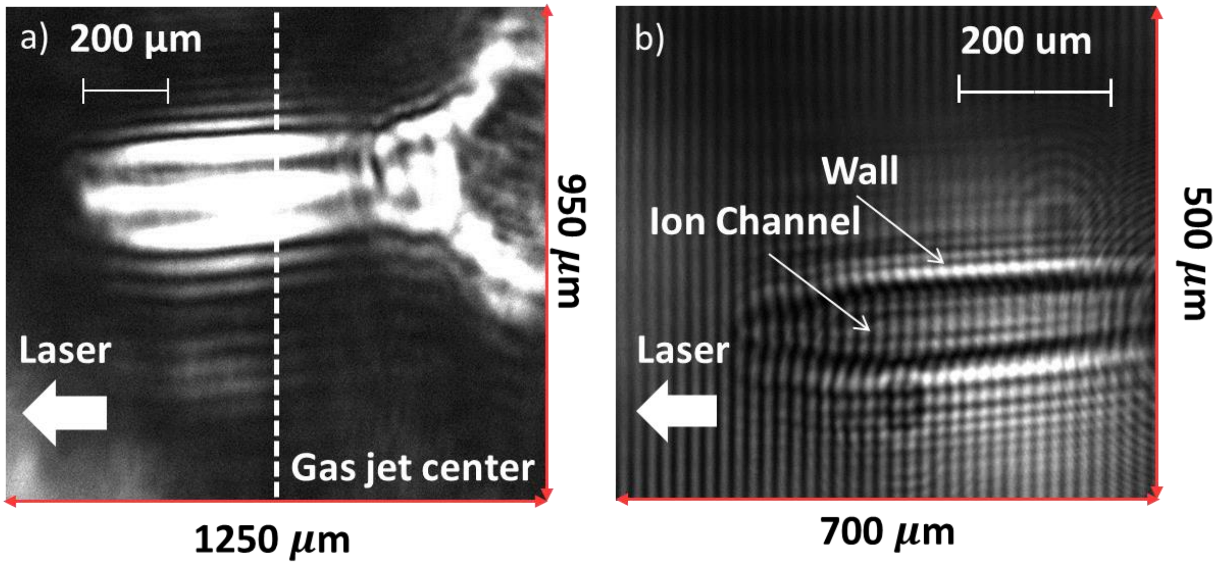

Figure 31: (a) shows a Schlieren image with a fiducial on upper left corner. (b) and (c) show Schlieren image and a corresponding interferogram at a 60J laser shot. The laser propagation direction is from right to the left. An ion channel with an overdense plasma wall (1.72×10^{19}cm^{-3}) is produced. Due to the limited field of view, the piled up plasma layer pushed by the laser radiation is missing in the image.

From the Schlieren image, we can see the formation of an ion channel. The estimated laser radiation power P is approximately equal to 350P_{cr} (P_{cr} is the critical power) [26]. This causes the laser to self-focus, which pushes the plasma electrons and ions out and produces a density channel. In this shot, a low divergence electron beam was observed on the phosphor screen. Also, we observed the piled up plasma layer pushed by the CO_2 laser in upstream location as shown in Figure 31(a). The center of the gas jet is set at the middle of the Schlieren image. The gas jet opening is 2mm. The entire field of view of the Schlieren image is ~1.3mm by ~1mm which is close to four times of the interferometry image, thus it provides us more information of where the laser is stopped and its relative position with respect to the gas jet center. In this particular shot, Schlieren image also shows a formed cavity driven by the laser radiation pressure behind the ion channel and its transverse cavity size. Also from the light refraction condition, a low plasma density area inside the cavity is clearly observed. On the other side, due to the limited field of view, all of this information is missing in the interferometry image.

4.6 Summary

In this chapter, we present the experimental setup for studying the dynamics of near critical density Helium gas plasma produced by a high power CO_2 laser pulse. The second harmonic generation (SHG) of a 1μm laser pulse using KDP crystal is used as a probe pulse. The pump pulse (10μm) and the probe pulse (532nm) are synchronized at the IP by employing a cross-correlation technique within 20ps accuracy. The laser focal spot size and its longitudinal variation is measured for two different focusing geometries.

The main diagnostic for the experiment is a four-frame laser interferometer that uses the 2ps, 532nm pulse as the probe. The temporal delay between each frame P1, S1, P2 and S2 is initialized as 20, 40, 20ps respectively to diagnose the plasma dynamics on the CO_2 laser macropulse timescale or 7ps for diagnosing the plasma dynamics between two laser micropulses that are 18ps apart. The temporal accuracy between the adjacent probe pulses is controlled within $\pm$ 1ps. Besides the interferometer, a Schlieren diagnostic with a larger field of view is set up to image the gas jet.

CHAPTER 5

5. Experimental Measurement Results and 2D OSIRIS Simulation

5.1 Introduction

Penetration of an intense laser beam into a dense plasma through the hole boring effect [19] and the self-induced transparency [38] is explored extensively in the context of laser interaction with an overdense plasma. Several experiments have been carried out to study the hole boring effect in a solid-density plasma by using the Doppler shift measurement [20]. However, these experiments have not simultaneously given both spatial and temporal evolution of this phenomenon. Besides, nonlinear effect such as self-phase modulation during the laser-plasma interaction process can affect the spectrum of the time integrated or time resolved backscattered light, which introduces extra uncertainty into the measurement result. A second technique that uses short pulse X-ray laser interferometry [39] to probe overdense plasma has revealed the formation of a laser bored cavity that has a strong modulated surface. However, time resolution in these measurements was also limited by the probe pulse duration and no systematic measurements of the hole boring velocity as a function of laser intensity were carried out. Recently, research group from University of Rochester also reported the observation of time evolution of the self-focused channel in the underdense plasma based on angular filter refractometry (AFR) technique [40]. Though, no direct measurement of hole boring velocity is reported due to the resolution limitation near the critical density plasma layer, the propagation velocity of the formed channel has been estimated and compared with the PCI simulation results.

The experimental results of the above diagnostic methods also show the complexity of laser plasma interaction resulting from the formation of a preplasma due to a limited contrast of the laser pulse.

As compared to solid targets and a near IR laser, using a gas target and a CO_2 laser to study hole boring process allows a direct visualization of the formation of laser cavity and its motion by using a visible-probe interferometer. In this chapter, we will present such direct measurements of the laser hole boring process by visualizing the time evolution of the density cavity using a four-frame, picosecond visible laser interferometry system.

5.2 Plasma Density Profile Measurement

We will begin with characterization of the plasma density profile. Interferometry can provide information of plasma density deduced from the phase change of the fringes after the probe propagates through the plasma. Analysis of interferograms is typically performed using a phase retrieval and Abel inversion computation program [41]. However, the success of extracting an accurate 2D plasma density profile depends on the homogeneity of the probe beam and the clarity of the interferogram including the visibility, continuity and sharpness of the fringes and the azimuthal symmetry of the plasma. For the P2 and S2 frames of a 45J laser shot (as shown in top two frames in Figure 32), there is a ~50μm thick dense plasma wall surrounding the cavity which causes the blurring of the fringes due to a strong refraction of the probe beams. Therefore, instead of using the phase retrieval and Abel inversion technique, a point-by-point manual analysis of the interferograms needs to be performed to extract the on-axis plasma density. Bottom two frames in Figure 32 show the on axis density profiles retrieved from the manual procedure. The CO_2 laser is incident from the right to the left. From the acquired interferogram, we can clearly see a parabolic region surrounded by a higher density plasma layer-- a characteristic curved cavity initiated by the radiation pressure of the laser pulse. This cavity is attached to the laser pulse in the direction of the laser but is now much larger than the extent of the laser pulse in the transverse direction. The significant bending of fringes in the narrow plasma layer indicates a high-density plasma area. The phase changes of the marked points (blue dots) on laser axis in the interferogram are measured by comparing a relative shift of the fringes with the background fringes (without plasma). One period here corresponds to a 2π phase shift. For the upstream region (towards laser), where the cavity is recorded, the transverse plasma density profile is modeled as a low-density area surrounded by two identical high-density plasma walls [35]. The phase change is the contribution of two walls and the cavity. For the downstream region, (away from laser), the transverse plasma density profile is modeled as a continuous Gaussian distribution centered on the laser axis. Based on the assumed transversely symmetric plasma profile, the plasma density of all the marked points can be calculated.

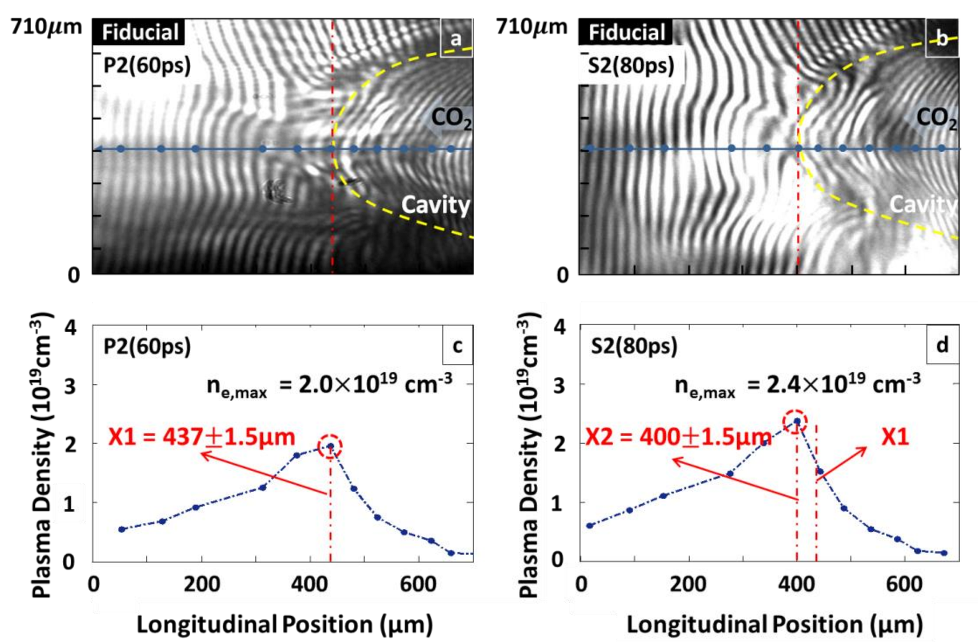

Figure 32: A point-to-point manual plasma density extraction on laser axis for two of the four interferograms taken for a 45J CO_2 laser shot. 80ps corresponds to the peak of the laser pulse train. Red dashed lines in a) and b) correspond to the peak plasma density. Yellow dashed line is the contour of the parabolic shaped cavity. Solid blue line with dots indicates the sampled positions for plasma density calculation. Dashed blue line with dots in c) and d) is the plasma density profile on laser axis. The peak a_o of the CO_2 laser pulse was ~1.4. The times notes are as indicated in Figure 24 w.r.t. the CO_2 laser pulse.

The results of the manually extracted plasma density profile are shown in c) and d). Comparison between these two shows that the peak plasma density is greater in the later interferogram (S2) indicating that one additional laser pulse has piled up even more plasma density from 2×10^{19} to 2.4×10^{19} cm^{-3} (2 to 2.4 n_{cr}) and the peak plasma density has been pushed forward by the laser radiation pressure by ~37μm during 20ps. On this timescale the gas jet neutral density does not vary within our accuracy of measurement. The density profile inside the cavity is steepened compared to the long plasma tail at downstream from the peak density. Though the laser could not penetrate the overcritical plasma layer, photoionization and collisional ionization by low energy electrons accelerated by laser can be responsible for a millimeter-scale exponentially falling plasma density profile formed on the back of the target. It should be noted that a good agreement between the measured values of plasma density and the initial density indicates the presence of singly ionized He in the overall volume of the plasma. This in turn suggests that the actual average peak value of $a_o \leq 1$, could be up to 40% smaller than that of the peak value determined from the measurement of the laser spot in vacuum.

As mentioned earlier, due to the blurring of the fringes, a point-to-point manual analysis is required for extracting the plasma density profile. However, there are several drawbacks existing by using this method, which will introduce errors and uncertainties for the data analysis. For instance, due to the resolution limit of the CCD cameras, the maximum phase shift we can clearly measure from the interferogram is 1/2π, and correspondingly this restricts the minimum measurable plasma density to greater than 2.8×10^{17} cm^{-3}. Also, due to laser prepulse on nanosecond time scale and laser filamentation effect and plasma expansion effects during interaction, a plasma cavity with much larger transverse size than the laser focus is produced. This introduces more complexities for the fringe counting process, which adds extra error. Besides, the assumption that the cavity is rotational symmetric around the laser axis is not accurate for a real plasma case. Thus, to understand such a complicated plasma density profile and testify the accuracy of the manual density analysis, a synthetic interferogram is generated using a Matlab program as shown in Figure 33.

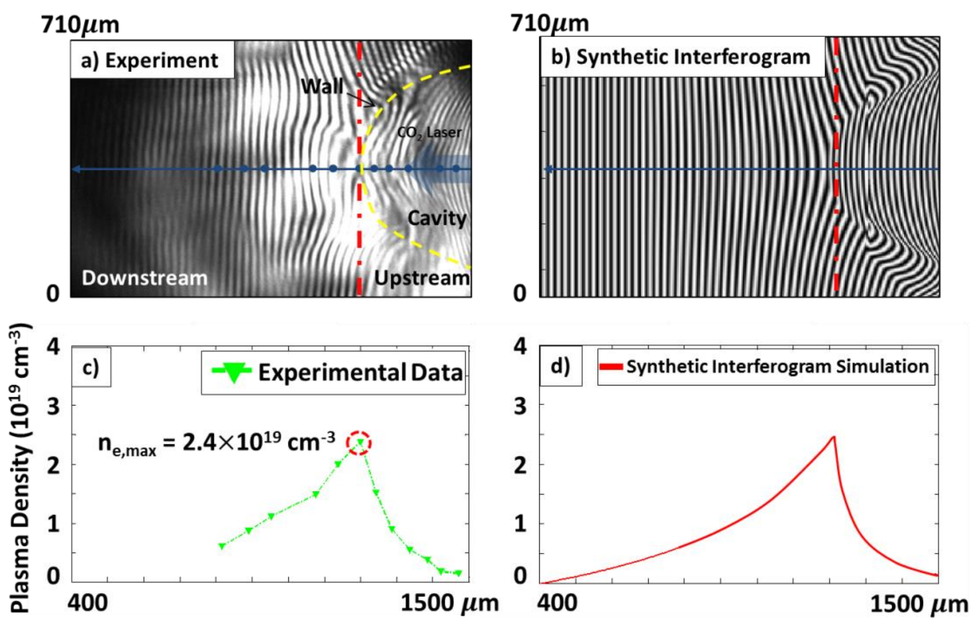

Figure 33: (a) An interferogram during the laser shot. (b) Synthetic interferogram. (c) Experimental plasma density profile on laser axis. (d) Simulated plasma density profile on laser axis.

A mathematic model is built to generate this synthetic interferogram in order to mimic the bending features of the interferometric fringes. A 3D, ~20μm thick parabolic shaped plasma wall is first created and a Gaussian distribution model is used to simulate the plasma density inside it. The plasma cavity is surrounded by the wall, and the density distribution inside is exponentially decreasing towards upstream starting from the inner shell of the wall. Outside the plasma wall downstream, the density distribution is also adopting a similar exponentially decreasing model to mimic the photoionization and collisional ionization. The fringe missing problem can be avoided in synthetic interferogram and the plasma density profile extracted out of it will be continuous. The synthetic interferogram is qualitatively similar to the actual interferogram up to the point where the laser is stopped by the plasma (i.e. the upstream region up to the peak plasma density). On the downstream side the curvatures of the fringes of the synthetic interferogram and the actual interferograms do not match and thus any on axis density fit is almost certainly fortuitous. However, on the upstream side, we can test the accuracy of the manually extracted plasma density profile using the synthetic interferogram. The plasma density profile on laser axis is plotted with a solid red line in Figure 33(d). And by adjusting the thickness of the plasma wall in the simulation, we can obtain a plasma density profile that is in a good agreement with the manually extracted one from the direct measurement. And both of the peak plasma densities of the S2 frame are equal to $2.4\times10^{19}cm^{-3}$.

5.3 Hole Boring Velocity Measurement

As was mentioned before, a high power laser pulse can steepen and push the critical density layer of plasma resulting in formation of a three dimensional cavity of a hole in plasma. In this section we report the first direct measurements of the laser hole boring velocity, V_h, in overdense plasmas using a four-frame picosecond green pulse interferometry. A train of CO_2 laser micropulses contained in a macropulse is used to create and push on a three dimensional cavity or a hole in an overdense helium gas jet plasma in the experiment. Using the pulse train has allowed us to measure the dependence of V_h on laser intensity and has elucidated the importance of plasma electron heating during the laser macropulse.

The CO_2 laser beam with an energy up to ~50J is focused down to a 1.4mm diameter He gas jet to give a maximum $I\lambda^2$ of 2×10^{18} $W\mu m^2/cm^2$ ($a_o<1.4$) for the most intense micropulse. A fiducial (a strip of ~200μm thick cooper foil) is placed slightly off the plane of the gas jet, which introduces a sharp edge located at the upper left corner in the camera image. Using the four-frame interferometry, we can measure the relative displacement between the overdense plasma layer and the edge of the fiducial. Combined with the information of the probe time of each frame, we can easily deduce the moving velocity of this overdense plasma layer. For each shot, P1, S1, P2, S2 frames generate four snap shots of plasma at 0ps, 20ps, 60ps and 80ps. One hole boring velocity can be measured between two adjacent frames. Thus, for each laser shot, we can deduce three hole boring velocities between P1-S1, S1-P2 and P2-S2. Each of them corresponds to a unique probe time within the CO_2 macropulse. Note that analysis of hole boring velocity by using frames from the same channel such as P1-S1, P2-S2 is rather straightforward. For S1-P2 measurement, a special procedure to take into account the parallax effect between probe beams needed to be adopted. Before the measurement, the distance between a fiducial and the center of the gas jet was determined for each channel. This allowed for generation of a correct value in measuring S1-P2's absolute positions.

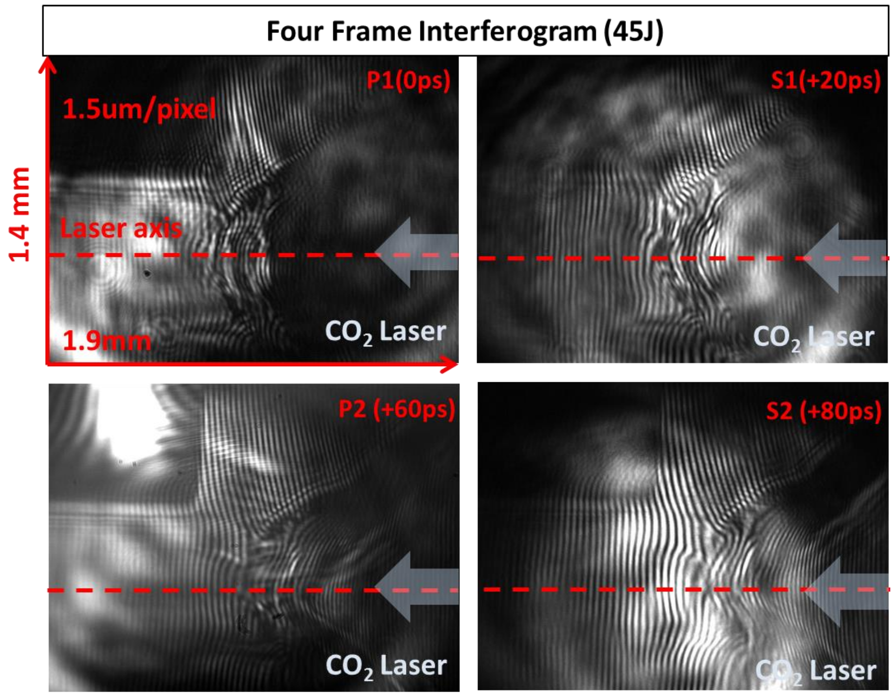

Figure 34: A typical four-frame laser interferometric image at a 45J laser shot. The field of view of the each probe window is 1.9mm × 1.4mm. The resolution of the CCD camera is 1.5µm/pixel. CO_2 laser propagates from right to left and the red dashed line shows the laser axis. Time delay between P1, S1, P2, S2 probes is 20, 40 and 20ps. The rectangular show is cast by the Cu fiducial.

Figure 34 shows a typical four-frame interferograms for a 45J laser shot. Each frame has a field of view of 1.9mm ×1.4mm with a camera resolution of 1.5µm/pixel. The CO_2 laser is propagating from right to the left and the red dashed line shows the laser axis. We can see the dark shadow formed by the fiducial located at the upper left corner in each frame due to the partially blocked main arm probe. The fiducial is positioned at downstream and doesn't affect the laser plasma interaction process. In order to get a sharp and clear image of the fiducial, the reference arm of the interferometry is blocked right after each laser shot to avoid the interference pattern and then a background image is recorded. The background image is used later to measure the relative distance between the overdense plasma layer and the fiducial.

We take P2 and S2 frames of this shot as an example to demonstrate how to measure the moving velocity of the overdense plasma layer. As shown in Figure 35, P2 and S2 frames have been cropped into two 710μm × 700μm images. P2 is probing 20ps earlier than S2 and based on the streaking data of the relative delay between the probe and the CO_2 laser pulse train, P2 is probing at the laser peak.

Here in the figure the 2D projection of a three-dimensional laser produced density cavity can be clearly seen in both P2 and S2 frames. The cavity shape is highlighted using yellow dashed lines by identifying features that are common in both frames. Outside of the cavity there is a high dense plasma layer with approximately 50μm thickness where some blurring of the fringes occurs due to a strong refraction of the probe beams in plasma. We define the velocity at which the on-axis position of this overdense plasma layer is moving as the hole boring velocity.

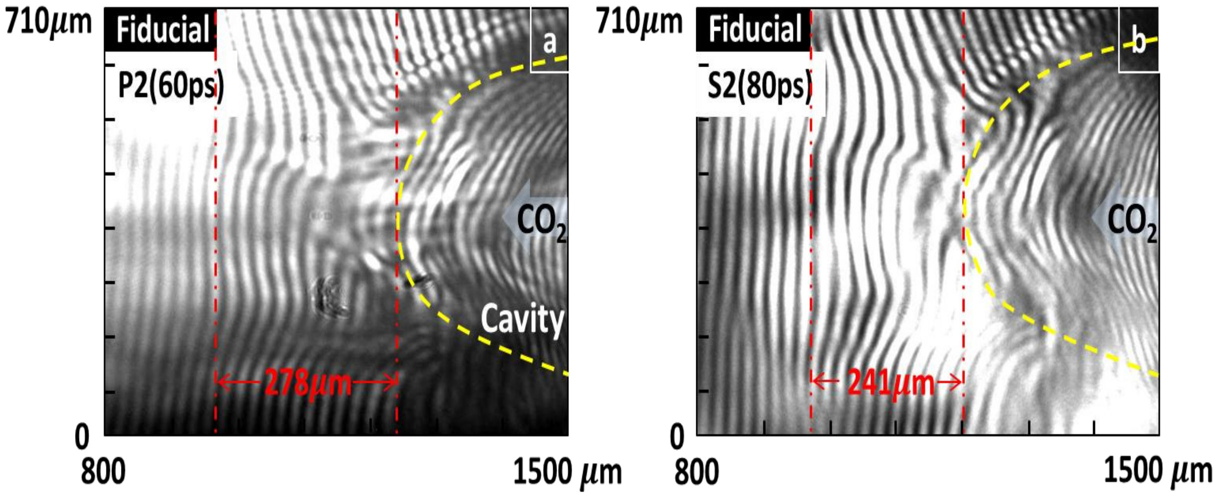

Figure 35: P2 (a) and S2 (b) frames of the four-frame interferograms taken for a 45J CO_2 laser shot. Each probe windows has a field of view of 700μm ×710μm. The light blue arrow shows the direction of the CO_2 laser beam. The dashed yellow line indicates the parabolic shaped cavity in plasma produced by the earlier laser micropulses. The two red dashed lines in each frame mark the position of the edge of fiducial and the front of the laser bored cavity. The distance between them is also labeled. P2 frame probes at 60ps and S2 frame probes at 80ps (20ps separation).

As shown in Figure 35(a) of the P2 frame, the distance between the overdense plasma layer and the edge of the fiducial is measured as 278μm. However, 20ps later, in b) of the S2 frame, this distance decreases down to 241μm. This result indicates a 37μm movement of this overdense plasma layer in 20ps. Thus the hole boring velocity is calculated as $V_h = 1.85\times 10^6$ m/s or 6.1×10^{-3}c. Moreover, the measurements of V_h along the laser axis have revealed that a region with a thickness of ~100μm (10λ) downstream outside the cavity travels with approximately the same velocity. We also measured the longitudinal component of V_h off the laser axis. It decreases slowly and reaches at $V_h = 3\times10^{-3}c$ on the edges of a 45° cone.

By varying the relative time delay between the probe beam and the CO_2 laser pulse, we scan over the entire 10.6μm pulse train using the fixed comb of green pulses (and even probe before/after it) and then extract the hole boring velocities at the corresponding probe time. Through these measurements, we first observe the hole boring as soon as when the laser intensity exceeds 10^{15}W/cm^2 which is the tunnel ionization threshold for He^{1+}. At this threshold intensity the tunnel ionized plasma is expected to be fairly cold [42] whereas the peak a_o of the laser pulse is already 0.3. In other words the radiation pressure to the thermal pressure of the plasma is already large.

As seen in Figure 36(a)- this data was taken at a peak a_o of 1.4- the critical plasma layer is first pushed by the laser at an increasing speed then begins to slow down after passing the peak of the macropulse and then stops moving altogether at t = 60ps despite the laser still exerting radiation pressure on the plasma. And in Figure 36(b), the maximum hole boring velocity is measured to be $6.1\times10^{-3}c$ and $3.4\times10^{-3}c$ for the high and low intensity cases, respectively. Note that the values of V_h measured here directly are in a good agreement with those inferred from Doppler-shift measurements [20]. We observe a striking difference in variation of V_h during the rising and falling edges of the CO_2 laser pulse train. The hole boring velocity drops faster during the falling edge of the macropulse and the rate at which this drop occurs depends upon the peak a_o delivered to the plasma. We also explored dynamics of the laser hole boring between two 3ps CO_2 laser pulses during the risetime by adjusting the timing between the four probes to be ~7ps. These measurements revealed that within the measured accuracy, the overcritical plasma layer continued to move between the micropulses at a near constant velocity. This suggests that at least during the risetime of the macropulse the laser radiation pressure clearly dominates over the plasma thermal pressure to such an extent that once the plasma ions are set into motion in the forward direction they continue to move due to inertia.

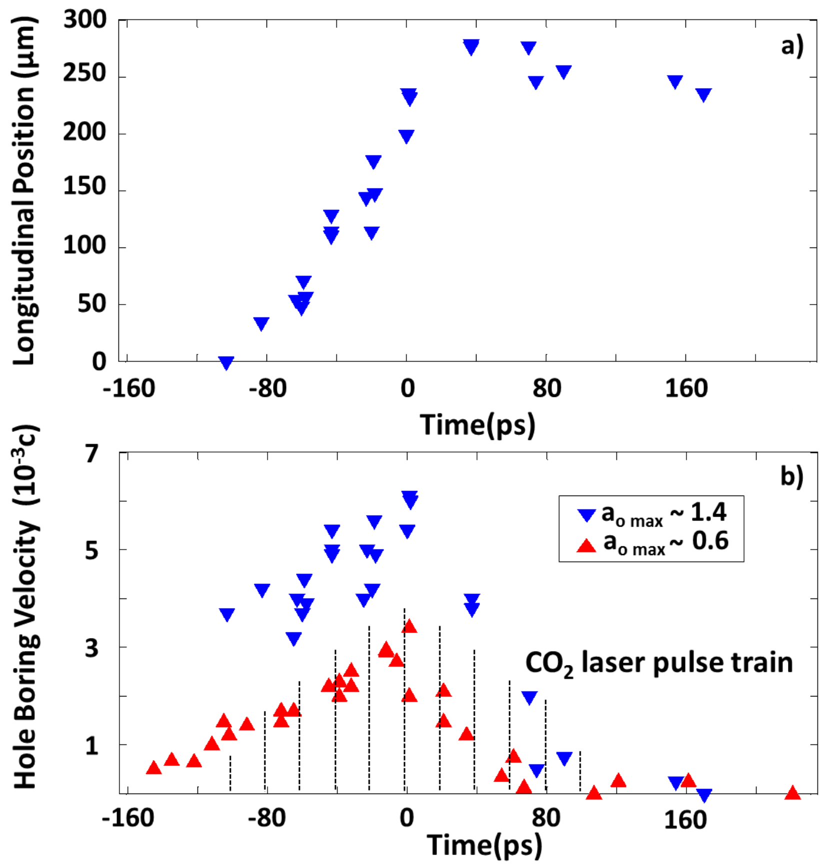

Figure 36: Time dependence of the laser hole boring. a) Experimentally measured longitudinal position of the peak density layer as a function of time (blue triangles) for a peak neutral density of $2\times10^{19}cm^{-3}$. b) Experimentally measured hole boring velocity as a function of time recorded during ~260 ps CO_2 laser-plasma interaction for two different values of peak ao indicated by blue and red triangles, respectively. The accuracy of velocity measurements in this method is 10% limited by spatial resolution and error is not shown because it is smaller than the symbol's size.

Figure 37 below depicts the measured V_h as a function of $I\lambda^2$. Also plotted is a curve for V_h from Eq. (12) first hypothesized by Wilks [19].

$$\frac{v_{hb}}{c} = [\frac{n_c}{2n_{pe}} \frac{Zm}{M} \frac{I\lambda^2}{1.37\times10^{18}}]^{1/2} \tag{12}$$

Where n_c is plasma critical density, n_{pe} is the plasma density, m is the electron mass, M is the ion mass, Z is the charge state, $I\lambda^2$ is the laser irradiance in unit of $W/cm^2\mu m^2$.

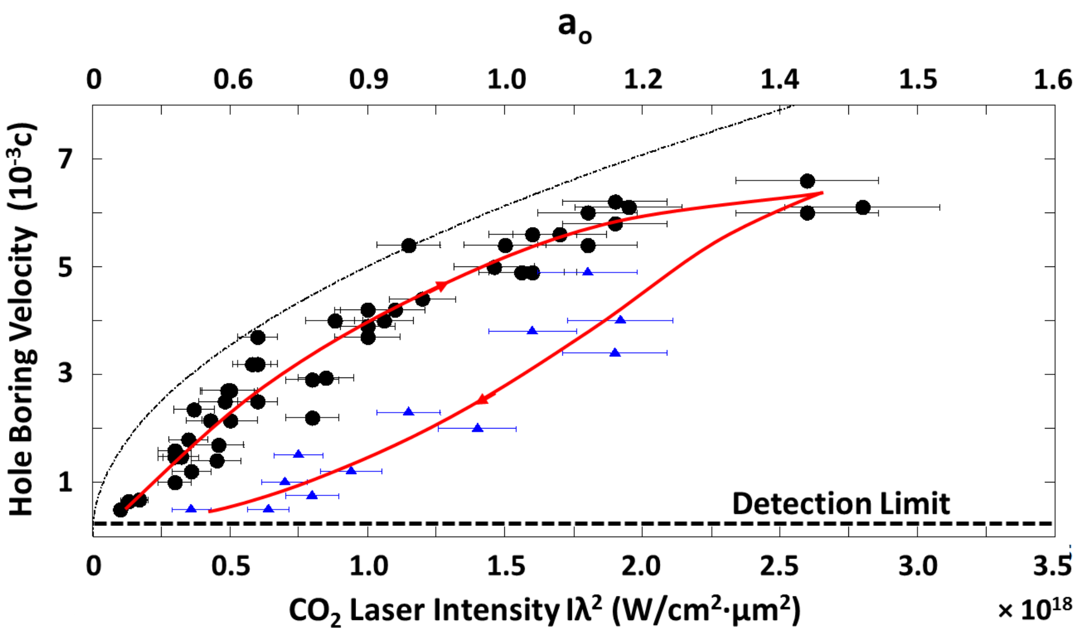

Figure 37: Intensity dependence of the hole boring velocity. V_h as a function of $I\lambda^2$ for a rising edge (black dots) and falling edge (blue triangles) of the pulse train. Red dashed lines are polynomial fit to the experimental data with arrows indicating direction of change of laser intensity for rising and falling edges of the CO_2 laser envelope. The solid black line is a calculated velocity for $n_e = 2n_{cr}$ using predication of Eq. (12) for the cold and totally reflective plasma. The limit of detection of V_h was defined by a pixel size of the CCD camera to be ~3×10-

^{4}c. The $I\lambda^2$ values used here are the vacuum values. The actual average values reaching the peak density of the plasma may be up to 40% smaller due to plasma induced refraction and dynamics change of position of the laser focus during the macropulse.

The first thing to note is that as the laser intensity is increased during the risetime of the laser macropulse (black circles), V_h increases albeit somewhat slowly than the expected $I^{0.5}$ scaling for a cold plasma and eventually begins to saturate at the highest values of a_o. An important clue as to the dominant physics that determines this scaling comes from the more rapid decrease of V_h seen during the falling edge of the laser macropulse (blue triangles in Figure 37). This hysteresis type behavior is more pronounced at higher laser energy and points to the role of P_{th} working to reduce the efficacy of hole boring. Intensity scaling of V_h with an exponent smaller than 0.5 has been also reported in the Doppler-shift measurements using a 1μm laser and this scaling is attributed to partial absorption of the radiation at the critical surface. This may also be true here but there are other complicating factors that increase (e.g. filamentation of the micropulses) and decrease (underdense laser-plasma parametric instabilities [23]) the net laser intensity reaching the critical density layer. Also the electron temperature will depend on the absorption mechanisms which in this intensity range make a transition from resonance absorption (a_o<1) to J×B heating (a_o >1) [43, 44].

5.4 2D PIC Simulation Results

In order to elucidate the complex physics of laser-plasma interaction that affects the laser-hole boring when it is driven by a train of intense pulses, we have performed 2D simulations with the PIC code OSIRIS [27]. The simulations use a box size of 1.5×1 mm^2, resolved with 6144 × 4096 cells and 16 particles per cell per species. We model the interaction of a train of nine laser pulses with a_0 = 0.52, 0.7, 0.85, 0.95, 1.0, 0.95, 0.85, 0.7, 0.52 and individual pulse duration of 3 ps, pulse separation of 18 ps, and transverse spot size of 84 μm (FHWM), closely following the experimental conditions. The laser interacts with a He gas with a triangular density profile with 0.5 mm rise and 0.5 mm fall and peak density of $2\times10^{19}cm^{-3}$. The plasma formation by field-ionization of the gas is self-consistently simulated using the ADK tunnel ionization model [45]. We note that collisional ionization, associated with the interaction of low energy particles with neutral atoms, is not taken into account. In the experiment collisional ionization is thought to produce a partially ionized plasma throughout the gas but this does not significantly change the laser hole boring on the front side, which occurs for $I\lambda^2>10^{17}$ $W\mu m^2/cm^2$, the field ionization threshold of He and produces a fully ionized He^{1+} plasma up to the critical density.

The first micropulse with a_0=0.5 ionizes helium via tunnel ionization up to the critical density creating a He^+ plasma. Further ionization of the low-density gas surrounding the interaction region is mediated by the currents associated with energetic electrons that are heated by the laser. The train of laser pulses then significantly modifies the plasma profile during its interaction, leading to density steepening near the critical surface, as shown in Figure 38(a) for a peak intensity (t=0). The plasma density here peaks at 1.6 n_{cr}. The lasers strongly filament between 0.5–1.0 n_{cr}, but most of their energy still reaches the critical density region, pushing it due to the radiation pressure (Figure 38(b)). Simulations confirm that the peak of the density profile corresponds to the position and the density where each micropulse is stopped and that the critical density layer continuously moves in between the micropulses as observed in the experiment (Figure 38 (c) and (d)). The maximum hole boring velocity $6x10^{-3}c$, is in a good agreement with the experimental results and the theoretical value $v_h = 6.5x10^{-3}$ from Eq. (12). In Figure 38 (c) we show that the longitudinal position of the peak plasma density agrees well for theory (red circles) and simulation (dashed curve). The evolution of the position of peak density confirms that hole boring is greater during the rising edge of the pulse train, as observed experimentally in Figure 36 and Figure 37. Electron temperatures in Eq. (12) were taken from simulations (see Figure 38 (c)) in which the bulk plasma electrons have been heated by the laser to ~140 keV at t = 0 and continue to reflux within the plasma cooling slowly [46, 47]. Theory gives a criterion for the laser to be able to push the critical surface $a_o > 2\sqrt{\frac{n_e}{n_{cr}}T_e[MeV]}$. For T_e = 140 keV, this threshold occurs at $a_0 \geq 0.75$ which is consistant with the observed termination of laser-hole boring at $a_0 \sim 0.7$ for a falling edge of the macropulse in Figure 37.

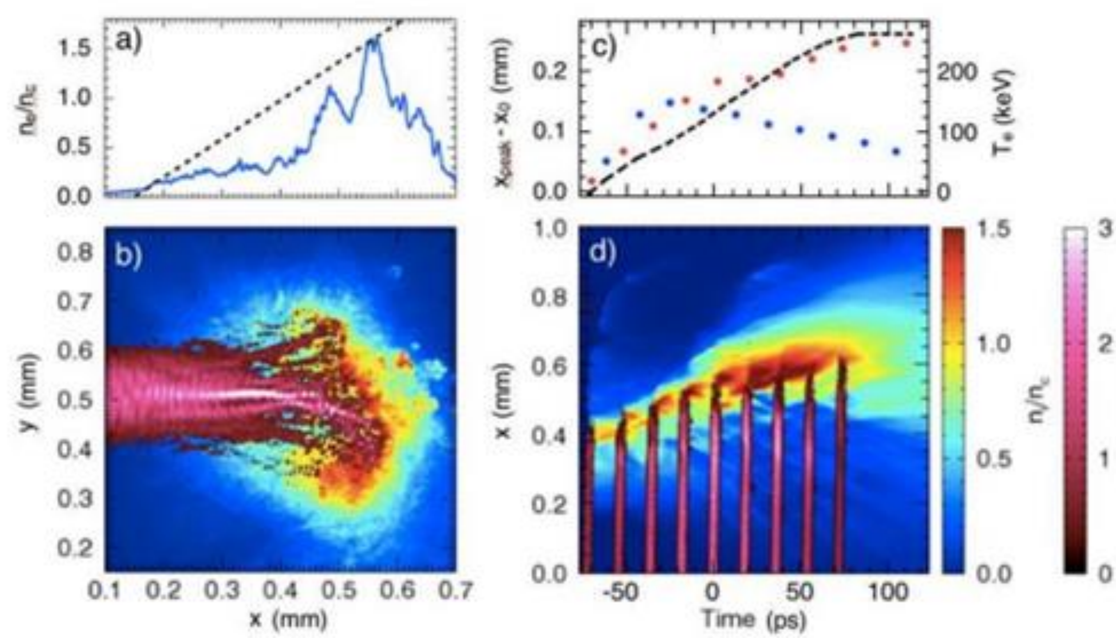

Figure 38: OSIRIS simulation of the interaction of a train of nine CO_2 laser pulses with a_0 = 0.52, 0.7, 0.85, 0.95, 1.0, 0.95, 0.85, 0.7, 0.52 with an individual pulse duration of 3 ps, pulse

separation of 18 ps, and transverse spot size of 84μm (FHWM), with a He gas having a peak density of 2×10^{19} cm^{-3}. A) On-axis plasma density profile at t=0. The black dashed line shows initial gas profile. B) 2D laser and plasma density profiles at peak laser intensity or t=0 ps. c) Temporal evolution of the position of peak plasma density, X_{peak}-X_0 from simulations (red marks) and from solving Eq. (5.1.1) (dashed line) for the plasma profiles, electron temperature and a_0 obtained in the simulation. Time dependence of T_e from simulations is shown by blue dots. d) Space-time diagram of the evolution of the laser field and plasma density on axis.

The good agreement between experimental measurements, theoretical predictions, and simulations has revealed spatio-temporal dynamics of the hole boring process. V_h first increases steadily during the risetime of the macropulse, where $P_L > P_{th}$, but the hole boring efficacy is strongly reduced during the falling edge of the macropulse because the plasma electrons once heated cool slowly causing more rapid fall of V_h and observed hysteresis. Finally our work suggests that the intentional use of several laser pulses rather than a single laser pulse [48] may lead to an efficient hole boring especially if a pulse train with an increasing laser intensity is used.

5.5 Helium Ion Acceleration Result

Laser-driven ion acceleration (LDIA) is capable of producing accelerated ion beams which have a short duration, an ultra-low emittance [49], and different charge states. This versatility has caused a lot of interest in the scientific community because of the potential application of such ion beams to fast ignition in inertial confinement fusion, ion beam cancer therapy, and for probing electric field structures in dense plasmas [50].

In the first LDIA experiment carried out at the Neptune Laboratory, we have demonstrated ~20MeV proton beams with a narrow energy spread of about $<$ 10% and low-emittance accelerated by laser-driven collisionless shocks [51]. Motivated by this encouraging result, we continued the LDIA experiments with the helium gas target to study if the similar accelerating mechanisms can be applied for light ion acceleration.

Helium ion acceleration was studied using experimental setup shown in Figure 17. A stack of CR-39 detectors is arranged on the laser axis with 15cm away from the gas jet. The detectors are tilted with ~4^{o} angle from the laser incident direction to avoid a back reflection. Comparative analysis of different ion detectors is presented in Appendix A.1.

A stack of CR-39 detectors allowed us to measure the energy spectrum of accelerated ions. The spectrum can be deconvolved based on the nonlinear loss of the particles' kinetic energy during the propagation process through the dielectric materials [52]. The primary loss of the energy as an ion propagates through the detector is due to the inelastic collisional process with the atomic electrons of the dielectric materials. The lost energy could result in ionization or excitation of electrons into the higher energy states. Based on quantum mechanics theory, this process can be described by the Bethe and Block formulism in energy lost per unit penetration length. Details of the Bethe and Block formula can be found in Appendix A.2.

Figure 39 shows an iterative plot of energy deposition of He^{1+} ions in CR-39 detector based on Bethe and Block formula.

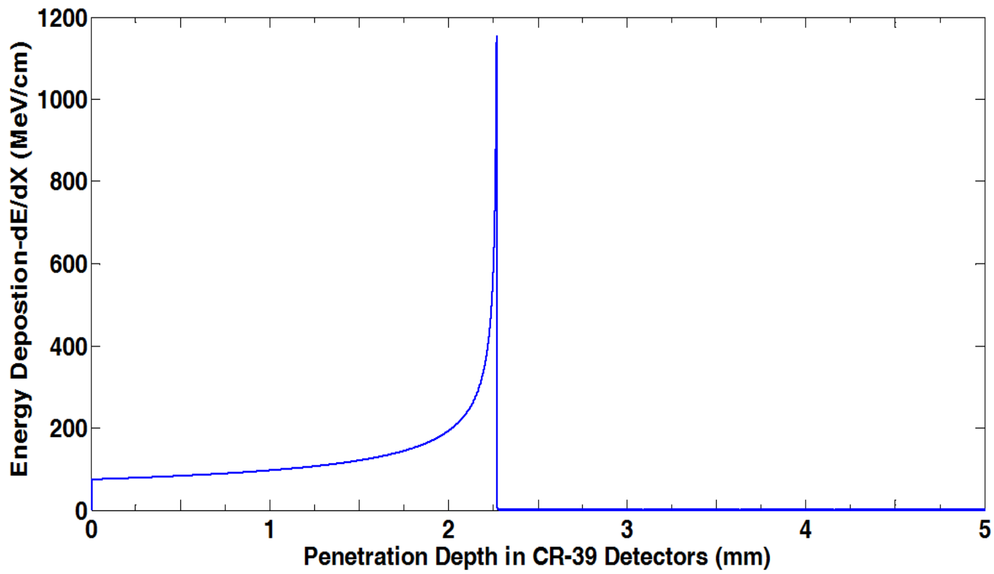

Figure 39: Energy deposition of single He^{1+} ion with an initial energy of 30 MeV propagating through the CR-39 material.

Figure 40 shows a plot of energy deposition v.s. penetration depth in CR-39 detectors of He^{1+} ions. The range of the initial kinetic energy of the ions is from 0~42MeV with a 1MeV step. Arrangement of the CR-39 detectors in the experiment and the energy range covered by each single CR-39 are also superimposed on top of the plot. CR-39 detectors also have two different thicknesses, 300µm and 1mm. Details of the configuration of the detector stack and specific dimensions are shown in Appendix B.1.

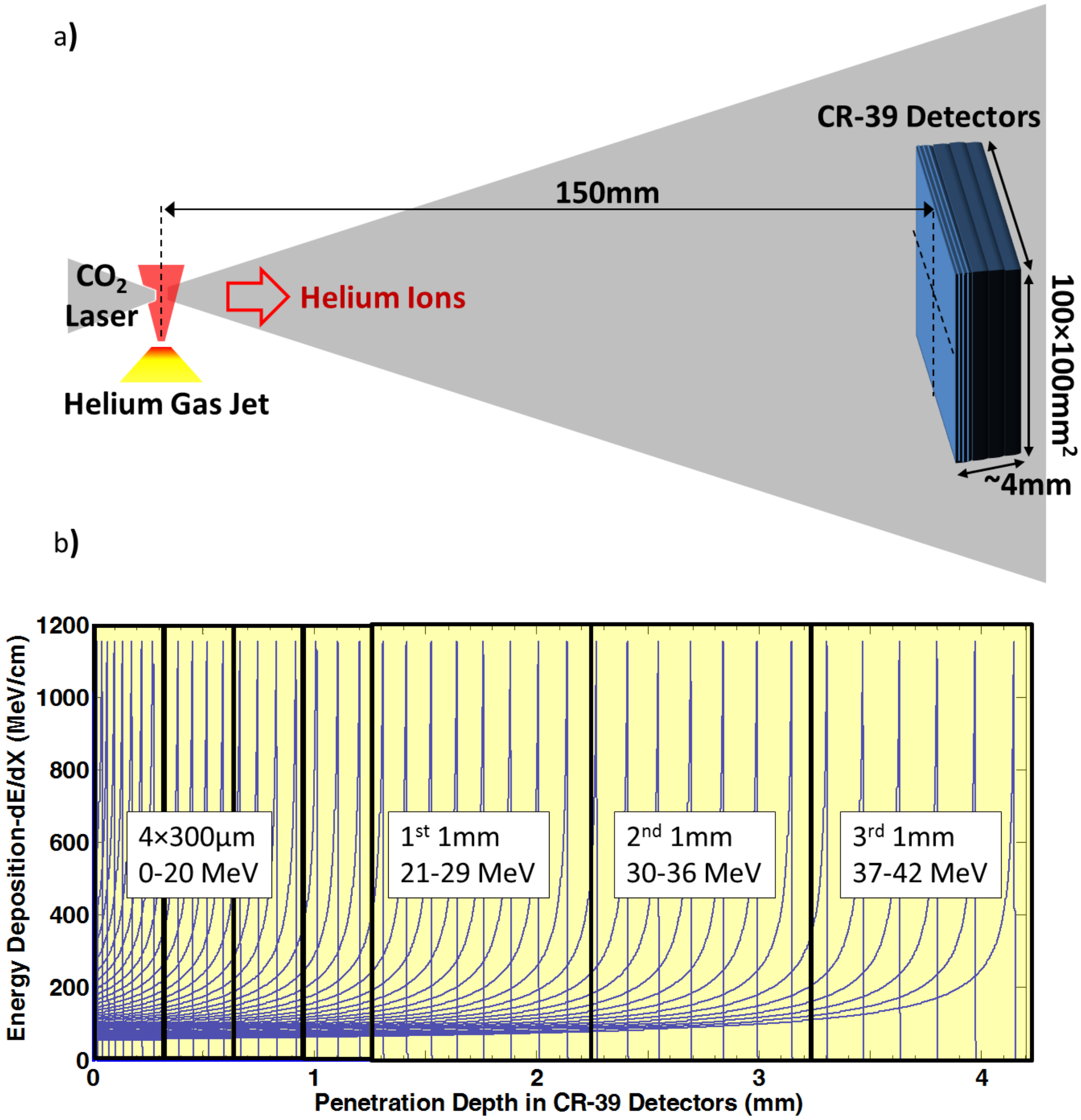

Figure 40: (a) Experimental arrangement of CR-39s for He^{1+} ion detection. (b) The helium ion (He^{1+}) energy deposition versus penetration depth in CR-39 detectors. Superimposed on top of the plot is the ion energy range covered by each CR-39 plate in the detector stack.

After exposure, each CR-39 plate in the detection stack was etched for 4 hours in a 6N NaOH solution at 80°C to analyze the ion related tracks on the front and back sides of the detectors. The etching rate ratio between the damaged areas (Track etching rate: v_t) and the bulk material (Bulk etching rate: v_b) is a key factor to determine if the ion track can be resolved. Only when v_t is larger than v_b, the etched track can be revealed under the microscope. Further etching for resolving the finer energy spectrum is performed for an additional 5 hours with a half hour etching step. With this incremental etching method, we found our spectral resolution of the detection system is 0.1MeV. And the background ion noise level is ~150 counts. The etching setup and procedure can be found in Appendix B.2.

After etching and cleaning, detectors were put under the microscope for a statistical analysis of number of particles. For this purpose, a computer-controlled automatic pit-counting system has been developed and implemented in Neptune laboratory, see Appendix B.3. In the experiment two distinct type of ion spectra have been recorded for different positions of the laser focus in the gas jet. Figure 41 shows these spectra recorded for 60J laser shots. Note that etching of CR-39 detectors results in visualization of ion tracks only in both surfaces. Therefore, after 5 hours of etching we could only resolve helium ion pits located within ~60μm thick layers shown by narrow energy bins in Figure 41.

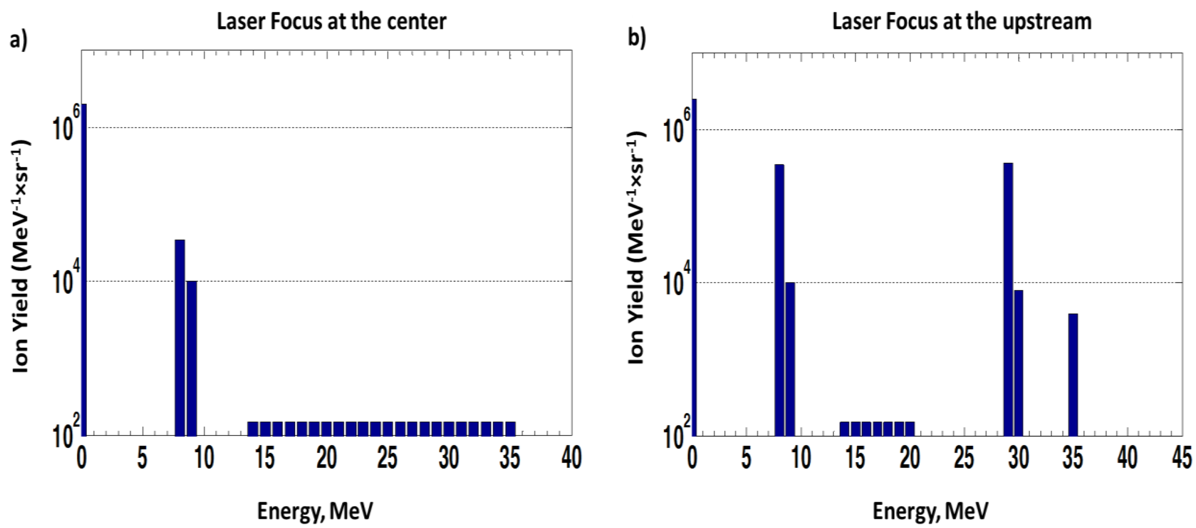

Figure 41: Ion spectra (He^{1+}) resulted from 60J LDIA experiments. a) shows the condition when laser focus is at the center of the gas jet. b) shows when the laser focus is at the upstream. Blue bar is the yield of produced ions at different energy.

As seen in Figure 41(a) and (b), high yield peaks with energy ~320keV and ~2.2×10^6 particles are detected on the front surface of the first 300μm CR-39 layer for both the center and upstream focus conditions. But, when the gas jet was moved by one Rayleigh length downstream from the focus, additional peaks with energy around 30MeV are observed. Maximum hole boring velocity measured for the 60J laser pulses is v_{hb} = 0.0068c. If we assume the He^{1+} ions were reflected with twice the hole boring velocity, the kinetic energy gained by the ions is close to 350keV. This matches well the low energy peaks on the detectors. However the yield is still rather low. These low energy ions are consistent with the energy that would be expected by the hole-boring RPA mechanism [53]. However, the hole boring effect can't explain acceleration of ions to high energy level. PIC simulations not shown in this dissertation revealed that a collisionless shock wave was launched during the laser-plasma interaction process and propagated with a velocity $v_{sh} = Mc_s >> v_{hb}$, where M is the Mach number and c_s is sound speed. Moving the laser focus upstream by ~1 z_R in the experiment apparently provides conditions for minimizing the effects of relativistic self-focusing in plasma as well as laser filamentation. Therefore, the unperturbed laser beam could reach the critical density layer and effectively pile up the plasma creating a density discontinuity along with a local heating of plasma electrons. Both these jump conditions are necessary for launching a laminar collisionless shock wave [18]. This shock wave propagates with a speed v_{sh} through an already ionized via electron collisions long scale plasma ramp and can reflect and accelerate the helium ions up to $2v_{sh}$. Based on this assumption, for the 35MeV reflected H^{1+} ions, the shock velocity can be calculated as 0.068c. However, it still should be noted that detected number of ions in the peak $\geq 10^5$ He/MeV is rather small and further optimization of both laser pulse and the target is necessary to increase the yield.

5.6 Summary

In this chapter, we have shown how picosecond, four-frame laser interferometry can be used for the visualization of the moving plasma density-cavity produced by the radiation pressure of the laser pulses. We have used these interferograms to measure the hole-boring velocity during both the rising and falling edges of the CO_2 laser macropulse. A 2D PIC code simulation is carried out to understand better the complex dynamics of laser-plasma interaction when a train of intense CO_2 laser pulses irradiates the plasma. The pulse train allows us to measure v_h as a function of the CO_2 laser intensity not only during the macropulse but also between micropulses when the laser radiation is not present. We observe that when laser related radiation pressure is pushing the initially cold plasma the hole boring velocity is monotonically increasing on the rising edge of the macropulse. As the plasma electrons are heated, thermal pressure first slows down the hole boring process and then brings it to a halt on the falling edge of the laser pulse. It is this balance of laser pressure and thermal pressure that determines dynamics of hole boring process in plasma.

We reported the observation of two groups of helium ions at low and high energy levels in different focusing conditions for the LDIA experiment. The low energy ions may be attributed to the hole-boring RPA mechanism. The high energy ions are resumably accelerated by a shock wave.

CHAPTER 6

6. Conclusion

In this dissertation, the first direct measurements of the laser hole boring velocity in an overdense helium plasma using a four-frame picosecond green pulse interferometry are presented. The CO_2 laser pulse train allows us to measure the hole boring velocity (v_{hb}) as a function of the laser intensity not only during the macropulse but also between micropulses (when the laser radiation is not present). In the experiment, the maximum v_{hb} measured for an approximately 45J laser shot with $a_o \sim 1.4$ is 6.0×10^{-3}c. By measuring the hole boring velocity during the intensity risetime and then the fall time of the macropulse we find that the hole boring process is determined by a balance between the radiation pressure P_L and thermal pressure P_{th}.

During the risetime of the laser pulse, P_L dominates P_{th} and v_{hb} increases. As the laser intensity increases and the plasma electrons are heated up and P_{th} increases. In simulations these heated electrons reflux within the plasma and the plasma cools down more slowly on the falling edge than it heats up during the rising edge. The effect of this thermal pressure is that v_{hb} decreases more rapidly during the falling edge compared to the rising edge. Hole boring phenomenon is important in fast-ignition fusion because it may allow the laser pulse to deliver the energy closer to the compressed fuel where fast electrons can be produced for ignition. It is likely to be important in hole boring RPA acceleration of ions and in launching of collisionless shocks. Our 2D visualization of the laser-bored cavity and measurements of v_{hb} in overcritical density helium plasma using CO_2 laser pulse train can certainly contribute to these applications of laser-plasma interaction.

Hole boring process at different laser and plasma conditions is also studied using the 1D OSIRIS PIC code simulations. The interaction of a single 70ps CO_2 laser pulse is compared with a train of 3ps pulses separated by 18ps. Both pulses have the same peak intensity. Simulations show the maximum hole boring velocity achieved for a smooth laser pulse is greater than the time structured pulse due to a continuous push on the plasma. Simulations also show that regardless of CO_2 laser pulse profile the hole boring process is always determined by a balance between P_L and P_{th} as mentioned.

The CO_2 Master Oscillator Power Amplifier (MOPA) laser system at the UCLA Neptune Laboratory is used for the purpose of experimentally investigating the laser hole boring process. This three-stage laser amplification system has the capability of boosting a 3ps, 10μm seed pulse from nanojoules up to tens of joules level. The peak power of the produced laser pulse can reach

~TW. A focused CO_2 laser beam produced by this system can achieve an intensity of $\leq 10^{16}$ W/cm^2 and ionize helium gas target. The unique temporal structure of the CO_2 laser pulse-3ps micropulses contained within a 100ps macropulse- not only allows us to measure the motion of the laser-produced cavity during the macropulse but also between two micropulses.

For probing the laser-produced plasma, the second harmonic of a 1μm laser pulse is used to build the four-frame laser interferometer. The 532nm probe pulse has a pulse length of 2ps. As compared with the plasma decay time (~ns level), such a short probe can 'freeze' the plasma and generate a sharp interferogram image reflecting the plasma density. Based on laser polarization, the probe is separated into four interferometric frames. Time delays between them are set as 20, 40 and 20ps respectively. Thus we can diagnose the plasma dynamics during a ~80ps time window in a single CO_2 laser shot. The temporal accuracy between the adjacent probe pulses can be controlled within $\pm$ 1ps. By applying this multi-frame laser interferometry, we can visualize the moving plasma density-cavity produced by the radiation pressure of the laser pulses. By measuring the change in the critical density layer and the edge of an inserted fiducial, three hole boring velocities can be extracted for each laser shot.

The hole boring process can accelerate ions to $2v_{hb}$. To detect these ions and in addition any ions accelerated by a collisionless shock, we installed a stack of CR-39 detectors behind the plasma. Two group of helium ions at low and high energy levels were observed at different laser focusing conditions. Low energy ions (~320keV He^{1+}) may be attributed to the hole-boring RPA mechanism. High energy ions (35MeV He^{1+}) are assumed to be resulted from a produced shock wave. Ion yield is still low and optimization of laser parameters and focusing conditions require to be done for the future experiments.

APPENDIX A

A.1: Different Ion Detectors

Detection of accelerated ions frequently relies on one or more of the following diagnostic techniques: radiochromic film (RCF) dosimetry, fluorescent measurements, and nuclear track recording.

RCF contains an active monomer layer that polymerizes if exposed to particles or ionizing radiation [54]. This reaction results in a color change of the RCF film which can be analyzed later by using optical densitometry to obtain the quantitative information of the absorbed radiation dose. Then the total yield of accelerated ions is deduced based on an ‘optical density versus dose calibration’ curve plotted for the specific film used. For instance, GafChromic MD-55, HS, and HD-810 films are all common commercial products designed for ion detection purpose.

Fluorescence, on the other hand, depends on absorption of particle energy or photon energy to change atoms’ electronic energy states. Once activated, these excited states release photons with energy equal to the energy gap which can be captured and recorded by the CCD camera. Here, the total yield of detected ions is calculated based upon the knowledge of the quantum efficiency (energy emitted versus incident energy) of the fluorescer and an estimation of the percentage of the total emitted photons collected.

However, there are two major limitations on the above two detection mechanisms. First, besides energetic ion particles, both detection principles: color change and atomic excitation are sensitive to energetic electrons and high energy photons either of which are a common product during the intense laser-plasma interaction process. Therefore, additional filters are required to decrease the noise level with the result that the targeted ion signals is reduced in the same way which leads to errors for the post analysis process. Second, sensitivity of such detectors is low and the total yield of detected ions using these methods is not a direct result of the measurement, instead it is usually inferred from a separate calibration standard which causes additional errors. To avoid these complexities, CR-39 nuclear track detectors with the single ion detection capability are often used for a cross-calibration measurement.

CR-39, or allyl diglycol carbonate, is a type of transparent polymer which can be produced in different sizes and shapes. With the optical polishing technique, it can widely be used as a basic material for fabricating eyeglass lenses. In 1978, CR-39 was first proposed to be used as a detector for accelerated ions based on the observable ion tracks created on the detector surface [55]. When ions are passing through CR-39, the positive charge and high kinetic energy of the ions cause ionization and damage the molecular bonds along their propagation trajectories. These damage areas can be revealed as cavities, or pits by etching the detectors in a NaOH solution. Clearly, we can benefit more from the unique attribute of the single particle response of the CR-39 detectors, which allows a clear determination of the ion yield especially in the case of low yield. The possibility of a single Helium ion resolved by the CR-39 detector has been demonstrated by Hara et al. [56]. The etched ion pits can be clearly observed by a sub-μm-scale atomic force microscope. A common optical microscope with a few-μm spatial resolution is capable of resolving the pit's size and shape. Even though numerous of advantages of using CR-

39's as the ion detectors have been listed, there is still one major drawback which is the complicated and time-consuming post-analysis process of the CR-39 detectors. And this is also the reason that prevents the CR-39's from being used as an online diagnostic system.

A.2: Bethe-Block Formula

Bethe-Block formula in energy lost per unit penetration length is given by: [52]

$$\frac{dE}{dx} = -2\pi N_a r_e^2 m_e c^2 \rho \frac{Z}{A} \frac{z^2}{\beta^2} [\ln(\frac{2m_e \gamma^2 v^2 W_{max}}{I^2}) - 2\beta^2] \tag{13}$$

where:

$$W_{max} = \frac{2m_e c^2 \beta^2 \gamma^2}{1 + 2(\frac{m_e}{M_i})\sqrt{1+\beta^2\gamma^2} + (\frac{m_e}{M_i})^2} \tag{14}$$

$\beta = v/c$: Normalized ion velocity

$\gamma = 1/\sqrt{1-\beta^2}$: Relativistic Lorentz factor

$N_a = 6.022 \times 10^{23} mol^{-1}$: Avogadro's number

$r_e = 2.817 \times 10^{-13} cm$: Classic electron radius

$m_e = 9.11 \times 10^{-31} kg$: Electron mass

$M_i = 6.68 \times 10^{-27} kg$: Helium ion mass

$c = 3 \times 10^8 m/s$: Speed of light

$\rho = 1330\ kg/m^3$: Density of CR-39

$Z = 146$: Atomic number of CR-39

$A = 272$: Atomic weight of CR-39

$z = 1e$: Charge of a helium ion in units of e (We use He^{1+})

APPENDIX B

B.1: Detector Dimensions and Arrangement

A stack of CR-39 detectors is used to detect the emission of energetic helium ions in the current experiment. It consists of 4 pieces of 300μm thick CR-39s at the front and 3 pieces of 1mm thick CR-39s at the back. The whole stack is located 15cm downstream from the helium gas jet. The total active area for ion detection is $100 \times 100\ mm^2$ with a ~36° solid angle covering a full expansion of the F/1.5 laser beam. Detector layers are bundled and secured in a home designed frame as shown in Figure 42.

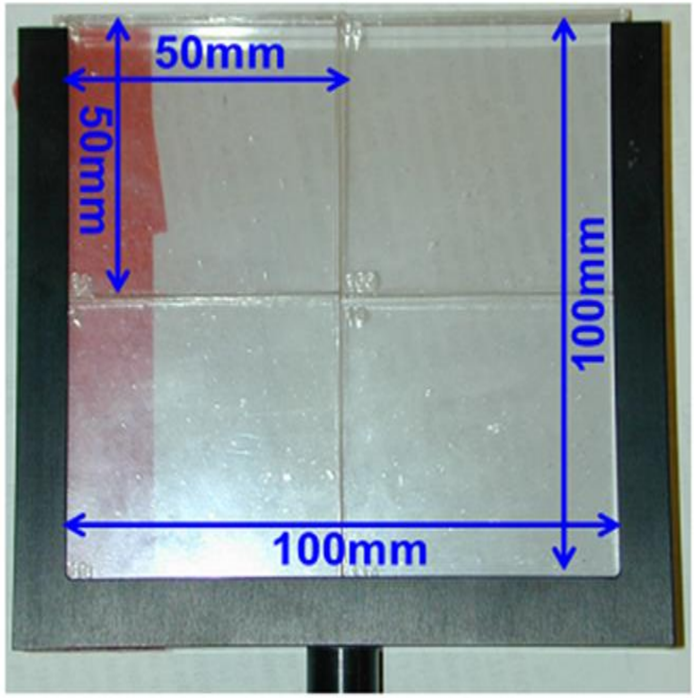

Figure 42: CR-39 detector stack. The whole stack covers 100×100 mm^2 area.

B.2: CR-39 Etching Setup

For the laser driven helium ion acceleration experiment, a large amount of CR-39 plates are required for post-processing after each run, therefore a batch etching method is developed in the Neptune laboratory to improve the etching efficiency. This setup is shown in Figure 43, where a glass container with NaOH solution is placed on a hot plate. The hot plate has a thermo-sensor which can receive the feedback signal provided by the thermocouple probe and thus maintain a constant temperature. Inside the container, a plastic insert is used to hold and separate each individual CR-39 plate. For such arrangement, a maximum of thirty six 50×50 mm^2 detectors can be etched simultaneously.

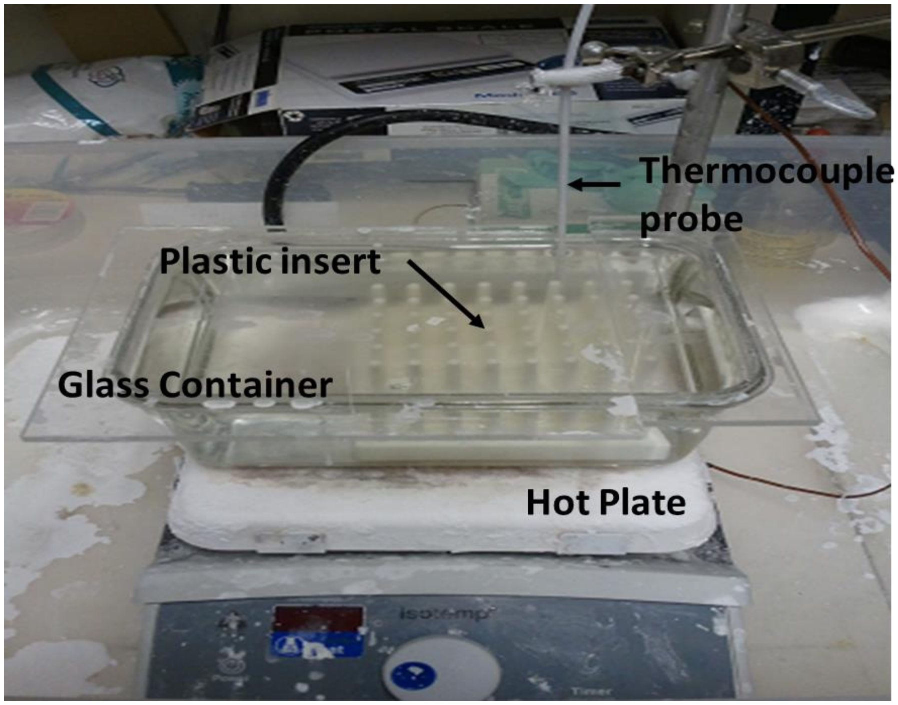

Figure 43: A picture of the CR-39 detector etching setup.

B.3: Automatic Ion Pit Counting System

Figure 44 shows schematically the automatic system for counting the ion pits following the etching of the CR39 plates.

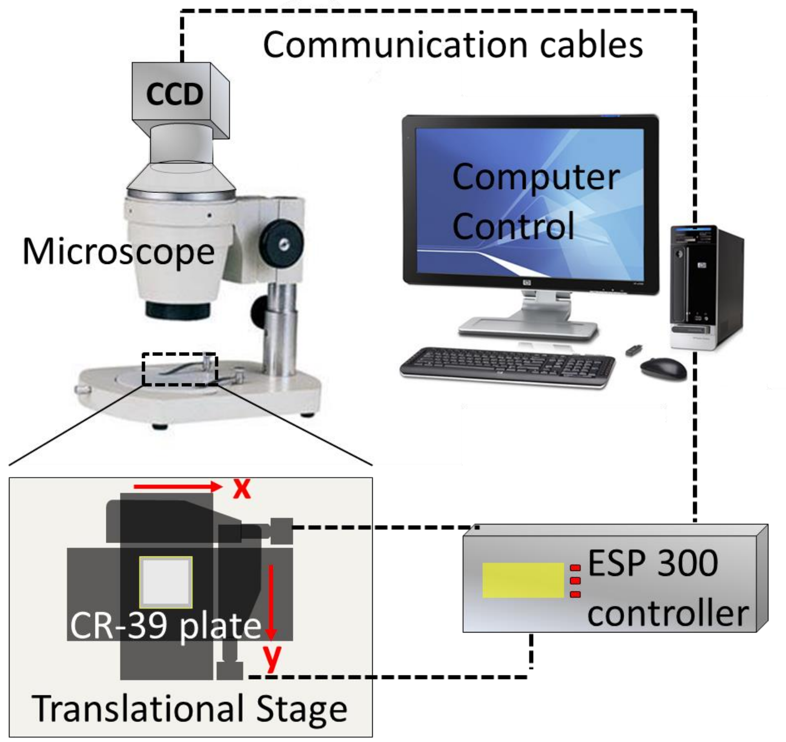

Figure 44: A schematic diagram of automatic helium ion pit counting system based on compute control. A CCD camera installed on top of the microscope is connected with the computer through the USB port. Two translation stages orientated in x and y directions are used to scan a CR-39 detector under the microscope. The stages can move with an accuracy <1μm. ESP300 controller which receives commands from the computer is used to power up the translation stages. Digital images taken by the CCD camera are saved on the computer for a post-analysis.

The system has a total magnification of 200× but a limited field of view. A LabView program is written to control the moving step of the stages and the CCD camera continuously takes snapshots of different areas on the CR-39 plate. All the digital images are saved on the computer and then used for a post analysis. For each CR-39 plate, a total of 25×25 = 625 snapshots are saved in order to recover the entire 50mm×50mm surface area. A Matlab program is written (see Appendix B.4) on the computer to combine all these snapshots in order and then generate a full scale image of the detector.

B.4: MATLAB Code for Ion Pits Counting

```
function main

% This program is used to import images and count the ion pits


clc;
clear;
close all;
pack;

disp('Orientation Condiation: 1->Back 2->Front 3->Back Topstrip 4->Back
Sidestrip 5->Front Topstrip 6->Front Sidestrip');
Orien = input('Please input the Orientation Condition: ');

if Orien < 3
    N = 1200;
else
    N = 320;
end

rscan = 40;
total1 = 0;
C = 1.02;
sum = 0;

for i = 1:N


    i_str = int2str(i);
    I = imread(['image' i_str '.tif']);
    I = rgb2gray(I);
    I = I(end: -1: 1,:);


    level = 0.74;
    I = im2bw(I,level);
    se = strel('disk', 4);
    I = ~imclose(~I, se);
```

```
    set(0, 'recursionlimit', 4000);


    [Idouble, number] = bwlabeln(~I, 8);


    Region = regionprops(Idouble, 'BoundingBox');
    clear Idouble;

    Boundingbox = cat(1, Region.BoundingBox);

    if ~isempty(Boundingbox)
    Lenwidth = Boundingbox(:, [3,4]);
    clear Boundingbox;
    clear Region;
    Diameter0 = max(Lenwidth.');
    else
        Diameter0 = 0;
    end
    Diameter = Diameter0*C;

    indice = Diameter(find(Diameter > 6 & Diameter < 60));
    numtemp = length(indice);
    sum = sum + numtemp;

    [r,c] = size(I);
    y = N/rscan - floor((i-1)/rscan);

    if rem(y, 2) == 0
       x = rscan + 1 - (i - rscan*(N/rscan-y));
    else
       x = i - rscan*(N/rscan-y);
    end

   j = size(find(I == 0), 1);
   rsm = 0; csm = 0; rbm = 0; cbm = 0;
   [rsm, csm] = find(I == 0);
   rbm = (x-1)*r + rsm; cbm = (y-1)*c + csm;
   a(total1+1: total1+j) = rbm; b(total1+1: total1+j) = cbm;
   total1 = total1 + j;
   clear I rsm csm cbm; pack;

end

figure(1);

switch Orien
    case 1
        plot(b, -a, 'k.');
    case 2
        plot(a, -b, 'k.');
    case 3
        plot(a, b, 'k.');
```

```
    case 4
        plot(-b, a, 'k.');
    case 5
        plot(-b, -a, 'k.');
    otherwise
        plot(-a, b, 'k.');
end

axis image;

title(sprintf('%d proton pits found.', total), 'fontsize', 13,
'fontweight','bold');

sprintf('The total number of particles detected is %d \n', sum);

end
```

REFERENCES

1. Strickland, D. and G. Mourou, *Compression of Amplified Chirped Optical Pulses.* Optics Communications, 1985. **56**(3): p. 219-221.
2. Langdon, A.B. and D.E. Hinkel, *Nonlinear evolution of stimulated scatter in high-temperature plasmas.* Physical Review Letters, 2002. **89**(1).
3. Malka, V., et al., *Principles and applications of compact laser-plasma accelerators.* Nature Physics, 2008. **4**(6): p. 447-453.
4. Willi, O., et al., *Inertial confinement fusion and fast ignitor studies.* Nuclear Fusion, 2000. **40**(3Y): p. 537-545.
5. Boyd, T.J.M., *Laser Plasma Interaction Physics in Underdense Coronal Plasmas.* Canadian Journal of Physics, 1986. **64**(8): p. 944-955.

6. Sarkisov, G.S., et al., *Self-focusing, channel formation, and high-energy ion generation in interaction of an intense short laser pulse with a He jet.* Physical Review E, 1999. **59**(6): p. 7042-7054.

7. Willingale, L., et al., *Surface waves and electron acceleration from high-power, kilojoule-class laser interactions with underdense plasma.* New Journal of Physics, 2013. **15**.

8. Ting, A., et al., *Plasma wakefield generation and electron acceleration in a self-modulated laser wakefield accelerator experiment.* Physics of Plasmas, 1997. **4**(5): p. 1889-1899.

9. Joshi, C., *The Plasma Beat Wave Accelerator .1. Experiments.* Aip Conference Proceedings, 1982(91): p. 28-42.

10. Joshi, C., et al., *Ultrahigh Gradient Particle-Acceleration by Intense Laser-Driven Plasma-Density Waves.* Nature, 1984. **311**(5986): p. 525-529.

11. Esarey, E., C.B. Schroeder, and W.P. Leemans, *Physics of laser-driven plasma-based electron accelerators.* Reviews of Modern Physics, 2009. **81**(3): p. 1229-1285.

12. Krushelnick, K., et al., *Multi-MeV ion production from high-intensity laser interactions with underdense plasmas.* Physical Review Letters, 1999. **83**(4): p. 737-740.

13. Cui, Y.Q., et al., *Laser absorption and hot electron temperature scalings in laser-plasma interactions.* Plasma Physics and Controlled Fusion, 2013. **55**(8).

14. Corkum, P.B., *Plasma Perspective on Strong-Field Multiphoton Ionization.* Physical Review Letters, 1993. **71**(13): p. 1994-1997.

15. Krushelnick, K., et al., *Effect of relativistic plasma on extreme-ultraviolet harmonic emission from intense laser-matter interactions.* Physical Review Letters, 2008. **100**(12).

16. Horlein, R., et al., *High harmonics from solid surfaces as a source of ultra-bright XUV radiation for experiments.* Plasma Physics and Controlled Fusion, 2008. **50**(12).

17. Palmer, C.A.J., et al., *Monoenergetic Proton Beams Accelerated by a Radiation Pressure Driven Shock.* Physical Review Letters, 2011. **106**(1).

18. Forslund, D.W. and C.R. Shonk, *Formation and Structure of Electrostatic Collisionless Shocks.* Physical Review Letters, 1970. **25**(25): p. 1699-&.

19. Wilks, S.C., et al., *Absorption of Ultra-Intense Laser-Pulses.* Physical Review Letters, 1992. **69**(9): p. 1383-1386.

20. Zepf, M., et al., *Measurements of the hole boring velocity from Doppler shifted harmonic emission from solid targets.* Physics of Plasmas, 1996. **3**(9): p. 3242-3244.

21. von der Linde, D., *Generation of high order optical harmonics in steep plasma density gradients.* Superstrong Fields in Plasmas, 1998(426): p. 221-230.

22. Kruer, W.L., E.J. Valeo, and K.G. Estabrook, *Limitation of Brillouin-Scattering in Plasmas.* Physical Review Letters, 1975. **35**(16): p. 1076-1079.

23. Kruer, W.L., *The physics of laser plasma interactions.* Book, 1988.

24. Ahedo, E. and J.R. Sanmartin, *Resonant Absorption in a Plasma Step Profile.* Plasma Physics and Controlled Fusion, 1987. **29**(3): p. 419-432.

25. Mulser, P. and D. Bauer, *High Power Laser-Matter Interaction.* High Power Laser-Matter Interaction, 2010. **238**: p. 1-416.

26. Sun, G.Z., et al., *Self-Focusing of Short Intense Pulses in Plasmas.* Physics of Fluids, 1987. **30**(2): p. 526-532.

27. Fonseca, R.A., et al., *OSIRIS: A three-dimensional, fully relativistic particle in cell code for modeling plasma based accelerators.* Computational Science-Iccs 2002, Pt Iii, Proceedings, 2002. **2331**: p. 342-351.

28. Tsung, F., et al., *CO2 Laser acceleration of forward directed MeV proton beams in a gas target at critical plasma density.* Journal of Plasma Physics, 2012. **78**: p. 373-382.

29. Platonenko, V.T. and V.D. Taranukhin, *Coherent Amplification of Light-Pulses in Media with a Discrete Spectrum.* Kvantovaya Elektronika, 1983. **10**(11): p. 2246-2257.

30. Haberberger, D., S. Tochitsky, and C. Joshi, *Fifteen terawatt picosecond CO2 laser system.* Optics Express, 2010. **18**(17): p. 17865-17875.

31. Alcock, A.J. and P.B. Corkum, *Ultra-Fast Switching of Infrared Radiation by Laser-Produced Carriers in Semiconductors.* Canadian Journal of Physics, 1979. **57**(9): p. 1280-1290.

32. Filip, C.V., et al., *Optical Kerr switching technique for the production of a picosecond, multiwavelength CO2 laser pulse.* Applied Optics, 2002. **41**(18): p. 3743-3747.

33. Ganeev, R.A., A.I. Ryasnyanski, and H. Kuroda, *Nonlinear optical characteristics of carbon disulfide.* Optics and Spectroscopy, 2006. **100**(1): p. 108-118.

34. Autler, S.H. and C.H. Townes, *Stark Effect in Rapidly Varying Fields.* Physical Review, 1955. **100**(2): p. 703-722.

35. Haberberger, D., *Shock Wave Acceleration of Monoenergetic Protons using a Multi-Terawatt CO_2 Laser.* 2012 Ph.D. Dissertation.

36. G. S. Settles, *Schlieren and Shadowgraph Techniques: Visualizing Phenomena in Transparent Media.* Berlin, Germany: Springer, 2001.

37. Schappert, G.T. and M.J. Herbst, *Anomalous Dispersion Effects on Pulse-Propagation in High-Pressure Co2 Amplifiers.* Applied Physics Letters, 1975. **26**(6): p. 314-315.

38. Mccall, S.L. and E.L. Hahn, *Self-Induced Transparency.* Physical Review, 1969. **183**(2): p. 457-&.

39. Takahashi, K., et al., *Laser-hole boring into overdense plasmas measured with soft x-ray laser probing.* Physical Review Letters, 2000. **84**(11): p. 2405-2408.

40. S. Ivancic, D.H., H. Habara, et al., *Channeling of multikilojoule high-intensity laser beams in an inhomogeneous plasma.* Physical Review E, 2015.

41. Takeda, M., H. Ina, and S. Kobayashi, *Fourier-Transform Method of Fringe-Pattern Analysis for Computer-Based Topography and Interferometry.* Journal of the Optical Society of America, 1982. **72**(1): p. 156-160.

42. Leemans, W.P., et al., *Plasma Physics Aspects of Tunnel-Ionized Gases.* Physical Review Letters, 1992. **68**(3): p. 321-324.

43. Brunel, F., *Not-So-Resonant, Resonant Absorption.* Physical Review Letters, 1987. **59**(1): p. 52-55.

44. Sentoku, Y., et al., *Laser hole boring and hot electron generation in the fast ignition scheme.* Fusion Science and Technology, 2006. **49**(3): p. 278-296.

45. Ammosov, M.V., N.B. Delone, and V.P. Krainov, *Tunnel Ionization of Complex Atoms and Atomic Ions in a Varying Electromagnetic-Field.* Zhurnal Eksperimentalnoi I Teoreticheskoi Fiziki, 1986. **91**(6): p. 2008-2013.

46. Jaanimagi, P.A., et al., *Return-Current Electron Streams in High-Intensity Laser Target Interaction.* Applied Physics Letters, 1981. **38**(10): p. 734-736.

47. Nilson, P.M., et al., *High-intensity laser-plasma interactions in the refluxing limit.* Physics of Plasmas, 2008. **15**(5).

48. Mironov, V., et al., *Effect of the laser pulse temporal shape on the hole boring efficiency.* Plasma Physics and Controlled Fusion, 2012. **54**(9).

49. Cowan, T.E., et al., *Ultralow emittance, multi-MeV proton beams from a laser virtual-cathode plasma accelerator.* Physical Review Letters, 2004. **92**(20).

50. Borghesi, M., et al., *Electric field detection in laser-plasma interaction experiments via the proton imaging technique.* Physics of Plasmas, 2002. **9**(5): p. 2214-2220.

51. Haberberger, D., et al., *Collisionless shocks in laser-produced plasma generate monoenergetic high-energy proton beams.* Nature Physics, 2012. **8**(1): p. 95-99.

52. Leo, W.R., *Techniques for Nuclear and Particle Physics Experiments.* 2nd ed. Berlin, Germany: Springer-Verlag, 1994.

53. Robinson, A.P.L., et al., *Hole-boring radiation pressure acceleration as a basis for producing high-energy proton bunches.* Plasma Physics and Controlled Fusion, 2012. **54**(11).

54. McLaughlin, W.L., et al., *Radiochromic solid-state polymerization reaction.* Irradiation of Polymers, 1996. **620**: p. 152-166.

55. Cartwright, B.G., E.K. Shirk, and P.B. Price, *Nuclear-Track-Recording Polymer of Unique Sensitivity and Resolution.* Nuclear Instruments & Methods, 1978. **153**(2-3): p. 457-460.

56. Hara, K., et al., *Single-ion detection using nuclear track detector CR-39 plastic.* Review of Scientific Instruments, 1999. **70**(12): p. 4536-4538.